PHYSIK-DEPARTMENT

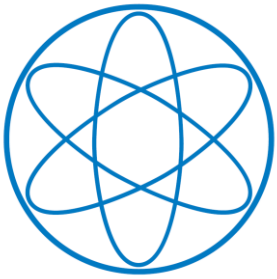

Light-induced electron motion in nanojunctions

Doktorarbeit

von

Daniel Friedrich Gerster

TECHNISCHE UNIVERSITÄT
MÜNCHEN

TECHNISCHE UNIVERSITÄT MÜNCHEN

Physik Department E20

-

Molekulare Nanowissenschaften & Chemische Physik von Grenzflächen

Light-induced electron motion in nanojunctions

Daniel Friedrich Gerster

Vollständiger Abdruck der von der Fakultät für Physik
der Technischen Universität München zur Erlangung des akademischen Grades eines

Doktors der Naturwissenschaften (Dr. rer. nat.)

genehmigten Dissertation.

Vorsitzender: Univ.-Prof. Dr. Harald Friedrich
Prüfer der Dissertation:

1. Univ.-Prof. Dr. Johannes V. Barth
2. Univ.-Prof. Dr. Alexander W. Holleitner

Die Dissertation wurde am 29.02.2012 bei der
Technischen Universität München eingereicht und
durch die Fakultät für Physik am 16.04.2012 angenommen.

Abstract

Photochemical reactions in biology as well as optoelectronic applications are driven by optical excitation of charge carriers. In this work the light-induced electron motion through nanoscale objects in the limits of different electron transport models is studied experimentally. A gold coated scanning near-field optical microscope tip is employed in two experimental configurations. First, photosynthetic protein complexes (PS I) which can be considered as model systems for optically driven charge separation were investigated. Individually contacted single PS I revealed a photocurrent of 10 pA under laser illumination. In a second approach electrons in metal-dielectric-metal nanojunctions were optically excited and steered by ultrashort laser pulses. The results show that the collective electron motion within a dielectric can be controlled by the optical field and generates a macroscopically detectable current.

Zusammenfassung

Photochemische Prozesse in der Biologie als auch optolektronische Anwendungen werden durch optische Anregung von Ladungsträgern angetrieben. In dieser Arbeit wird die lichtinduzierte Elektronenbewegung in nanoskopischen Objekten in den Grenzen zweier Elektronentransportmodelle experimentell untersucht. Hierfür wird eine metallisierte nahfeldmikroskopische Spitze in zwei verschiedenen experimentellen Anordnungen verwendet. Zunächst wurden photosynthetische Proteinkomplexe (PS I), die als Modelsystem für optische angeregte Ladungstrennung angesehen werden, untersucht. Unter Laserbestrahlung zeigen einzelne PS I einen Photostrom von 10 pA. Im zweiten Experiment wurden Elektronen in einem Metall-Dielektrikum-Metall Nanokontakt durch ultrakurze Laserpulse optisch angeregt und gesteuert. Die Ergebnisse zeigen, dass die kollektive Elektronenbewegung durch das optische Feld gesteuert und ein makroskopisch detektierbarer Strom generiert wird.

Contents

1 Introduction

Light-induced electron transfer in nanoscale objects plays a key role in light driven nanotechnology applications as well as photochemical reactions. Photosynthesis is the most important process in biology, converting solar energy into stable chemical energy via optically-induced charge separation. As a by-product oxygen is produced. On the molecular scale this light driven reaction is accomplished by the absorption of photons by photosynthetic protein complexes. Nearly every photon which is absorbed effects a charge separation. In 1988 Huber, Deisenhofer and Michel received the Nobel prize in chemistry for the determination of the three-dimensional structure of a photosynthetic reaction center. These findings are important for renewable energy sources as organic photovoltaic devices, that attract increased interest as fossil energy sources are expected to run out within the following decades. To improve the performance and efficiency of such devices a basic understanding on the single molecule level is mandatory. Photosynthetic protein complexes can be understood as model systems for an electron pump in the field of molecular electronics. Innovative applications in optoelectronics (photodetection), photovoltaic devices (solid state), as well as photochemical cells based on this protein complexes are under development.
Optically controlled electronic switching is expected to increase the operation speed of state-of-the-art semiconductor technology, at the current status limited to several GHz. The combination of light confinement on the nanometer scale and high optical fields can be used to explore light-induced processes on the molecular/atomic level. Techniques employing nanoplasmonics play a key role for the investigation of optical excitation of electrons in molecules and solid state devices. It can be used to produce localized light sources which illuminate only a small sample volume.

In this thesis the light-induced electron motion in nanoscale junctions was studied in the limits of two different electron transport regimes. First, electron transport through a single photosynthetic protein complex (Photosystem I) embedded between two metal electrodes was investigated (hopping transport). The Photosystem I is characterized by an internal quantum efficiency close to 1. This high efficiency makes the protein an interesting candidate for future devices. In this approach a metalized glass-tip acts as a localized light-source and as an electrode at the same time. This configuration is the connecting link to the

second experimental approach, where the tip was employed as metal-dielectric-metal solid-state device, probing the optical excitation mechanisms inside the dielectric with ultrashort laser-pulses in the limits of ballistic transport.

1.1 Outline of the thesis

In the first chapter the basic concepts of molecular electronics (section 1.2), ballistic electron transport (section 1.3), optical induced transport phenomena (section 1.4), nanoplasmonics (section 1.5), scanning near-field microscopy (SNOM) (section 1.6) as well as the photosynthetic protein complex Photosystem I (section 1.7) are introduced. The chapter ends with an explanation of the principles of lightwave electronics (section 1.8). The first part of chapter 2 gives an insight into the properties of the tetrahedral SNOM-tip, employed as a probe during this thesis in two experimental configurations (section 2.1). Subsequently the experimental set-up for the exploration of the electron transport properties of single molecules is elucidated (section 2.2). The last section deals with a laser-system and the experimental set-up, generating laser pulses in the timescales of sub-femtoseconds, thus enabling the investigation of charge carrier excitation in a dielectric with the electric field of the laser pulses (section 2.3). Chapter 3 is divided in two main parts. In the beginning the results of the electron transport measurements of single Photosystem I proteins under laser illumination are interpreted (section 3.2). In the second part the measurements aimed to explore the charge carrier excitation and motion control in a dielectric are presented and compared with simulations of possible excitation mechanisms (see section 3.3). This thesis ends with chapter 4, giving a summary and an outlook for future research in this field and possible applications.

1.2 Molecular electronics and single molecule transport

The concept of "molecular electronics" is based on the idea of employing molecules as functional parts in electric circuits [1–4]. There is an enormous potential to exploit molecular functionalities in possible molecular applications like switches, rectifiers, transistors, light emitters and organic-inorganic hybrid devices [4–8]. Even if molecular electronic devices might never be based on the operation of single molecules, it is crucial to improve the understanding of already existing molecular-film devices like organic light emitting diodes (OLEDs) by investigation of the relevant processes on the single molecular level [9]. As the ongoing miniaturization (*top-down* approach) in semiconductor technology is supposed to reach its limits in the near future, new technologies to fabricate electronic devices are developed. Molecular electronics is a promising candidate for future applications, based on the *bottom-up* approach where devices might be built up from the molecular level into

integrated circuits [10]. However, a basic understanding of the principles in this field is required to further a young technology [11]. Aviram and Ratner first proposed in 1974 a molecule which could serve as a rectifier [12]. Today this paper is often referred to as the founding statement of molecular electronics [13]. First experiments on molecular films to explore the electric properties of molecules were performed by Kuhn and Mann in the 1970s with self assembled monolayers (SAMs) employing the Langmuir-Blodgett (LB) technique [11, 14]. In the following years experiments by Metzger et al. [15] revealed diodic behavior in LB-films. A variety of techniques have been developed within the last 20 years to study the properties of single molecular junctions (see section 1.2.1 and 1.2.2) and supply experimental data for theoretical models to describe the mechanisms of charge transfer (see section 1.2.3) in such metal-molecule-metal systems.

Molecular and hybrid devices

Recent reports have demonstrated that single small molecules can act as functional parts in electric [8, 11, 16–18] and optoelectronic circuits [19–22]. Photochemical reactions in diarylethene and azobenzene molecules have been exploited to trigger an on/off switching of nanoscale electronic circuits [7, 23, 24]. Photoexcitation of single photosynthetic reaction centers (see section 1.7) leads to an enhanced photoconductance across photosynthetic proteins [25, 26]. In carbon nanotube devices, PS I was shown to photogate the conductance of the nanotubes [27, 28] and metal nanoparticles have been utilized to enhance the light absorption and circular dichroism of the PS I over its entire absorption spectrum [29, 30].

1.2.1 Common techniques to study single molecule transport

A number of techniques to study the electron transport through organic molecules and monolayers have been developed within the last decades. Here, a brief overview on the most common techniques is given. First experiments were performed on molecular films, fabricated with the so called LB-technique [14]. Experiments reveal an exponential decay in the current depending on the distance (see figure 1.1 a)) [14]. A main drawback of experiments performed on molecular self-assembled monolayers (SAM) is the fact that it is a space-averaging method and thus the properties of a single molecule are not directly accessed [2].

The invention of the scanning tunneling microscope (STM) by Binnig and Rohrer [31] and the atomic force microscope (AFM) by Binnig et al. [32] opened the door to explore the electric and mechanic properties on the single molecule level [2]. In STM and AFM-experiments a metallic tip is directed on top of a molecule covered metal substrate and the tunneling current between tip and molecule substrate is measured. The tunneling current is not only exponentially dependent on the distance but reveals also the electronic properties

of the molecular film (see figure 1.1 b)). It is also possible to manipulate single atoms or molecules and perform tunneling spectroscopy on single molecules [2]. In AFM the mechanical properties of molecules can be studied [2, 4]. Different AFM-scanning modes and techniques have been developed as the current probe (CP)-AFM or nanoparticle (NP)-AFM [11, 33, 34]. A drawback is the limited spatial long term stability [4], necessary to form a stable contact between tip and molecule.

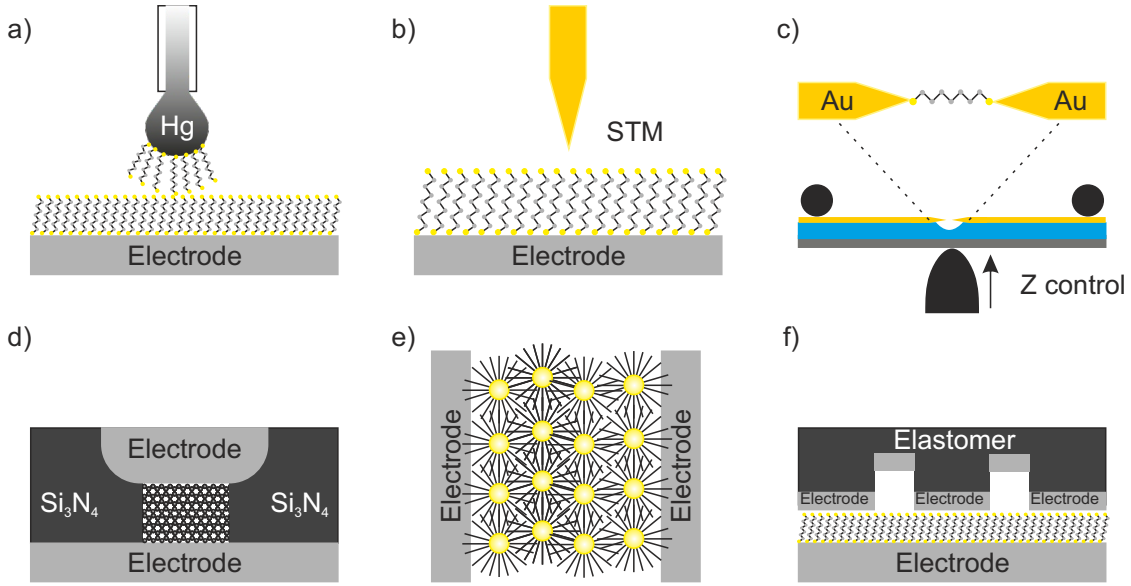

Figure 1.1: Experimental configurations to study the electric transport properties of molecules or molecular films: a) A hanging mercury electrode with a monolayer of molecules connected to a second molecular layer on the underneath electrode. With this configuration first molecular transport measurements were realized. b) STM (or AFM) realization, where a sharp metallic tip probes the self-assembled molecules on a substrate. c) With the MCBJ technique extremely stable gap-control is achieved. d) A nanopore configuration, where an ensemble of molecules is embedded in a pore, sandwiched from the bottom and the top by electrodes. e) Array of molecule covered nanoparticles to probe the electron transport properties of molecules. f) Nanotransfer printing is a new technique to fabricated reproducible metal-molecular-film-metal junctions. Figures adopted from [11].

This problem was overcome by the introduction of the mechanically controlled break-junction technique (MCBJ) [4, 35]. This technique is based on a three point bending machinery of a flexible substrate (see figure 1.1 c)). On top of the flexible substrate a thin wire with a constriction is prestructured, forming a freely suspended metal bridge. A pushing rod is moved upwards, while both ends of the substrate are pressed against a counter support. The metallic bridge in the center of the substrate is elongated, until the contact

is mechanically broken. Subsequently the contact can be closed with sub-Ångstrom precision. The ratio between surface elongation and displacement of the center pushing rod is in the order of 10^{-4}, meaning that for example a height difference of the pushing rod of 1 μm effects a distance of 1 Ångstrom between the metallic contacts [4]. Based on this highly stable technique first transport measurements of a single molecule linked between the metallic contacts were realized [16, 36]. MCBJs combine high mechanical stability with the possibility to form and open a molecule contact as often as necessary, thus statistics about single molecule junctions are provided [37]. A similar principle can be realized with STM, named as STM-BJs [38, 39]. A drawback of MCBJs and STM-BJs is the fact that an additional electronic gating in molecular junctions is technically hard to realize.

An alternative technique to contact single molecules is the electromigration method. This technique provides nanogaps by applying high DC-voltages to prestructured metal nanowires with a constriction [4, 40]. High electric fields in the constriction effect material transport along the constriction. A nanogap has formed when the formerly low ohmic electrical resistance suddenly increases up to several MΩ. Electromigration is strongly dependent on the material, the surface roughness and the temperature [4]. The reproducibility of this electrodes is poor, since the gap formation strongly depends on the microscopic structure of the metal bridge, which effectuates a strong variation of the gap width. After the gap formation the junction is highly stable [4].

Electrochemical fabrication of nanosized gaps was introduced by Morpurgo et al. [41] and others [42]. The difficult reproducibility of the gap-size as well as the geometry and the transfer of the fabricated tips from the liquid phase to other environments prevented an establishment of this technique by now [4]. In electrochemical STM, the electrolyte can induce gating effects [43]. Also other techniques employing STM or AFM tips with metallic nanoparticles at the end of the tips have emerged [11, 44]. Nanotransfer printing [11, 45], nanopores [11, 46] and 2-dimensional arrays of nanoparticles [11, 47] embedded between two electrodes are further techniques to name but a few (see figure 1.1 d)-f)). These approaches primary aim to explore ensembles of molecules and molecular films. A detailed description of all state of the art techniques to contact organic molecules for the investigation of its electrical properties can be found in [2–4, 11].

1.2.2 Properties of single molecular junctions

In 1997 Reed et al. [36] achieved for the first time to contact single molecules in a reproducible and well controlled manner by MCBJs followed by detailed investigations of Reichert et al. in 2002 [16]. Thereby the molecules are covalently bound between two gold

electrodes. Current-voltage-characteristics of both symmetric and asymmetric anthracene derivatives were studied. Their conductance measurements revealed:

- A lock-in behavior of the molecules when closing the gap between both electrode is observed.
- The asymmetric properties of the molecule are reflected in the current-voltage-characteristics. In ensembles of contacted molecules this effect would be averaged out.
- Molecular fluctuations appeared in subsequent measurements, indicating the single molecular character and strong dependency on the local environment of the molecule.

At the same time different models to describe the electronic transport through the molecules evolved, which are described below.

1.2.3 Theoretical description of transport mechanisms

The first theoretical description of a single molecule acting as a diode has been made by Aviram and Ratner in 1974 as already mentioned in section 1.2 [12]. In a simplified model a metal-molecule-metal junction can be divided into three main parts as visualized in figure 1.2:

1. The macroscopic metal electrodes: They are specified by their electrochemical potentials μ_1, μ_2 where the potential is adjustable by applying an external voltage U.
2. The molecule: Single molecules are characterized by the electronic structure of their molecular orbitals. The position of energy levels and their level spacing ΔE has great influence on the electron transport across the junction.
3. The coupling constants Γ_1 and Γ_2: These constants give information about the coupling strength between the electrodes and the molecule. For example a strong coupling can result in a higher electron transfer rate through the molecule. The type of bond of the anchor groups of a molecule to the electrodes affects the electron transport properties by several orders of magnitude [48]. The coupling constants are quantified in energy dimensions, thus a strong coupling corresponds to a low energy barrier height (small coupling constant) and a broadening of the energy levels [4]

The Coulomb energy E_C describes the amount of energy that is required to load or unload a molecule with an additional electron. As the capacity C of quantum objects is very small $E_C = \frac{e^2}{2C}$ can also play a decisive role in the electronic transport properties. In IV-characteristics the Coulomb energy comes apparent as a so called Coulomb staircase. Within this work two different transport regimes have to be considered: Coherent tunneling

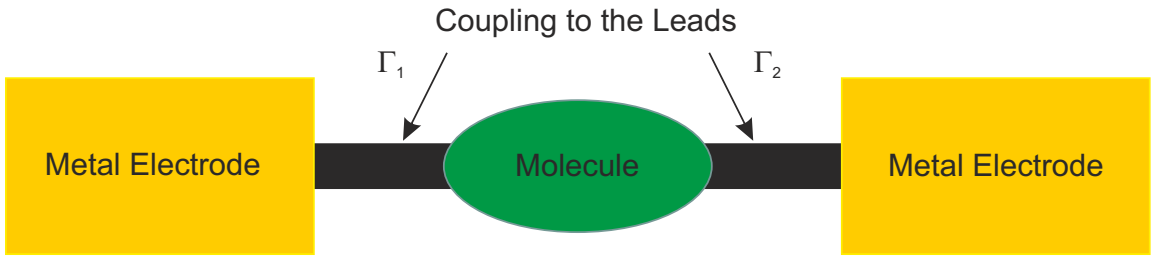

Figure 1.2: Sketch of metal-molecule-metal-junction to model the transport mechanism.

and sequential hopping. The primary mechanism describes ballistic electron transport, with strong coupling between electrodes and molecule. Sequential hopping is the dominant mechanism for long-wired molecules, characterized by a weaker coupling to the electrodes and an inelastic electron transport over large distances. Both regimes are specified in the next two chapters.

Coherent tunneling

Coherent tunneling describes electron tunneling through a molecule, in which the phase information of the wavefunction of tunneling electrons is preserved [4]. This transport mechanism is mainly present in short molecules with a strong coupling between the molecule and the metallic leads ($\Delta E > \Gamma$) [49]. The high coupling can effect a high electron transmission rate across the molecule, thus a short residence time of electrons on the molecule. Figure 1.3 a) depicts schematically a single molecule junction with its molecular orbitals embedded between two metal electrodes with the electrochemical potentials μ_1 and μ_2 at $U_{bias} = 0$ V. The case, when a bias voltage between the electrodes is applied, is illustrated in figure 1.3 b). Electrons directly tunnel through the molecule, when the electrochemical potential is in resonance with one of the energy levels of the molecule. Electron transport measurements on single molecules were performed in dependence on a variety of parameters, for example as a function of the bonding between molecules and the leads or as a function of temperature [4, 50, 51]. Among others the conductance dependence on the length of non-conjugated (for example alkanedithiols) molecules with a strong coupling was studied [17]. It became apparent that the conductance decays exponentially with increasing length of the molecules. An explanation for the exponential decay can be found with the so called bridge model as depicted in figure 1.3 c) based on the tight-binding approach, where a molecule is built up of a bridge with N identical sites ($B_N = B$) [4, 52]. In this model only nearest neighbors are considered, thereby the transfer of electrons along the molecule is described by transfer rates $t_{N,N+1} = t$ between neighboring sites [4]. This model results in an exponential decay of the conductance for increasing length, where electron transfer through the N bridges can be seen as single-step tunneling processes.

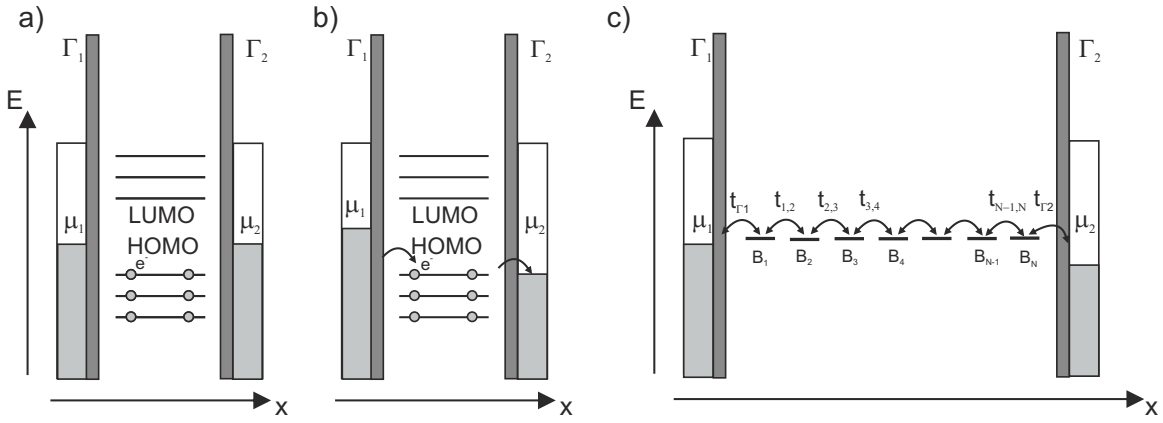

Figure 1.3: Sketch showing the principles of coherent electron tunneling through a single molecule. The metal electrodes are characterized by their electrochemical potentials μ_1, μ_2. Γ_1 and Γ_2 are the coupling constants, which define the strength of coupling between the molecules and electrodes. Between the electrodes the molecule with its occupied and unoccupied energy levels is situated. a) The system at U_{bias}= 0 V. b) A voltage is applied between the electrodes. When a molecular orbital is in resonance with a the electrochemical potential of one of the electrodes, electron flow occurs. c) Bridge model with N bridges, where electron transfer between next neighbors is assumed. Figures adopted from [4, 50].

Sequential hopping

In case of a weak coupling to the electrodes ($\Delta E < \Gamma$) non-coherent transport is best described in a hopping picture. It is most commonly found in long-wired molecules with small barriers between bridging sites [1]. It is assumed that electrons are localized in specific positions of the molecule, sequentially hopping to the next bridge position, as depicted in figure 1.4. This transport mechanism gets relevant when the contact time of the electrons on the molecule is comparable with the time scale of inelastic processes [4]. In huge and complex molecules like proteins and DNA this transport mechanism dominates [53, 54]. Hopping is often a thermally activated process where electrons are heaved by thermal energy to higher energy levels and thus reduce the effective tunneling barriers [4, 49]. The transition from coherent tunneling to hopping is strongly dependent on the molecular species [1, 4]. The hopping regime can then be characterized by an exponential dependency on temperature ($e^{-\Delta E/k_B T}$, where ΔE is the activation energy) and a weaker dependency on the length (in the order of $\approx 1/N$) [1, 4, 55]. The large activation energy for example in optically active redox-protein complexes as the Photosystem I (introduced in section 1.7), ΔE is overcome by the absorption of a photon.

Nitzan et al. [55] showed that the electron transfer rate k, from the chemical reaction theory [56], is correlated with the conductance of long-wired biological molecules. In biolog-

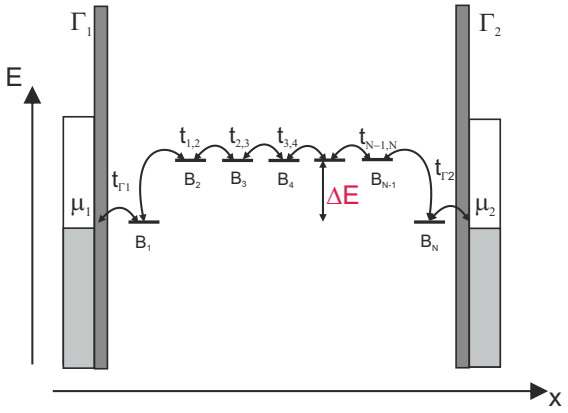

Figure 1.4: The sketch shows a modeled long-wired molecular conductor with N bridge sites embedded between metallic leads. To activate electron transport the activation energy ΔE has to be overcome. Only next-neighbor tunneling is considered.

ical molecules the chemical environment plays an important role for the electron transport properties of the molecule [4]. Experimentally it has been shown that the conductance of proteins acting as solid state conductors can be several orders of magnitude higher than in solution [54, 57].

1.3 Ballistic electron transport

The investigation of electron transport properties in nanosized metal wires revealed that the validity of *Ohm's law* is restricted to macroscopic contacts. In nanoscale physics one has to distinguish between diffusive and ballistic transport. To classify these regimes the elastic mean free path l is introduced, which describes the mean distance between elastic collisions with impurities. Considering a sample with the length L, then the regime $l \ll L$ is named diffusive, whereas the regime $l > L$ is called ballistic transport regime [58]. In the ballistic transport regime the electron can move without collision through the nanostructure. With a scattering approach Landauer derived a formula for the finite conductance in atomic-sized metal constrictions [58–60]. If one additionally reduces the diameter of the metal wire to the order of the electron-wavelength, conductance quantization can be observed. The quantized conductance of a single metal atom or a row of atoms between both electrodes is defined as:

$$G_0 = \frac{2e^2}{h} \approx \frac{1}{12,9}\frac{1}{k\Omega}, \tag{1.1}$$

with the electron charge e and Planck's constant h [49, 58, 61, 62]. The general conductance formula for N channels with the transmission coefficient t_n of the nth-channel can be written

as:

$$G = G_0 \sum_{n=1}^{N} t_n \tag{1.2}$$

[62]. This approach can also be applied to short molecular wire junctions, as introduced in section 1.2.3, whereby the transmission coefficient comprises coupling parameters and electron transfer rates [44].

1.4 Optically-induced transport phenomena

The photocurrent of an optoelectronic device is defined as the residual current measured at zero bias voltage ($U_{SD} = 0\ V$) upon light irradiation (see figure 1.5 b)), also named short circuit current. The photocurrent at zero bias voltage reveals that light is absorbed and separates charge carriers which induce a current flow. For this case the current-voltage characteristics are shifted from zero to I_{photo}, but the slope remains the same. The photovoltage U_{photo} is defined at I = 0 A. These definitions for photocurrent and photovoltage are used within this thesis. The photocurrent is sometimes determined as $I_{photo} = \Delta I(U_{SD}) = I_{on} - I_{off}$ at a given voltage U_{SD}, which is considered to be misleading. This current difference is

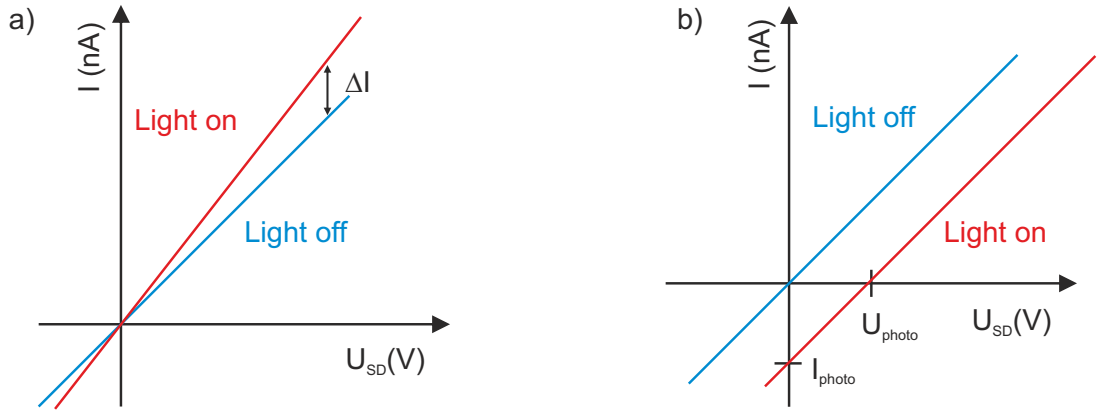

Figure 1.5: a) Visualization of photoconductance, where light illumination changes the slope of IV-characteristics by the current ΔI at a given bias voltage U_{SD}. The current change divided by the given voltage U_{SD} defines the photoconductance G_{photo}. b) The photocurrent I_{photo} is defined as the residual current at U_{SD}=0 V; the photovoltage U_{photo} is defined as the residual voltage at zero current respectively.

divided by the applied voltage. It is defined as photoconductance:

$$\Delta G = G_{photo} = \frac{\Delta I(U_{SD})}{U_{SD}}. \tag{1.3}$$

The entire conductance $G_{excitation}$ under radiation is composed of the conductance G_{off} without illumination and the photoconductance G_{photo} [63]:

$$G_{excitation} = G_{off} + G_{photo}. \tag{1.4}$$

The photoconductance effects a change in the slope of the IV-characteristics, but no shift along the y-axis as depicted in figure 1.5 a).

1.5 Nanoplasmonics

In the field of nanoscience a branch has emerged over the last 25 years which is named plasmonics. It describes, collective electron oscillations in the conduction bands of metals (see figure 1.6 a). Plasmons combine attractive properties of both optics and electronics [64]. Plasmons can be used to realize subwavelength optics by concentration and transport of light in nanostructures and provide strongly enhanced localized light sources on the molecular level for example in Raman and Fluorescence spectroscopy [64–68]. The longitudinal electron oscillations could be utilized for ultrafast data transport in future applications and supersede conventional electronics [64]. Plasmonics also plays an important role for the improved efficiency of solarcells [69] and organic or inorganic light emitting diodes [64]. As already defined in the beginning, plasmons are collective oscillations of electrons. Surface plasmons (SPs) are coherent oscillations bound to a metal-dielectric surface region. Photons coupling to an excitation in a medium e.g. phonons, plasmons or excitons can be treated as quasi-particles and are named polaritons. Thus, a photon interacting with surface plasmons at the dielectric-metal interface is called surface plasmon polariton (SPP).

1.5.1 Surface plasmon polaritons

SPPs propagate along the interface as waves (figure 1.6 a)) and are exponentially decreasing into both media as evanescent waves (figure 1.6 b)), thus SPPs have a two-dimensional character and are confined within the interface [66]. Due to the exponential decay of the SPPs with increasing distance of a metal (-dielectric) interface, they are often exploited in near-field imaging techniques [66]. The development of the scanning near-field optical microscope (SNOM) [70] (see section 1.6) enabled for the first time the visualization and study of SPPs properties in the near-field [66].

The expression of the wavenumber k_x for the propagation of SPPs along the x-axis as a function of the frequency ω, named dispersion relation, can be derived by solving the *Maxwell's equations* in both media taking into account the boundary conditions at the

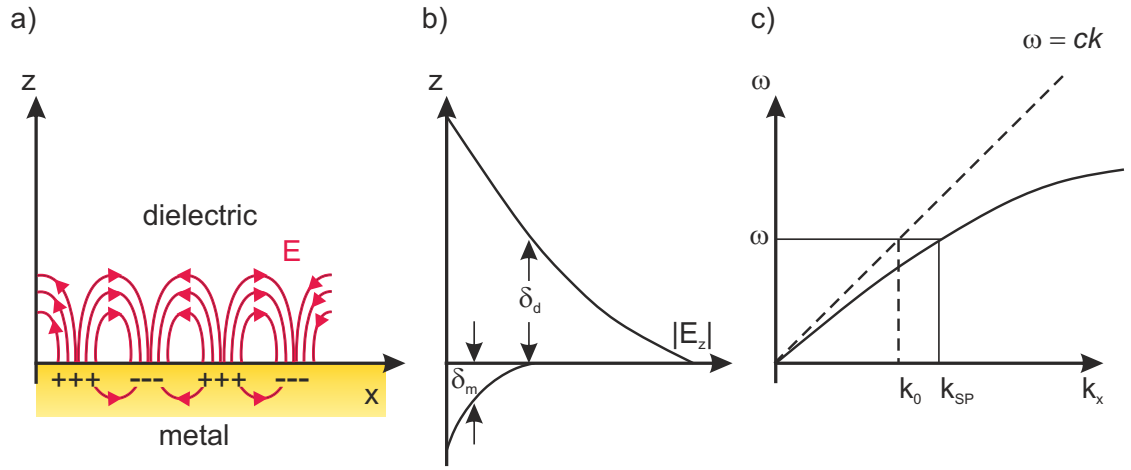

Figure 1.6: Basic properties of surface plasmons: a) SPs are electron oscillations confined within the dielectric-metal interface. The red curves show the electric field distribution in both media at a point of time. The electrical field strength decays exponentially with increasing distance to the surface. b) The decay length of the electric field component perpendicular to the interface in both media is depicted. In a dielectric this length is approximately half of the incident wavelength, whereas in metals the decay length is correlated with the skin depth. c) Disperion curves of light and SPs are visualized. Generally, a momentum mismatch prevents an excitation of SPPs by light at a metal-vacuum interface, as there is no crossing point of both curves. This problem can be overcome by usage of different configurations elucidated in the text. Figures adapted from [65].

interface [66]:

$$k_x = \frac{\omega}{c}\sqrt{\frac{\epsilon_d(\omega)\epsilon_m(\omega)}{\epsilon_d(\omega)+\epsilon_m(\omega)}}, \tag{1.5}$$

k_x is the wave-vector parallel to the surface. c is the velocity of light, $\epsilon_d(\omega)$ and $\epsilon_m(\omega)$ are the frequency dependent complex dielectric functions of the dielectric and metal respectively. $\epsilon_d(\omega)$ for glass and air can be set as positive dielectric constant ϵ_d, as it does not show a strong frequency dependency. Figure 1.6 c) visualizes the dispersion curve of SPPs in metal and the linear behavior of light with $k = \frac{\omega}{c}$ in air. When comparing both dispersion curves, the SPs show a larger momentum k at the same frequency; this momentum mismatch for direct excitation of SPPs by photons needs to be overcome [66]. It can be realized by either prism coupling in the Otto [71] or the Kretschmann-Raether [72, 73] configuration (see figures 1.7 (a)-(c)). Other possibilities are the use of SNOM probes (figure 1.7 (d)), diffraction gratings (figure 1.7 (e)) as well as rough metal surfaces [66]. One of the first experiments to excite SPPs were performed by Otto in an attenuated internal reflection (ATR) configuration [71]. As depicted in figure 1.7 (c) light is coupled through a glass prism under an angle of incidence Θ_{SP} that is greater than the critical angle for total internal reflection onto a metal film [66]. The prism and metal film are separated by a small, air filled gap of only a few nanometers. SPPs are excited if the following condition is fulfilled:

$$k_x = \frac{\omega}{c}\sqrt{\epsilon_d}\sin\Theta_{SP}, \tag{1.6}$$

then an evanescent wave can couple through the air interface to the metal and induce SPPs. This configuration is preferred when thick metal films are excited. In the Kretschmann-Raether set-up one plane of the glass prism is covered with a thin metal film, thus SPPs can be excited at the metal-air interface by an incident beam in the dielectric, for a sufficiently thin metal coating. Figure 1.7 (d) shows an aperture SNOM-tip, an optical fiber that is covered by a metal coating, with a small aperture at the end, where SPPs can be provided locally on the metal surface. Another way of SPP excitation can be achieved by diffraction gratings (figure 1.7 (e)). Diffracted light with an adequate wave-vector then provides SPPs on the metal surface. Another common SPP generation technique can be realized with randomly rough metal surfaces (figure 1.7 (f)). Illuminated metal STM-tips are based on this effect (see section 1.5.2). In contrast to the aforementioned configurations, no special conditions are required, due to the fact that in the optical near-field of the rough surface all wave-vector components of the diffracted light are present [66]. This technique is easy to realize, with the main drawback that the efficiency of SPP generation is very low as it is a nonresonant excitation compared to the Otto or Kretschmann-configuration were SPPs are generated under the resonant conditions of the equation 1.6. Rough metal surfaces are strongly correlated with another subtype of plasmons, named localized surface plasmons

(LSP). LSPs are mainly found in metal particles of various sizes and geometries, which can be excited by light of distinct plasmon resonance frequencies ω_{LSP} [74].

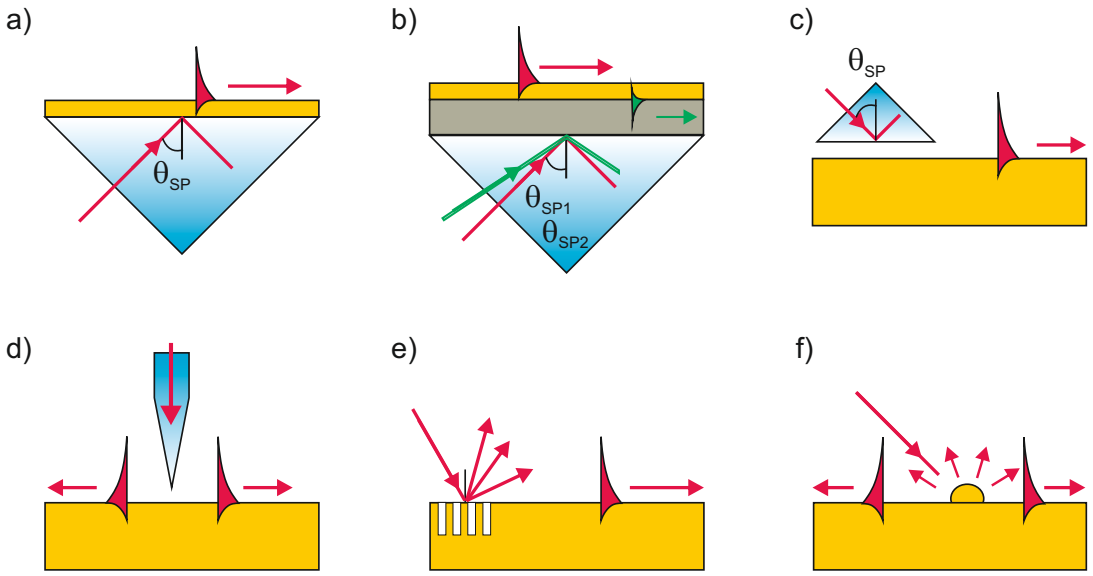

Figure 1.7: Different configurations for the excitations of SPPs: (a) Kretschmann geometry with one layer and two layer geometry (b). (c) Otto configuration. (d) Fiber SNOM-tip for the local excitation of SPPs. (e) A diffraction grating on a smooth metal surface is another technique for SPPs generation. (f) The easiest way to excite SPPs can be realized by illumination of a rough metal surface. Figure adopted from [66].

LSPs resonances decay efficiently into light. Due to the localized character of the LSPs, a strong light confinement is achieved, thus an enhancement of the incident optical field by several orders of magnitude can be obtained [75].

1.5.2 Plasmonic field enhancement mechanisms

The starting point for the estimation of plasmonic field enhancement was given by the results observed by Fleischmann et al. in 1974 [76, 77]. In their experiments Fleischman studied Raman spectra of pyridine molecules on a rough silver surface with a surprisingly high intensity of the measured Raman signal. Raman scattering is an optical spectroscopy based on inelastic light-scattering to investigate vibrational modes of a material. This technique is named after the physicist Raman, who was the first to observe this effect [78]. Each material has specific vibrational modes, which are chemical fingerprints that can be accessed by this technique. At that time it was claimed that the increased Raman intensity

might originate from an increased surface area due to the roughened silver surface [76]. In 1978 Moskovits [79] proposed that the unexpected high Raman signal could originate from LSP excitations. From thereon this effect was termed surface enhanced Raman spectroscopy (SERS). The low scattering cross-section of conventional Raman spectroscopy which is in the order of $10^{-27} - 10^{-32} \frac{1}{\mathrm{cm}^2}$ can be increased with SERS up to the order of $10^{-18} \frac{1}{\mathrm{cm}^2}$, the minimum scattering cross-section for the detection of Raman signal from single molecules [77, 80, 81].

Optical field enhancement through surface roughness

The aforementioned SERS effect is based on the fact that surface roughness on metal substrates can induce an enhancement of the incident optical field by several orders of magnitude. It has been demonstrated that for the detection of Raman scattering in the single molecular level "hot spots" play a leading role. These surface inhomogeneities are assumed to induce giant optical fields, sufficient for the detection of Raman fingerprints from single molecules adsorbed on the surface [77].

Optical field enhancement through tip geometry

An additional way to take advantage of field enhancement is the utilization of a metallic probe with an extremely sharp geometry. The *lightning rod effect* known in electrostatics induces a field enhancement at the apex of the tip ("field line crowding") [82]. Based on this effect tip enhanced Raman Spectroscopy (TERS) has become an alternative technique for the detection of Raman signals and has been demonstrated for example on single wall carbon nanotubes (SWCNT) [83]. The field enhancement caused by the *lightning rod effect* is strongly influenced by the polarization of the laser beam, as SPPs are excited on the rough metal surface of the tip, propagating towards the apex of the tip. Thus TERS can be considered as a subtype of SERS. The enhancement in TERS can be quantitatively determined by comparison of the signal strength in tunneling contact and with the tip retracted [84, 85].

Calculation of the field enhancement factor

In the scope of plasmonics, TERS and SERS it is common to specify a field enhancement factor derived from experimental data or from theoretical approaches [77]. The enhancement factor g is derived from the ratio between the local electric field and the electric field of an incident laser beam:

$$g = |\frac{E_{local}}{E_{incident}}| \tag{1.7}$$

This value is in the order of 10-1000 depending on the experimental configuration, the probe and substrate material, its surfaces properties and the geometry [77]. The light intensity is proportional to $|E^2|$.

1.6 Scanning near-field optical microscopy

Scanning near field optical microscopy (SNOM) was introduced by Pohl et al. [70] and Lewis et al. [86]. It is a scanning probe technique based on the combination of optical spectroscopy and microscopy [82]. For the first time it was possible to circumvent the classical diffraction limit calculated by Rayleigh and Abbe [82]. Thus it became possible to probe chemical characteristics, topographic and optical information directly with the optical near-field [66]. Basis of this technique is a confined light source which is moved on top of a surface, probing the optical properties. In the near-field non-propagating electromagnetic waves decay exponentially with increasing distance to the interface. The evanescent waves are a solution of *Maxwell's equations*, with at least one component of the wave-vector getting complex, therefore decreasing exponentially. The easiest way to generate an optical near-field is realized with a light beam incident to a dielectric with an refractive index n_2 higher than the refractive index in air (n_1) with the critical angle of total internal reflection. Different experimental approaches have been developed over the last two decades. The two mainly used in SNOM are aperture probes (a-SNOM) and apertureless or scattering type SNOM probes (s-SNOM) in different configurations and operation modes. The (a-SNOM) probes are most commonly optical fibers coated with a metal film and small opening at the apex. The one end of the fiber is illuminated by a laser beam, the aperture at the apex acts then as a local light source. The disadvantage is the low transmission at the aperture, thus a weak evanescent field is generated, while on the other hand the background radiation is suppressed [75]. The alternative probes are bare metal tips (s-SNOM) that are illuminated from the far field. By scattering of light at the apex of the tip near-field information is transferred to the far-field. The advantage of this (s-SNOM) type probes is a high confinement and enhancement at the apex, but the background noise due the far field illumination is orders of magnitude higher [75, 82].

1.7 Photosystem I

1.7.1 Introduction to photosynthesis

From a biological view the oxygenic photosynthesis evolved about 3.5 billions years ago in simple ancestors of todays cyanobacteria, with oxygen as a reaction product [87,88]. Due to a continuous production of oxygen, the oxygen level of earths' atmosphere and the oceans

was slightly increased over 2 billion years up to a level where advanced animal life could develop [87,89]. The evolution of photosynthesis marks a seminal point for the development of life. In a more physical/chemical picture photosynthesis is a very efficient photochemical reaction that converts solar energy into stable chemical energy, like glucose and other vital organic substances. Photosynthesis evolved along different pathways in higher plants, algae and certain bacteria, today the main contributors in the generation of oxygen and biomass. On the molecular level the process of solar energy conversion is given by the following overall net reaction-equation:

$$6\ CO_2 + 12\ H_2O \overset{light}{\rightarrow} C_6H_{12}O_6 + 6\ H_2O + 6\ O_2$$

CO_2 taken of the earths' atmosphere together with light and water is transformed into carbohydrates and oxygen. Figure 1.8 shows 4 protein-complexes consisting of photosystem II (PS II), cytochrome b_6f, photosystem I (PS I) and NADP-reductase that are involved in the light-driven photosynthetic reaction in a cyanobacterium embedded along the thylakoid membrane. Following photon absorption, PS II extracts electrons from H_2O that is present in the thylakoid membrane [87]. The electrons then pass a quinone cycle as well as the cythochrome b_6f protein complex, where the electrons are transferred to plastocyanin, a soluble electron carrier protein. Plastocyanin finally docks to the PS I as electron donor [87]. In PS I photon energy is absorbed by a chlorophyll antenna complex inducing an charge separation and guiding the charge along the so called electron transport chain (ETC). At the end of the transfer process of the central electron transport chain ferrodoxin, a redoxprotein complex, is reduced by the electrons. Consecutively NADPH is produced at the NADP reductase together with the electrons and H^+ ions. NADPH is a basic module for the synthesis of cellular components [87]. During the whole photosynthetic reaction process a proton gradient across the membrane is generated powering the production of ATP, a multifunctional molecule not only for energy storage, but also the base of all energy consuming processes of advanced life forms. A detailed description of the photosyntetic reaction, including light and dark reactions can be found in the book of Berg et. al [90]. The main role of the combination of PS I and PS II is the light induced charge separation that provides highly energetic electrons. These electrons enable the buildup of carbohydrates, whereby water as an electron donor is photooxidized and oxygen is produced [91].

1.7.2 The structure of the cyanobacterial Photosystem I

The PS I investigated in this thesis is extracted out of the thylakoid membrane of cyanobacteria [92,93]. In contrast to plants PS I, where only a monomeric form has been observed, PS I in cyanobacteria exists primarily *in vivo* as a trimer with a relative molecular mass $M_r = 3 \times 356,000\ Da$ [94–96]. A PS I monomer has a height of approximately 9 nm

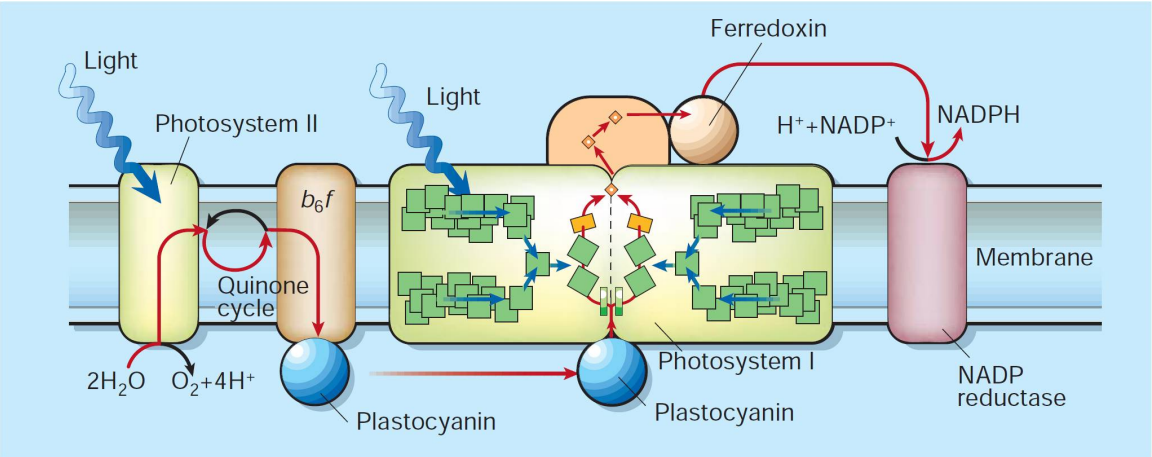

Figure 1.8: Sketch of molecular components contributing to the oxygenic photosynthetic reaction embedded in the thylakoid membrane of a cyanobacterium. [adopted from [87]].

and width of 15 nm. Figure 1.9 visualizes the molecular structure of the cyanobacterial PS I [94]. One PS I monomer complex is composed of 12 subunits, named as *PsaA-F, PsaI-M* and *PsaX* [94]. Additional to the 12 protein subunits each monomeric unit consists of 127 cofactors containing 96 chlorophylls, 22 β-carotenoids, 3 [4Fe-4S] clusters, 2 phylloquinone molecules and 4 lipids [94, 97]. The heterodimeric core of the PS I comprises the two biggest subunits *PsaA* and *PsaB* [98], including 79 of the 90 antenna cholorophylls [94, 97]. Furthermore *PsaA* and *PsaB* coordinate the primary electron donor *P700*, the initial electron acceptor A, the primary electron acceptor A_0, the secondary electron acceptor A_1 named as phylloquinone also known as vitamin K_1 [99] and the tertiary acceptor F_X, the majority of cofactors participating in the electron transfer [94, 97, 99] shown in figure 1.11. The extrinsic *PsaC* subunit binds two [4Fe-4S]clusters, the terminal acceptors named as F_A and F_B [94, 97]. For the electron transfer from PS I to ferredoxin the subunits *PsaD* and *PsaE* are crucial [97, 99], while the remaining subunits are mainly structuring and stabilizing the heterodimeric core (*PsaF,PsaJ,PsaK,PsaX*) or the monomer-monomer interface (*PsaL*, *PsaI*, *PsaM*) [94, 97].

1.7.3 Optical properties of the Photosystem I

The core antenna system is responsible for the efficient light trapping and energy transfer to the electron transport chain. In cyanobacterial PS I the core antenna system contains 90 chlorophyll *a* molecules (*Chl a*) and 22 β-carotenoids in different spectral forms [94, 99]. The chlorophyll species (*Chl b*) is also present in plants PS I. Figure 1.8 visualizes the principal conformation of the chlorophylls around the heterodimeric core. The so called

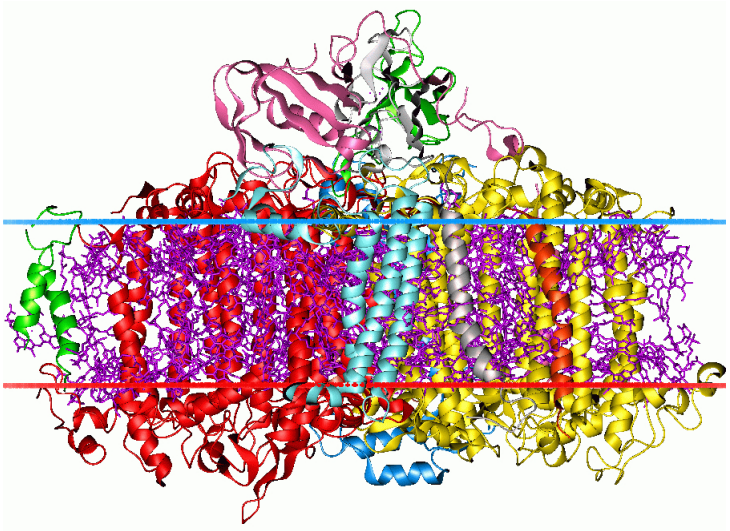

Figure 1.9: Structure of a cyanobacterial photosystem I monomer: The blue and red horizontal lines mark the upper and lower end of the thylakoid membrane in which the photosystem I is embedded. The pink, yellow, blue, gray, red and green α-helical molecules are polypeptide subunits. The whole PS I consists of 12 protein subunits. Chlorophylls and carotenoids colored in violet are responsible for an efficient absorption of the solar energy. [adopted from [94]].

central domain surrounds the electron transport chain [94, 97]. Two chlorophyll clusters, one situated at the lower boundary, the second at the upper boundary of the membrane flanking the core and form the peripheral domain [94, 97]. The carotenoids are found in both domains [94, 97]. Nearly all of the *Chl a* molecules have a distance of less than 15 Å to several of their next neighbors, enabling a very efficient Förster type excitation energy transfer to the center of the PS I complex [94, 100]. PS I shows two distinct absorption maxima around 400 nm (see figure 1.10), the so called B-band (Soret-band) around 630 nm and 680 nm the Q-band [101]. Depending on which is incorporated (*a* or *b*) the maxima position of the absorption peaks vary. Carotenoids extend the absorption of light harvesting in the range of 450-570 nm [94]. Even at wavelengths beyond 700 nm a few *red* chlorophylls absorb light [94, 99].

1.7.4 The electron transport chain and transport through single Photosystem I proteins

All cofactors that are involved in the spatial charge separation along the electron transport chain (ETC) inside the PS I reaction center are shown in figure 1.11. The ETC, along which photoexcited electrons are guided, is composed of 6 chlorophylls *Chl a* combined as dimers ($P700, A, A_0$), two phylloquinones (A_1) and three iron-sulfur clusters (F_X, F_A, F_B) [97].

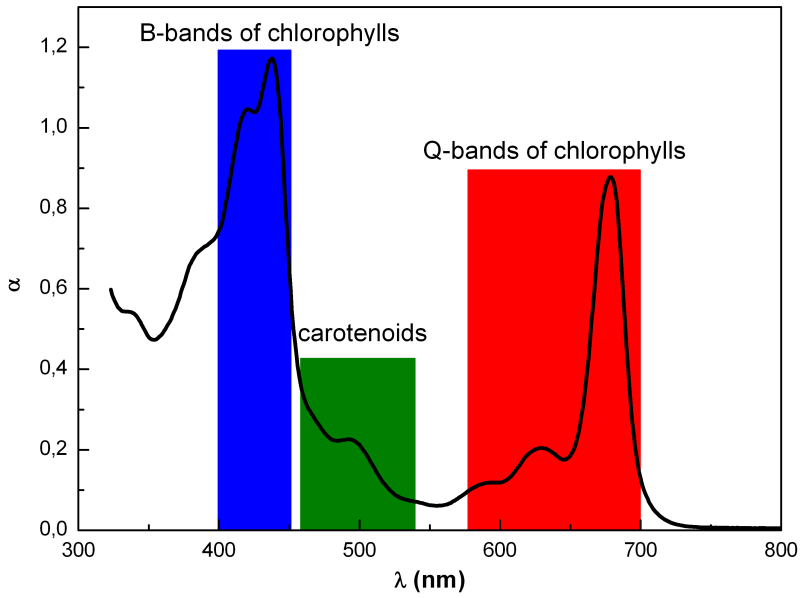

Figure 1.10: Absorption spectrum of PS I: Two absorption maxima at around 420 nm and 440 nm as well as two maxima around 630 nm and 680 nm are associated with the chlorophylls, while a shoulder between 450-530 nm originates from the carotenoids. Figure adopted with permission from [102].

Hereby the chlorophylls and phylloquinones are arranged in two branches A and B [94]. Whether both branches are active or only one branch enables the electron transfer is still not fully understood [94, 103]. As mentioned in section 1.7.3, the photon energy is transferred via Förster energy transfer to the core of the reaction center, in particular to the special pair of chlorophyll a $P700$. Here the $P700$ is optically elevated to an excited singlet-state $P700^*$, with a minimum energy of 1.77 eV that is required for the excitation. In the following one electron is guided from $P700^*$ through one of the $Chl\ a$ of the dimer A to one $Chl\ a$ of the primary electron acceptor A_0 in less than 5 ps (see figure 1.12). In the next step along the ETC one of the phylloquinones of the dimer (A_1) is passed within approx. 30 ps. Subsequently the electron is transferred to the first F_X, the second F_A and the third F_B iron-sulfur cluster in less than 200 ns. The spatial distance between $P700$ and the final electron acceptors $F_{A/B}$ is about 6 nm, with a positive charge at the oxidizing and an electron at the reducing side of the PS I. At the end of the ETC ferredoxin is reduced while plastocyanin docks to the oxidizing side acting as a electron donor for $P700$ (see figure 1.8). In case of suppressed charge transfer to the ferredoxin due to a lack of ferredoxin or other reasons a charge recombination between $P700^+$ and the final electron acceptors $F_{A/B}$ takes place within an approx. recombination half-time of 10 ms [103]. The standard free energy difference between the excited state $P700^*$ and the final state $P700^+F_B{}^-$ (see figure 1.8) is 1 eV, that corresponds to an energy yield of nearly 60 percent with respect to the minimum

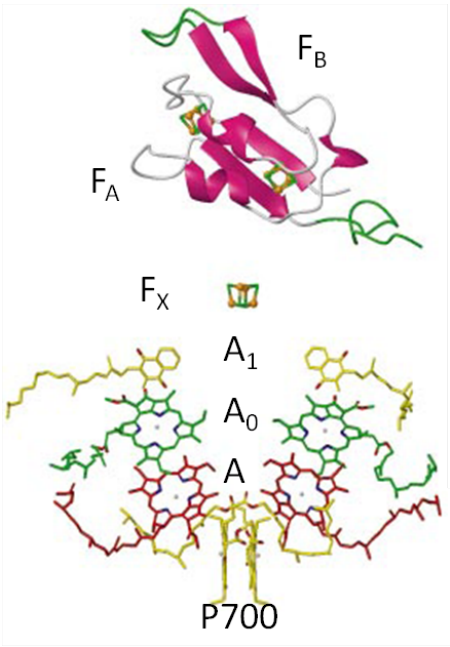

Figure 1.11: Cofactors of the electron transport chain: 6 chlorophylls (*Chl a*) combined as dimers ($P700, A, A_0$), two phylloquinones (A_1) and three iron-sulfur clusters (F_X, F_A, F_B) form the electron transport chain. The chlorophylls and phylloquinones are arranged in two branches. Figure adopted from [94].

photon excitation energy of 1.77 eV (700 nm) [99]. Also the internal quantum efficiency is close to 1, meaning that almost every adsorbed photon effects a charge separation, presumed that no recombination occurs [95, 99]. The photosystem can be considered as an optically excited electron pump, where the electron energy along the ETC over time shows a staircase behavior, as hinted in figure 1.12. These properties make the PS I a promising candidate for technological applications.

1.7.5 Genetically mutated Photosystem I

The discovery of the site-directed mutagenesis in a DNA sequence in 1978 by Hutchison et al. [104] allowed for the first time to modify specific peptide-groups in bacteria. With this tool the structure/folding of a protein can be changed and together with a change of its specific properties, conclusions can be drawn from the function of the modified peptide-groups inside the protein. Studying optoelectronic properties like photocurrent or photodiodic behavior of PS I requires the immobilization of the PS I proteins by covalently binding them to an interface. One possibility to realize the immobilization of PS I is achieved by site-directed mutagenesis. The mutations have to be chosen in a way that the full functionality of PS I, meaning light trapping, energy transfer to the reaction center and charge separation

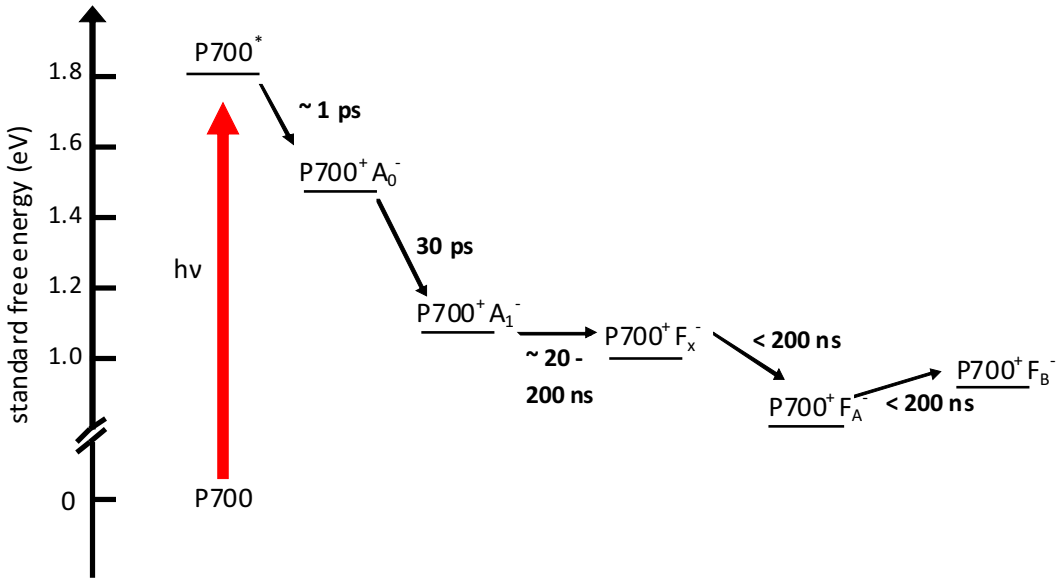

Figure 1.12: Standard free energy levels during the charge separation in PS I. The red arrow represents the electron excitation in *P700*. Figure adopted from [103].

within the electron transport chain, is preserved.

1.7.6 Integration of Photosystem I to biomolecular devices

In the following section a brief overview is given about the integration of PS protein complexes into biomolecular nanodevices within the last fifteen years. This research field is attracting increased attention due to its potential in various fields of possible applications as hybrid devices like biosensors and organic solarcells as well as water-splitting-based hydrogen producing applications [105, 106] . A prequisite for a device is the immobilization of isolated PS I proteins on substrates. First experiments on this field were done by Lee et al. 1996 [107] under helium atmosphere at room temperature, where PS I molecules are anchored by chemical platinization onto gold substrates. Also the orientation of the PS I can be controlled via chemical preparation of derivatized gold surfaces, shown by Lee et al. 1997 [108]. Ciesielski et al. [109] demonstrated in 2008 with functionalized nanoporous gold leafs (NPGL) the immobilization of PS I. The NPGLs surface is modified with aldehyde terminal groups to which exposed lysine residues on PS I bind covalently to the NPGL surface. Another way to immobilize PS I is the mutagenesis of distinct amino groups along the PS I, as mentioned in section 1.7.5. In 2004 Das et al. [110] introduced peptide surfactants for the stabilization of PS I outside the native environment. Subsequently the *PsaD* subunit of PS I is exchanged by a genetically mutated His_6 tagged *PsaD* that binds to a functionalized gold surface. A more specific mutagenesis was developed by Frolov et al. in

2005 [92]. Amino groups with no steric hindrance when bound to a gold surface are changed to cysteine groups that form a sulfur bond to gold or to functionalized semiconductors like GaAs [111]. The first solid-state devices that integrate PS I complexes were reported by Das et al. [110], where the above mentioned His_6 tagged *PsaD* proteins are covered with an tin-doped indium oxide (ITO) coverlayer. A "wet" photoelectrochemical device including PS I implemented into a FET was published by Terasaki et al. [112]. Kaniber et al. [28] achieved to functionalize a PS I carbon-nanotube hybrid system onto a chip. The PSI-CNT hybrids are integrated into a macroscopic circuit with a source and drain contact on which a voltage V_{SD} is applied. An objective focuses the light of a Ti:Sapphire laser onto the device. The current difference between "on" and "off" is recorded. These wavelength-dependent photoconductance measurements (see figure 1.13 a) revealed a photoconductance enhancement at around 360 nm and 680 nm in a PSI-CNT bundle, which is in agreement with absorbance measurements of PS I in solution (see red curve in figure 1.13 a). The enhanced photoconductance can be explained by an electron or energy transfer between CNT and the excited PSI [28, 113]. In figure 1.13 c) PSI is bound by an electrostatic interaction to the CNT, still showing an enhancement in photoconductance at around 680 nm whereas in sample D, the ETC of the PS I is electrostatically adsorbed and oriented parallel to the CNT thus energy and electron transfer from PS I to CNT is less efficient. In summary these experiments show, that cysteine mutated PS I is still optoelectronically active, retaining its aforementioned functionality.

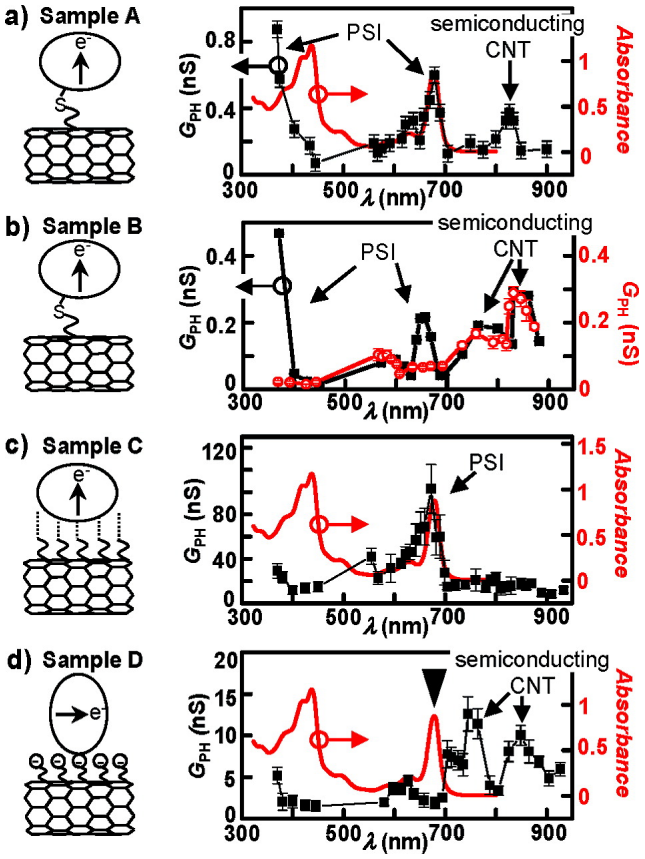

Figure 1.13: PSI-SWCNT-hybrid system: Depending on the orientation of the ETC with respect to the CNT and the binding between CNT and PSI the photoconductance G_{PH} and wavelength dependent absorbance differs. (a) ETC of PS I perpendicular to CNT orientation, covalently bound to CNT due to a sulfur-bond. The graph shows the absorbance (red) and photoconductance (black) G_{PH} with both having a maximum around 680 nm. (b) G_{PH} recorded before functionalization with PS I (black) and after (red), the peak at 680 nm can be referred to electron or energy transfer from PS I to the CNT. (c) In sample C the PS I is bound electrostatically to the CNT, still showing a maxima in the absorbance and G_{PH}. (d) In contrast to sample D, where the ETC is oriented parallel to the CNT. The absorbance maxima at 680 nm due to PS I remains, while the maximum in G_{PH} vanishes. [adopted from [28]]

1.8 Lightwave electronics

Lightwave electronics is a new research field that was first dubbed by Goulielmakis et al. in 2007, targeting to excite bound electrons and to steer the collective motion by the electrical field of ultrashort laser pulses [114, 115]. The time and length scale of electronic processes in atoms or molecules is often confined to the subfemtosecond respectively Angstrom scale [115]. For a temporal access to this subfemtosecond time scale, tools are required that enable the "real-time" observation of electron dynamics in a stable, reproducible and controllable way. The development of the attosecond laser near single cycle pulse generation opened the door for the study time-resolved electron motion in atoms, molecules or condensed matter [114–121]. The main parameters for the generation and control of femtosecond laser pulses are exemplified in the following subsections. The solid-state system experimentally probed by these ultrashort laser pulses (subsection 1.8.2) and possible charge injection mechanisms are introduced and the mathematical calculation of the charge carriers injection is described (subsection 1.8.4).

1.8.1 Fundamentals of femtosecond light pulses

Here, the fundamental concepts of femtosecond light field control are exposed, a detailed description on ultrashort laser pulses can be found in the books of Chang [122] and Diels [123]. Ultrashort light pulses are mathematically defined by time- and space-dependent electric field $\vec{E}(\vec{x},t)$, while their propagation can by described by *Maxwell's equations*. In this introduction we neglect the spatial term, then the electric field of a linearly polarized pulse as a function of time in the time domain is:

$$E(t) = A(t) \cdot \cos(\omega_L t + \varphi(t)), \tag{1.8}$$

where *A(t)* is the time-dependent electric field amplitude, ω_L the carrier frequency and $\varphi(t)$ corresponds to a temporal phase-function. For a Gaussian pulse the electric-field amplitude is

$$A(t) = E_0 \cdot e^{\,2ln\ 2\left(\frac{t}{\tau}\right)^2}, \tag{1.9}$$

where E_0 is the electric peak amplitude and the pulse duration τ is the full width at half maximum of the Gaussian envelope. The peak intensity I_0 at the center of a Gaussian beam pulse is correlated with the laser power P

$$I_0 = \frac{1.88}{\pi} \frac{P}{w^2 \tau f_{rep}}, \tag{1.10}$$

with the repetition f_{rep} rate of the laser and the beam waist w. The waist is defined as the radius where the intensity I decays to I_0/e^2. By measuring the laser power and the beam

size the electric field amplitude can be determined as $I = \epsilon_0 c E_0^2$.

Temporal phase, carrier-envelope offset phase and chirping

In equation 1.8 we introduced **the time dependent phase-function** $\varphi(\mathbf{t})$. The phase offset between the maximum of the Gaussian envelope and the maxmimum of the electric field amplitude is defined as **carrier envelope offset phase** (CEP), when the phase is stationary. In figure 1.14 the time-dependent electric field for $\varphi_{CE} = 0$ and $\varphi_{CE} = -\pi/2$ are depicted. The cosine-pulse ($\varphi_{CE} = 0$) shows one maximum for $t = 0$, whereas the maximum for the sine-pulse ($\varphi_{CE} = -\pi/2$) is smaller and shifted towards the positive timescale. If the temporal phase is a quadratic function in time $\varphi = bt^2$, the instantaneous frequency for a given time t is defined as:

$$\omega(t) = \frac{d}{dt}(\omega_L t \ + \ \varphi(t)) = \omega_L \ + \ 2bt. \tag{1.11}$$

b is the chirp parameter, for $b<0$ the pulse is negatively chirped. For this case the instantaneous frequency under the Gaussian envelope is decreased over time as depicted in figure 1.14 c). Respectively for a positive chirp $\omega(t)$ is increased over time. By insertion of dispersive media into the beam path of the laser pulse the CEP is changed and the pulse is chirped.

Pulse propagation in dispersive media

When ultrashort pulses propagate in dispersive media as for example fused silica, the CE-phase is shifted:

$$\Delta\varphi_{CE} = \varphi_{CE}(z) - \varphi_{CE}(z = 0) = \left(\frac{1}{v_g(\omega_L)} - \frac{1}{v_p(\omega_L)} \right) z\omega_0. \tag{1.12}$$

z corresponds to the propagation length in the dispersive media. As the equation 1.12 indicates, the CE-phase shift is caused by the difference of the group and phase velocities v_g, v_p in the dispersive media. For large propagation length the pulse gets temporally broadened or compressed. The resulting pulse duration τ_{chirp} at the outcome of the dispersive media, within a propagation length z is

$$\tau_{chirp} = \tau_{in}\sqrt{1 + (\frac{\Delta z}{L_D})^2}, \text{with the dispersion length } L_D = \frac{\tau_{in}^2}{2D_\omega}. \tag{1.13}$$

τ_{in} is the initial pulse duration at z = 0 and D_ω is the group velocity dispersion (GVD).

$$D_\omega = \frac{\partial^2 k}{\partial \Omega^2}|_{\Omega=\omega_L} \equiv \frac{d}{d\omega}\left(\frac{1}{v_g}\right). \tag{1.14}$$

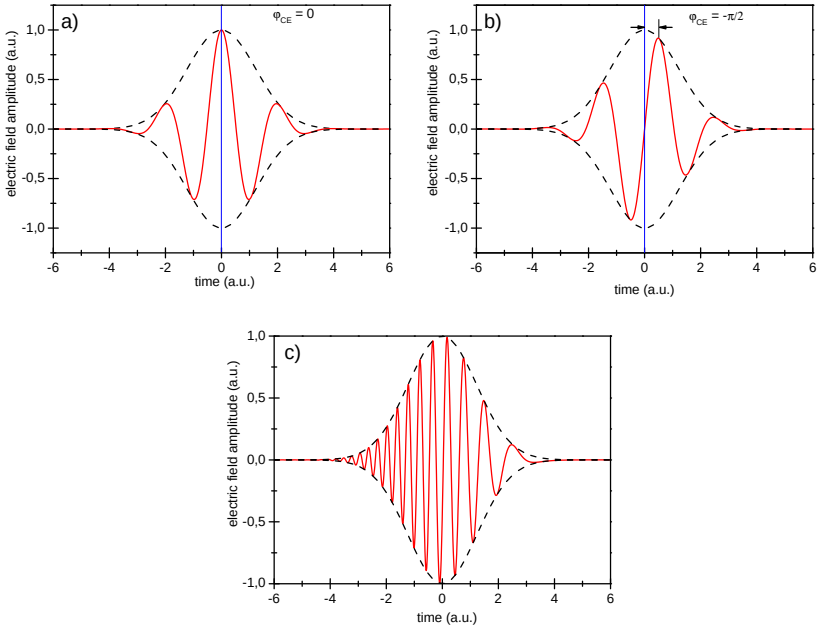

Figure 1.14: Sketches illustrating the basic properties of ultrashort near-single cycle optical pulses. The carrier- envelope phase defines the temporal structure of the electric field of the pulse relative to its envelope. a) Electric field for $\varphi_{CE} = 0$, a cosine pulse, as the amplitude of the electric field is at maximum for t = 0. b) Electric field for $\varphi_{CE} = -\frac{\pi}{2}$ is named sine pulse, as the symmetry is equal to a sine wave at t = 0. c) A chirped pulse, where the frequency of the enveloped pulse decreases over time.

1.8.2 Optically-induced charge carrier excitation in a dielectric

The experimental approach aims to study the mechanisms of charge carrier generation and control of the collective charge motion in a dielectric embedded between two metal electrodes by ultrashort CEP-stabilized near single-cycle optical pulses. To study these mechanisms in the picture of ballistic electron transport, with a mean free path on the order of nanometers, we use nanostructures (see figure 1.16). The CEP is expected to be the fundamental control parameter in the experiments discussed in section 3.3. This experimental approach is analogous to the streaking experiments of atoms in the gas phase [116] or at the solid interface [119], where electrons are excited above the vacuum level with synchronized attosecond XUV-pulses and subsequently accelerated by NIR-pulses. Here, the goal is to

excite and imprint a net momentum change to electrons within a dielectric. The measurement parameter in this concept (see figure 1.15) is the net current between metal electrodes as a summation of the collective electron motion inside the dielectric. Experimentally it is expected that the absolute value of the net current is dependent on the CE-phase of the optical pulse.

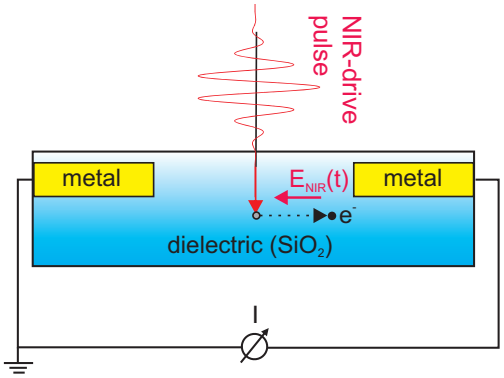

Figure 1.15: Principle set-up for the experimental approach towards the streaking of electrons in a solid-state device.

The properties of silicon dioxide as well as some excitation processes that qualify as possible mechanisms are discussed in the following chapter.

1.8.3 Optical and electronic properties of silicon dioxide

Silicon dioxide (SiO_2) is a dielectric, widely employed in semiconductor technology as an insulator due to its specific electronic and optical properties; it is also the principal component of glass. The three mainly existing condensed appearances are the amorphous SiO_2 (a-SiO_2), the α-quartz ($\alpha - SiO_2$), while the third manifestation β-quartz ($\beta - SiO_2$) is only stable at temperatures above 500 K [124,125]. Amorphous (a-SiO_2) has no long range order compared to the crystalline α-quartz. The different conformational structures of both manifestations marginally influence the electronic properties [125]. The calculated energy band gap between the valence band (VB) and the conduction band (CB) for both structures is on the order of 9 eV [125, 126], which defines SiO_2 as an insulator. Only if the electrons overcome (e.g. by photon absorption) the 9 eV direct band gap energy, the conduction band gets populated and the material becomes conductive. The scattering time for silica was calculated to about 2 fs for electron energies of up to 3 eV [127]. Simulations on the electron dynamics in $\alpha - SiO_2$ in the presence of ultrashort, strong optical fields performed by Otobe et al. [128] revealed an optical breakdown in the dielectric for intensities above $2.5 \times 10^{15}\ \frac{W}{cm^2}$. It is assumed that a critical electron density in the conduction band needs to be overcome to induce this breakdown effect [128, 129]. Experimentally this avalanche

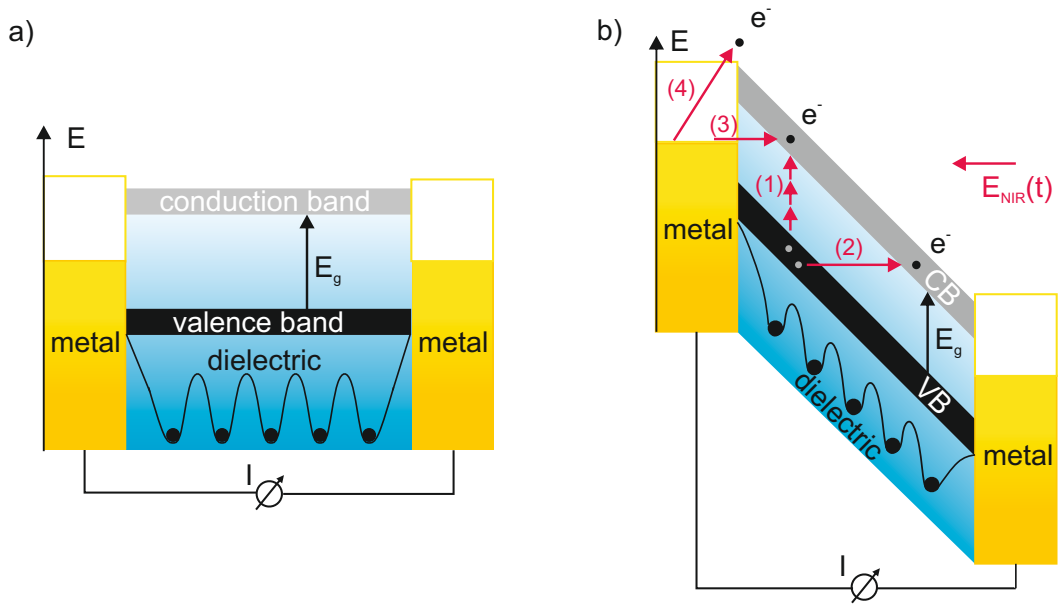

Figure 1.16: Energy band-diagram of the metal-dielectric-metal nanojunctions investigated in this thesis with ultrashort laser pulses. a) Nanojunction without laser excitation. b) Energy diagram of the hybrid junction under the exposure of an intense optical field. The illustration of the bent energy levels represents the energy levels exposed to a strong electric field, i.e., the lower energy electronic states are located in the opposite direction of the field. This is a picture at a given time. When the field is time-dependent, as it is the case when a optical waveform is present, the electronic levels are 'flipping'. The energy bands in the dielectric are bent. Four possible mechanisms for the charge carrier excitation are depicted, which are (1) Multiphoton excitation, (2) Zener/Keldysh interband-tunneling, (3) Fowler-Nordheim tunneling, (4) Photoemission.

like breakdown has been demonstrated by Du et al. for laser pulses between 150 fs and 7 ns [130]. The laser intensities for our experimental approach are located in this breakdown regime, but theoretical calculations indicate that this effect is suppressed for the pulse durations of approx. 4 fs employed in our experimental approach [131]. In the regime of few-cycle laser exposure in the VIS/NIR experimental data for bulk fused silica showed that we are well below the breakdown regime [132].

Photoemission

Linear photoemission is one of the possible mechanisms to cause current flow in a nanoscale metal-dielectric-metal junction (see figure 1.16 b):(4)). Since the laser beam spot-size is expected to be larger than the gap between the electrodes, an asymmetric illumination of the metallic electrodes can lead to a macroscopically detectable current. Photoemission is an excitation mechanism that is based on the photoelectric effect. By irradiation of light with a photon energy $E_{photon} = h\nu$ that is larger than the work-function W of a given metal, electrons can be emitted from the surface. The electron is excited by the photon above the vacuum level E_{vacuum} and escapes the surface after overcoming the metal work-function W. The remaining kinetic energy E_{kin} of the photo emitted electrons is given by

$$E_{kin} = h\nu - E_{binding} - W, \tag{1.15}$$

where $E_{binding}$ is based on the Fermi level E_F. The energy difference between E_{vaccum} and E_F defines the work-function W.

Multiphoton excitation

Multiphoton excitation is a possible injection mechanism of charge carriers in the solid state. For sufficiently high optical fields electrons can get excited from the valence band to the conduction band as depicted in figure 1.16 b):(1), even if the energy of a single photon is to small to overcome the energy difference between the energy levels [133]. By the absorption of several photons, the energy gap can be overcome, thus electrons can populate this energy band. The probability $P(n)$ for the absorption of n photons as a function of the intensity I is given by [133]

$$P(n) \propto I^n. \tag{1.16}$$

In case of multiphoton ionization, when electrons are excited above vacuum level, the kinetic energy after the absorption of n photons is given by

$$E_{kin} = nh\nu - I_p, \tag{1.17}$$

where I_p is the ionization potential.

Zener/Keldysh interband tunneling

Zener derived a description for the interband tunneling of electrons in the presence of a strong DC-electric field E_{ext} [134]. In figure 1.16 (2) the Zener tunneling mechanism is depicted. In the case where the external electric field bends strong enough that the VB and CB are degenerate, electrons can tunnel through the reduced energy barrier. Zener deduced a tunneling rate per second:

$$\Gamma_{Zener} = \frac{eE_{ext}a}{h} exp\left(-\frac{\pi^2}{h^2}\frac{m_e a E_{gap}^2}{|eE_{ext}|}\right) \tag{1.18}$$

Here, m_e is the reduced electron mass in the SiO_2 and a is the periodicity of the potential energy given by the lattice. For the calculation of the tunneling rate in SiO_2 in the presence of an ultrashort pulse as visualized in figure 1.17, a is approximated by the lattice constant of α-quartz. Keldysh extended this model to AC-fields in 1965 [135]. The transfer time

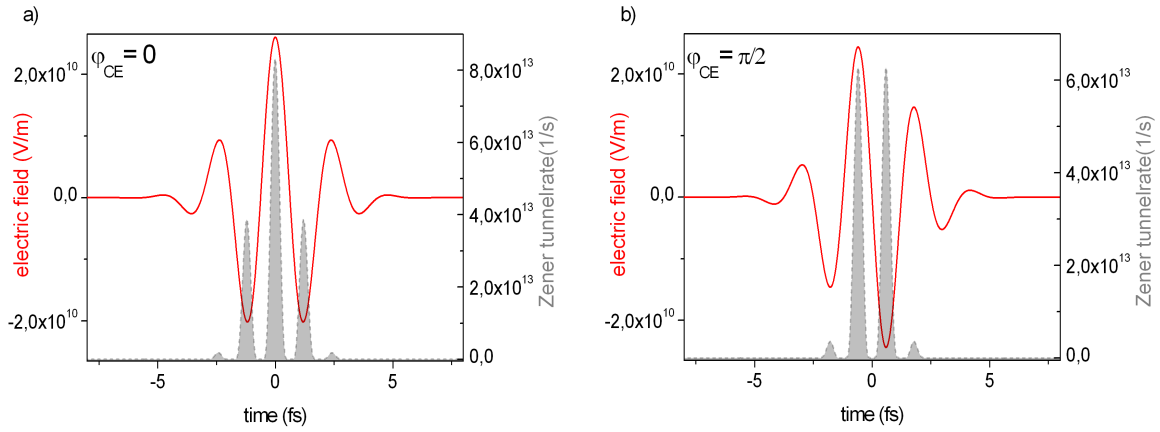

Figure 1.17: Charge carrier injection rate calculated for Zener-interband tunneling for a near single cycle NIR pulse and two values of the CE-phase. Clearly evident in this simulations is the sensitivity of the injection rate to the CE-phase of the pulse. The charge carrier generation depends exponentially on the electric field, this implies that a significant charge carrier generation to the CB occurs at maximum field strength. a) CE-phase set to $\varphi_{CE} = 0$. b) $\varphi_{CE} = \pi/2$: The maximum electric field strength for both simulations is $2.6 \cdot 10^{10}$ V/m.

for electrons from the VB to the CB can be estimated to be on the order of tens of 100 as. As the experimentally provided NIR-pulses are in the range of 4 fs, we can assume that the DC-field model by Zener is adequate for the numerical calculation of the tunneling rate. As a consequence we can use the instantaneous electric field E(t) of the pulse for the

parameter E_{ext}. Two simulations for the tunneling rate of the Zener model with different CEP are shown in figure 1.17. The charge generation rate is determined by the structure of the pulse, meaning the CEP and the field strength. The probability of excitation given by Zener depends exponentially on the field magnitude, therefore significant carrier generation occurs when the field is maximum. Thereby the time of excitation is determined by the CEP, triggering the peak height.

The Keldysh parameter

In the above mentioned paper Keldysh derived a description for the ionization in a solid state system exposed to strong electromagnetic AC-fields. Keldysh distinguished the ionization between multiphoton excitation and Zener interband tunneling. For an estimation of these two asymptotic behaviors Keldysh defined the parameter γ as the ratio between photon frequency ω and tunnel frequency ω_t [135]:

$$\gamma = \frac{\omega\sqrt{2mE_{gap}}}{eE} = \frac{\omega}{\omega_t}. \tag{1.19}$$

For low optical frequencies and strong optical fields and thus $\gamma \ll 1$, the time for electrons passing through the tunneling barrier is sufficient. The picture of quasi-static tunneling is valid. The second asymptotic behavior, when $\gamma \gg 1$ corresponds to high frequencies, where electrons do not have the time to traverse the tunneling barrier, the multiphoton description is employed. In our experimental approach, the Keldysh-parameter for an electric field strength on the order of 10^{10} V/m is in the intermediate regime of $\gamma \approx 1$.

Fowler-Nordheim tunneling at metal-silicon dioxide interfaces

An explanation for electron emission from metals in the presence of intense electric fields was given by Fowler and Nordheim [136] in 1928. The authors developed a description for the transmission of electrons inside a metal electrode tunneling through a potential barrier. If the effective tunneling barrier is strongly bent due to an external electric field, the transmission coefficient through the barrier is nonzero and an electric current is generated. In figure 1.16 b) Fowler-Nordheim tunneling is represented by the mechanism (3) in the metal-dielectric-metal nanojunction. The external electric field $E_{NIR}(t_0)$ of the optical pulse at a distinct point in time t_0 effects a bending of the conduction and valence bands in SiO_2. When the electric field is strong enough, Fermi level states of the metal electrode coincide energetically with empty levels of the unoccupied conduction band of the dielectric. Tunneling between these states can thus occur, causing an optically-induced current. The effective tunneling barrier width x as a function of the external electric field $E_{NIR}(t_0)$ can be calculated as $x = \frac{4.2eV}{eE_{NIR}(t_0)}$ [135]. The energy gap of 4.2 eV corresponds to the energy

difference of the electrons in the gold and the CB of the dielectric. A formula for the tunneling current density j of the current flux from the metal electrode to the SiO_2 is given by [137]:

$$j(E(t)) = \frac{e^3 \mathbf{E(t)^2}}{8\pi h \phi_m} \exp\left(-4 \cdot \frac{\sqrt{2m}\phi_m^{3/2}}{3\hbar |e\mathbf{E(t)}|}\right). \tag{1.20}$$

Here, m is the free-electron mass and ϕ_m is defined as the energy barrier height form the Fermi level of the metal to the conduction band of the SiO_2. To distinguish whether charge carriers are injected into the conduction band of SiO_2 by Fowler-Nordheim tunneling, current measurements as a function of the pulse intensity $I \propto |\mathbf{A(t)}|^2$ are required to see if the data fit to

$$j(t) \sim E(t)^2 \exp \frac{1}{E(t)}. \tag{1.21}$$

Figure 1.18 shows the simulated charge carrier injection rate for two pulses with a CE-phase of $\varphi_{CE} = 0$ and $\varphi_{CE} = \pi/2$. Qualitatively this injection rate over time resembles the one calculate with the Zener tunneling.

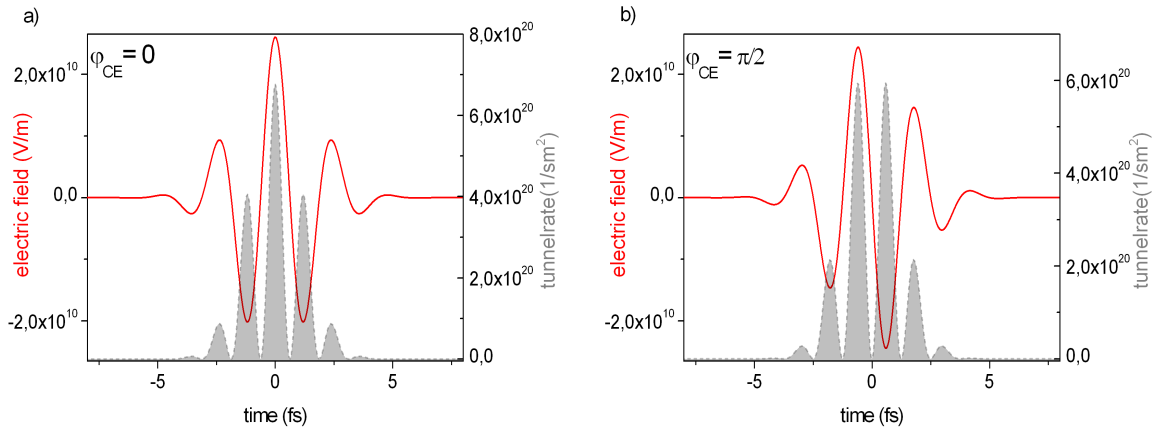

Figure 1.18: Charge carrier injection rate calculated for Nordheim-Fowler-tunneling for two values of φ_{CE}: a) The CEP of the a near single-cycle NIR pulse is set to $\varphi_{CE} = 0$. b) $\varphi_{CE} = \pi/2$: The charge carrier injection rate strongly depends on the CE-phase, which is similar to the calculations performed with the Zener-interband tunneling. The maximum electric field strength for both simulations is $2.6 \cdot 10^{10}$ V/m.

1.8.4 Mathematical description of optically injected electric current

We assume an electron located in the conduction band of a dielectric sandwiched between two metal electrodes as introduced in figure 1.16 which will subsequently be exposed to

an ultrashort, near-single cycle pulse. The electron will be accelerated by the oscillating laser field. After the presence of the pulse the net momentum p of the electron sums up to zero, due to the propagation of the pulse according to *Maxwell's equations*. Only if charge carriers are created during the presence of the laser field a net momentum can accumulate. In classical mechanics the net momentum for a charge carrier generated at a time t_0 can be calculated as [122]:

$$p = -e\int_{t_0}^{\infty} E(t)dt = -e\int_{t_0}^{\infty} \frac{\partial A(t)}{\partial t}dt = -e\left[A(\infty) - A(t_0)\right] = eA(t_0) \tag{1.22}$$

, where *A(t)* is the vector potential of the few-cycle electric field. For the theoretical calculation of the net current density of excited charge carriers within the presence of the electric field $E(t)$ of ultrashort laser pulses, we can split this process into an generation/excitation process $\Gamma_{injection}$ and into a drive process, where the electric field pushes electrons towards the electrodes. The carrier injection rate $\Gamma_{injection}(t')$ then corresponds to the number of charge carriers injected per time unit into the CB of the dielectric at the time *t'*. $\Gamma_{injection}(t')$ implements the nonlinear injection mechanism in dependence of the electric field amplitude and the CEP. The drive process is described by the momentum $p(t, t')$ which accumulates from the time *t'* of excitation until time t. m_{cb} is the effective mass of injected electrons in the CB. For the charge carrier current density we get:

$$j(t) = -e\int_{-\infty}^{t} \Gamma_{injection}(t')\frac{p(t', t)}{m_{cb}}dt' \tag{1.23}$$

In our picture (see figure 1.19 a)) we assume that charge carriers are injected to the conduction band (1) and instantaneously feel the momentum of the laser electric field (2). The macroscopically detectable net current charge Q_{pulse} arriving at the electrodes is given by:

$$Q_{pulse} = \int_{-\infty}^{\infty} j(t)\ A\ dt, \tag{1.24}$$

where A is the area of both dielectric-metal interfaces. Here, ballistic electron transport is assumed. Inside the dielectric SiO_2 the scattering time for electron energies up to 3 eV corresponds to a mean free path on the order of nanometers [127]. For the dielectric nanojunction with a gapsize of 50 nm this simplification is justified. Until now one pulse for the injection and drive of charge carriers was considered. Experimentally in section 3.3.5 the injection and drive process are decoupled by exposing the junction to two synchronized orthogonally-polarized pulses (see figure 1.19 b)), such that one triggers the charge carrier generation and the other accelerates them. In the latter case, the delay between injection and drive can be varied, thus time-resolved information is accessible. This kind of polarization gating, will help to differentiate possible injection mechanisms. Additional parameters

as the time delay $\Delta\tau$, the CEP of the injection pulse as well as the CEP of the drive pulse can be varied to get insight into the time-resolved charge carrier motion in the solid state.

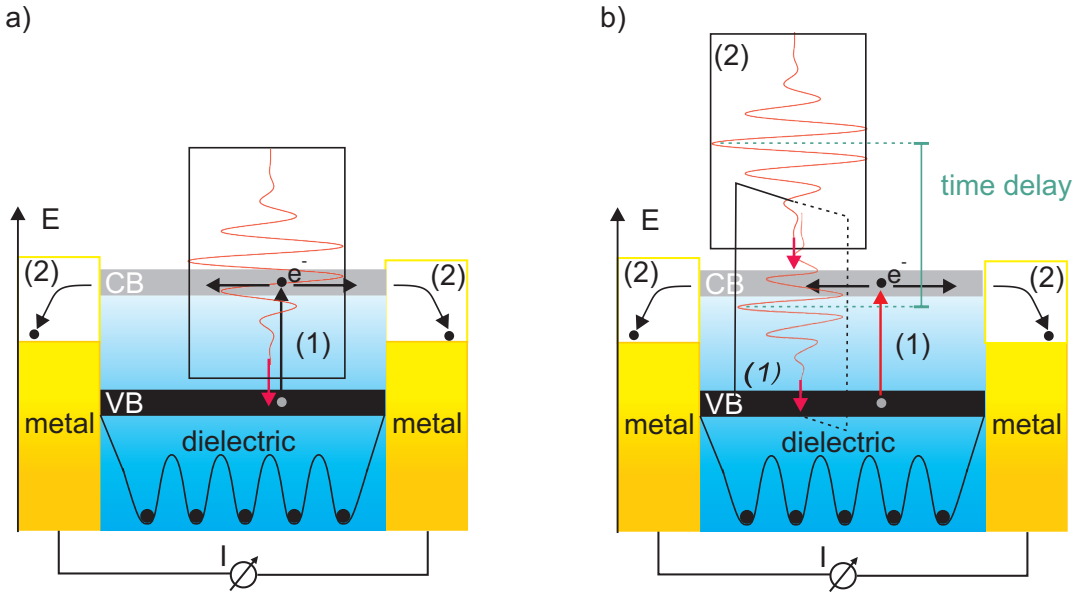

Figure 1.19: Two sketches visualizing the description of charge carrier injection into the dielectric. a) Principles of the one pulse experiment, where charge carriers are injected to the CB (1) and driven towards the metal electrodes (2). b) The decoupling of charge carrier injection (1) and the control (2), by two pulses polarized perpendicular and delayed in time.

2 Experimental methods

In the beginning of this chapter, the so called "tetrahedral SNOM-tip" is introduced, since it is employed as a tool in two types of experiments presented in this thesis. In the second part of this chapter a novel approach to characterize the electronic properties of single molecules as well as their optical properties is explained. The experimental configuration is described in detail, also the sample preparation, the characterization and the experimental procedure are exemplified. In the third part the experimental set-up to investigate the collective charge carrier motion inside a metal-dielectric-metal nanojunction optically excited and controlled by femtosecond laser pulse experiments as well as the experimental procedure is elucidated.

2.1 The tetrahedral SNOM-tip

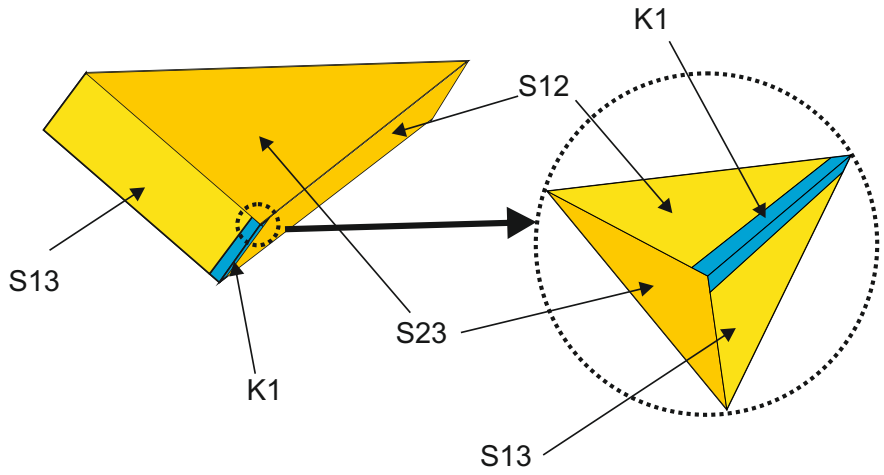

Figure 2.1: Sketch of the tetrahedral SNOM-tip. The body of the tip is cleaved out of glass and subsequently coated with a thin metal film. Depending on the evaporation process the edge K1 can be fabricated with or without metal, thus forming a nanogap over the entire edge. Figure adopted from [138].

The SNOM-tip (see figure 2.1) introduced here is also called T-tip due to its tetrahedral geometry. It is a scattering type or apertureless SNOM-tip and has been introduced by Fischer in 1993 [139] for the first time. The tip consists of a dielectric glass body, covered with a thin (20-50 nm) gold film on the planes. Depending on the fabrication process T-

tips with or without a nano-gap at the edge K1 (see figure 2.2) can be fabricated. Here its optical, respectively plasmonic properties are discussed, whereas the tip fabrication process is described in section 2.2.1.

Properties of the tetrahedral SNOM-tip

The basic idea of the T-tip is to create a light source that is intrinsically smaller than the diffraction limited focusing of far-field optics. It has been demonstrated by Bortchagovsky et al. [140, 141] that the tetrahedral-tip has the ability to act as a light source for SNOM [139] and as an alternative probe for Raman scattering. At the same time the T-tip can be used as a very efficient light collector [138]. SNOM-experiments performed by Koglin et al. demonstrated a lateral optical resolution below 10 nm [142]. This high resolution indicates that the light originates from an extremely localized excitation at the apex of the tip [143]. A brief overview about the different theoretical approaches to describe the light confinement and the enhancement at the apex of the T-tip is given here.

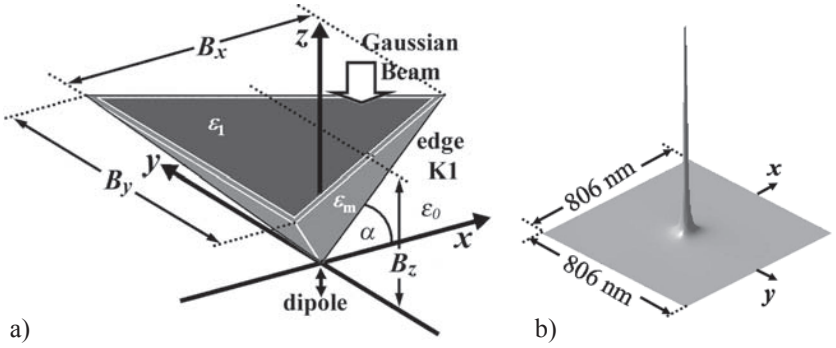

Figure 2.2: Geometry of the tetrahedral tip and light confinement at the apex: a) Sketch showing the geometry of the tetrahedral tip, it consists of a glass body that is covered with gold at three faces. The size of the tip in the simulation was $B_x = 6,2\ \mu m$, $B_y = 5,5\ \mu m$, $B_z = 3,1\ \mu m$. ε_m and ε_1 are the dielectric constants of gold respectively glass. The angle of the x-axis with respect to the edge K1 is 45°, while the white arrow displays the direction and the position of the incident Gaussian beam. In close vicinity of the point zero of the coordinate system a light emitting dipole source is placed. b) By means of the finite-difference time-domain (FDTD) method the optical intensity distribution at 5 nm below the apex in the xy-plane is simulated. The peak values of the intensity is normalized by the incident intensity with a value of approx. 15. Figures adopted from [144].

Tanaka et al. [144] performed simulations with the finite-difference time-domain (FDTD) method for a T-tip geometry without gap at the edge K1. This method is well established

for the simulation of *Maxwell's equations* in nanoplasmonics. [144, 145]. In their calculations they first demonstrated the electric-field evolution of a non illuminated T-tip where a dipole excitation source is placed close to the apex (see figure 2.2 a)). The results show that localized light emission in the near-field couples into the interior of the SNOM-tip, where it can be detected in the far-field. In a second step a Gaussian beam with 633 nm wavelength was coupled from the backside into the tip (see figure 2.2 a)). The simulations demonstrate that the tip can act as an extremely localized light source which is much smaller than the conventional diffraction limit (see section 1.6). The light intensity at the position of 5 nm below the apex in the xy-planes is increased by a factor of 15 with respect to the intensity of the incident Gaussian beam in this simulation (see figure 2.2 b)). The authors describe this superfocusing effect by a dimensional reduction of SPP modes in a 1-D metal-insulator-metal sandwich structure. The so called plasmonic edge modes at the air metal interface can be excited by momentum matching of the incident light with the SPPs. Thus energy is transported by the edge modes to the apex, resulting in an increase of intensity. One has to point out that the numerical simulations are based on a quasi-static model, meaning that for each time step the electric field is assumed to be constant. The simulations do not take into account retardation effects like the temporal evolution of dipole radiation. The light confinement strongly depends on the position where the incident beam is set. The numerical results reveal in most of the cases an attenuated field distribution at the apex. Moreover the influence of the substrate at the vicinity of the tip is not considered. To conclude, the simulations propose possible mechanisms of energy transport to the apex of the SNOM-tip without a gap at the edge K1. However a reliable prediction regarding the effective field distribution cannot be given.

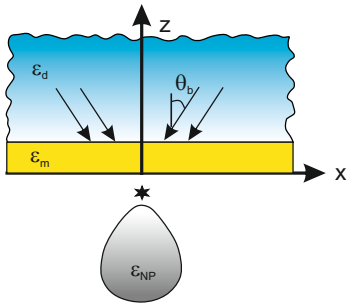

Figure 2.3: Model system for the simulation of light confinement and electromagnetic field enhancement performed by Geshev et al. [146]. Figure adopted from [146].

Figure 2.3 depicts another numerical approach which was presented by Geshev et al. [146]. The authors approximate a STM-tip as a metallic nanoparticle with varying radius R_C ranging from 1-100 nm and a dielectric function ε_{NP}. Between the metal film with a per-

mitivity of ε_m and the nanoparticle a radiating dipole along the z-axis is set. A polarized Bessel laser beam is used to excite SPPs in both the metal film and the nanoparticle. The totally reflected incident light beam forms a strong localized evanescent near-field below the metal film [146]. *Maxwell's equations* are solved for this axially symmetric scattering problem [146]. The advantage of this approach is the full representation of the electromagnetic field inside as well as outside the nanoparticle by a Green's formalism [146]. The results reveal that the electromagnetic field strength is strongly dependent on a variety of parameters as the shape, size and permittivity of the nanoparticle as well as the incident wavelength, the angle of incidence, the metal film thickness and most importantly the gap distance. The field enhancement calculated for a silver sphere acting as nanoparticle tip at a gap distance of 1 nm and a radius curvature of approx. 1 nm is on the order of 1000 for illumination of the metal film at an attenuated total reflection (ATR) configuration. ATR is a specific technique derived from the total internal reflection set-up (see section 1.6) and often applied in infrared-spectroscopy [147]. These simulations are a good basis to estimate the field enhancement at the apex of the t-tip, even if the exact geometry is not taken into account.

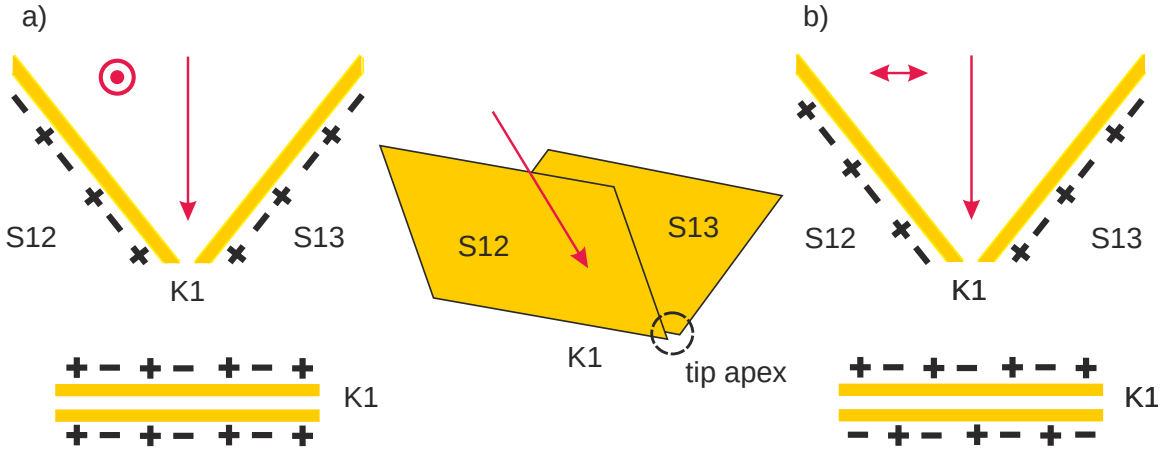

Figure 2.4: Sketch of the charge distribution at the air-metal interface for two different light polarizations at a given time: a) The upper image shows the charge distribution along the edges S13 and S12 for an oblique incident beam that is polarized along the edge K1. The draft below is the resulting symmetric charge distribution at the gap region of K1. b) An asymmetric charge distribution is obtained when the oblique incident light beam is polarized perpendicular to the edge K1. Figure adapted from [143].

When realizing a metalized T-tip with a gap (figure 2.1) at the edge of K1, Fischer et al. [143] proposed an additional pathway for SPPs to propagate. The authors suggested

that the gap may act as a plasmonic waveguide. One end of the gap is illuminated in an oblique manner. It is expected that SPPs are excited, which then propagate towards the apex, forming a strongly enhanced localized optical field. The charge distribution of the plasmons depends on the polarization of the incident light beam with respect to the gap. For an incident light beam that is polarized along the gap at the edge K1 (see figure 2.4 a), a symmetric charge distribution is expected, whereas an antisymmetric distribution for perpendicular polarization with respect to the gap is presumed (see figure 2.4 b). In thin metal films on glass it is generally not possible to excite SPPs within the glass-metal interface with a total internal reflection configuration due to the fact that there is a momentum mismatch of the incident light beam (see section 1.5) [143]. The authors claim that the situation is different when considering a layered system where a dielectric is sandwiched between two metal films. A symmetric charge distribution in figure 2.4 a) results in an increased plasma frequency due to Coulomb interaction for a sufficiently small glass gap. An antisymmetric charge distribution visualized in figure 2.4 b) would then lead to a decreased plasma frequency due to charge attraction. Fischer et al. calculated that a symmetric charge distribution at the edge K1 enables the coupling of light to SPPs at the metal-glass interface, which can propagate towards the apex, where a strong localized electric field might be generated. The coupling is explained by the vanquishing of the momentum mismatch due to the increased plasma frequency which generates an intersection of the dispersion relation (analogous to figure 1.6). An advantage of this SPP interface excitation is the higher efficiency compared to the case where SPPs are directly excited and the k-mismatch has to be compensated by the roughness of the surface [143]. To prove their hypothesis, dispersion relations for the metal-glass-metal system for gap sizes ranging from 500-25 nm were calculated. If the gap is small enough Fischer et al. concluded that external SPP modes from the metal-air interface might couple to internal SPP modes that then form a localized excitation at the apex of the tip. The model introduced here is very simplistic and does not describe the local field distribution at the apex, but it gives a hint for a possible efficient energy transfer by SPPs to the apex.

None of the three model-systems introduced in this chapter gives detailed information about the three dimensional field distribution and the resulting field enhancement at the apex of the tetrahedral tip. The calculations introduced here provide indications for possible mechanism explaining the light confinement at the apex. For a deeper understanding time-consuming three-dimensional simulations should be conducted which take the radiative decay of SPPs at the apex as well as on the metal substrate and retardation effects into account. For bare metal tips the local field distributions at the end of the tip is quite well understood [82, 85].

A benefit of the illuminated tetrahedral tip in optical spectroscopy on the molecular level

compared to far-field illumination of bare metal tips is the fact that only the sample volume is illuminated directly with a very high intensity. Therefore the tetrahedral tip has a reduced background radiation as well as reduced photobleaching of the entire sample [141]. Different detection pathways of the tip in optical spectroscopy are presented in the following.
As a SNOM-probe the tetrahedral tip provides access for signal detection from the metal substrate surface to the optical far field. Bortchagovsky et al. [140] specified signal detection channels for different experimental configurations with the T-tip depicted in figure 2.5. Radiation emitted from a dipole source (e. g. Raman signal of a molecule) close to the metal substrate can be detected through channel 1, where the signal is transmitted through the metal film below the critical angle of total reflection α_c, recordable with an objective of an NA < 1. The arrows of channel 2 show a leaky SP mode, that propagates along the gold-air interface of the substrate. It is named as leaky mode because it can dissipate its energy by radiation into the glass, where it has an angle slightly above α_c, detectable with immersion oil objectives having an NA >1. The highest efficiency for the detection from this channel is found for a substrate thickness of 50 nm [140]. The very efficient detection channel 3 is utilized in an external reflection configuration, where the optical signal is emitted into air. Non-radiative SP modes are the channels 4 and 7, which propagate along the glass-metal interface in the substrate respectively the tip. Both channels are not available for the detection in the optical far field. Direct radiation into the tip is achieved with channel 5. This way the tip can act as excitation source and detector at the same time. Another leaky SP modes forms channel 6 along the metal-air interface of the tip which is analogous to channel 2. A leaky edge mode, that propagates along the edge of K1 acts as the signal channel 8, designated in figure 2.5 with 2 arrows. This channel is suggested by the authors to serve as an efficient signal mediator for Raman spectroscopy on the molecular level. Significant efforts have been made within the last 15 years to understand the optical and plasmonic properties of the tetrahedral SNOM-tip. It still remains challenging to calculate the field distribution at the apex in a more precise manner. The effective field distribution depends on a number of parameters as the local geometry at the apex, the gap-size, the gold film thickness, curvature of the apex, the light intensity and the angle of cleavage, which are unique for each fabricated tip.

2.2 Experimental set-up for light illuminated single molecule junctions

Figure 2.6 shows a sketch of the principal realization for a single molecule transport experiment. The idea behind it is very simple. Two metallic electrodes with a precisely adjustable gap size are approached, while a voltage between the electrodes is applied. A monolayer

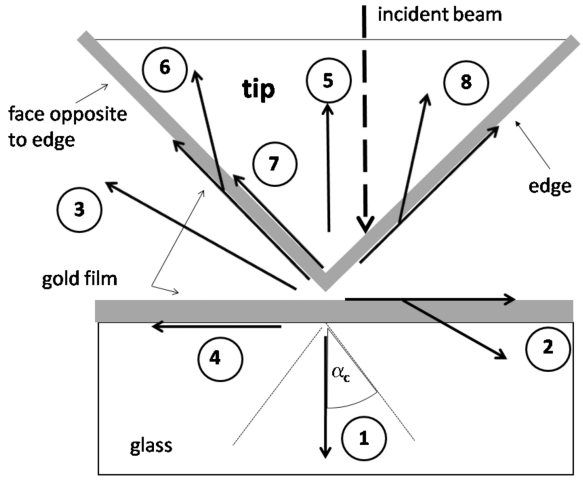

Figure 2.5: Plasmon modes along the tetrahedral SNOM-tip. The tip is illuminated from the inside (see dashed arrow) exciting different plasmon modes. For signal detection radiative channels are required, these are the channels 1,3,5, which are detectable in the far field. The leaky modes are (branched arrows 2,6,8) also efficient detection channels for tip enhanced Raman spectroscopy, in contrast to the non radiative modes (4,7) which are dissipative and not accessible in the optical far field. Figure adopted from [140].

of molecules is bound to one of the electrodes. The approach is stopped when the first molecule touches the second electrode. As soon as the molecule has locked between both electrodes the electric current driven through a single molecule can be measured. In figure 2.6 a metallic substrate acts as the first electrode. The second electrode, the so called counter electrode, is the metal coated glass SNOM-tip (see section 1.6, 1.5 and 2.1) with an atomically sharp corner. The advantage of this experimental single molecule transport realization is the simultaneous utilization of the SNOM-tip as a counter electrode and as a localized light source. By focusing light into the inside of this apertureless SNOM-tip, it acts as plasmonic waveguide to focus surface plasmon polaritons to the apex of the tip, where a strongly enhanced evanescent field is confined to only a few nanometers (see section 1.5 and 2.1). One can then explore the backscattered light coming from the SNOM-tip with a spectrograph. In the following the SNOM-tip, the sample preparation and the home-made experimental set-up are described in detail.

2.2.1 Tip fabrication

The great advantage of the this apertureless SNOM-tip is the rather simple and fast fabrication process, which is similar to the cleavage of glass knives in ultramicrotomy [143]. The SNOM-tip consists of a tetrahedral dielectric glass body and a metallic cover layer. Three sides including the apex of the tip are covered with a thin metal film. For the fabrication

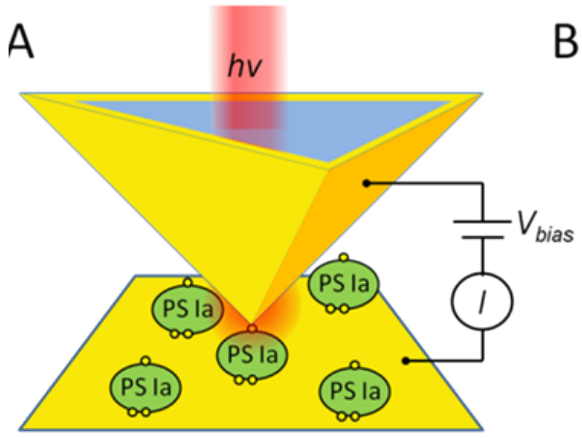

Figure 2.6: Sketch of the experimental configuration: A metallic substrate covered with molecules and a metal-coated SNOM-tip on top. With precise control of the gap distance between tip and substrate it is possible to perform conductance measurements on single molecules in a strong optical field and analyze the backscattered light at the same time.

of the T-tips microscope glass cover slips from the company *Thermoscientific/ESCO* with a size of 22×22 mm^2 and a thickness of ≈ 0.25 mm are utilized. High-purity a-SiO_2 plates from the supplier *Crystec* are employed for the experimental approach described in section 2.3. To remove any organic contamination on the T-tips, every cover slip is traversing a special cleaning process. Thereby the glass cover slip is fixed on top of a heating plate, that is heated up to $40 - 50°C$. In the next step bottled CO_2 gas is led through a so called snow jet pistol (*Applied Surface Technologies*) that creates small dry CO_2 ice particles in a high velocity gas stream [148–151]. The dry CO_2 ice removes hydrocarbon-based contaminations as well as small particles on the glass cover slide [148–151]. Due to the heat of the heating plate, no water condensates on top of the glass slide, which is considerably cooled down during the exposure to the snow jet. After the cleaning, the cleavage process is performed manually. Figure 2.7 shows a sketch of the cleavage process. The cleaned glass cover slip is slightly scratched with a diamond cutter at two edges that include an angle of about 90°. This angle can be varied to adjust the sharpness of the tip. This way, a glass prism of $3 - 5$ mm side length, with a atomically sharp apex, is formed [152, 153]. The tips are subsequently fixed on a sample holder in an evaporation chamber (*Leybold*) at a pressure of 10^{-5} mbar and covered with a metal coating at room temperature. The effective thickness is around $20 - 25$ nm and monitored by an oscillating quartz crystal inside the evaporation chamber. At this juncture the thickness of the metal coating on the edges and on the planes depends strongly on the angle of the incoming metal beam with respect to

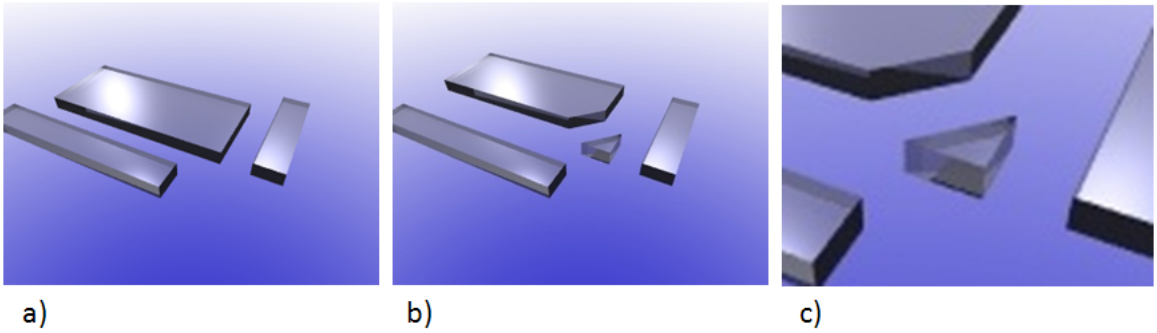

Figure 2.7: Sketch of tip fabrication procedure described in section 2.2.1.

the surface of the sides of the glass fragment. Gold is used on the one hand because of its chemical inertness, on the other hand because the molecules used in the experiments bind covalently to gold. To realize SNOM-tips without gold at the edge K1 and the plane S23, the two cleaved planes S12 respectively S13 (see figure 2.1) are coated with gold in a two step shadow evaporation process. The non-metalized gap width of 20-200 nm is adjustable by the angle of incidence of the evaporation source with respect to the plane that gets coated. Subsequently the Ohmic resistance across the two evaporated planes is measured. In case of metallic contact, the gaps have local shortcuts along the edge. This shortcuts can be removed by applying a DC-voltage, that is carefully increased up to 5 V. Because of the high electric fields across the edge and a current flow in the order of mA the shortcuts are removed by a combination of electromigration and melting [40]. Thus nanogaps in the order of few tens of nanometers are formed. Figure 2.8 shows SEM images of both T-tips with and without gap.

2.2.2 Sample preparation

Substrate

A rectangular shaped glass slide (10×5 mm^2) is cleaved out of a glass cover slip. The cleaning and fabrication process is the same as described in the former chapter 2.2.1. The typical thickness of the metal film is 50-100 nm, with gold as metal coating. By varying the evaporation rate of the gold during the evaporation process the roughness of the film can be increased which can be beneficial for the strength of the local optical field at the surface of the substrate (surface enhancement) as discussed in section 1.5. These gold coated glass slides act as substrates during the experiments, on which proteins and organic molecules are covalently bound.

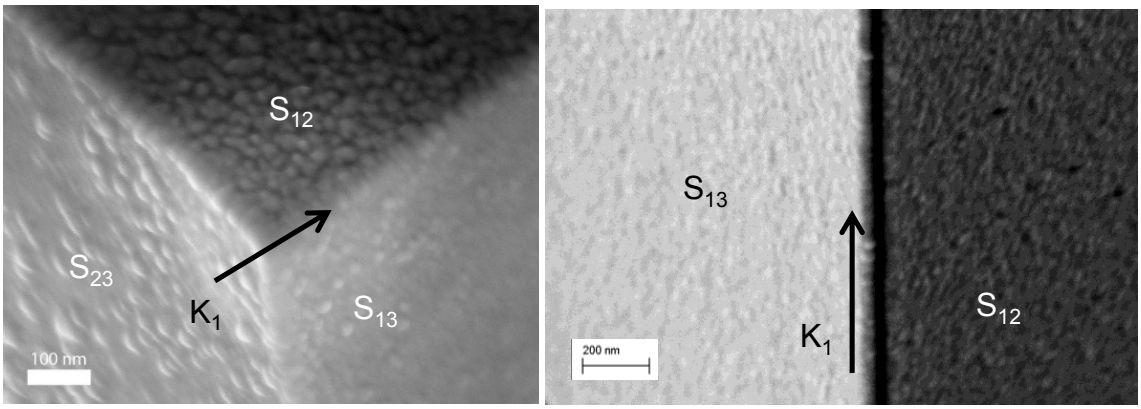

Figure 2.8: Scanning electron microscope image of the gold coated glass tips. Left: Three planes of the tip are covered with a thin gold layer of approx. 20 nm thickness. Right: SNOM-tip with an open edge: Nanogaps with a width of 20-200 nm can be realized by a shadow evaporation process, used in the experiments described in section 2.3.

Immobilization of PS I mutation

In section 1.7 the protein complex photosystem I (PS I) was introduced and in section 1.7.3 the properties of PS I and cysteine mutated species are discussed. Here, the wet-chemical preparation of mutated PS I covalently linked to a gold substrate is described. The pre-arrangement starts with the mixing of 0.3 ml phosphate buffered saline (PBS), a buffer solution for constant ph-value of 7.4, with PSI. To activate the sulfur of the cysteine groups, the PSI with a typical concentration of 0,8 chlorophyll/mol reacts with a 50 mmolar dithiothreitol (DTT) solution for 10-20 minutes in a shaker with 960 rpm at 25 °C. During this reaction disulfide bonds between cysteines are broken. Freestanding thiolgroups are then able to react with gold (see section 1.7.5). Subsequently the activated PSI is washed with Sephadex pillars (*PD spintrap G25* from *GE healthcare*) to remove excrescent DTT. The activated PS I solution is filled in an Eppendorf reaction tube, together with a gold substrate (section 2.2.2). The Eppendorf reaction tube is shaked thereafter for 12/24 hours, where thiolgroups of the PSI form a covalent bond when touching the gold surface. The following day the sample is rinsed with pure water and finally dried with nitrogen. Thereafter the sample is stored in an exsiccator in the dark and under vacuum conditions to prevent decomposition of PS I. This PS I surface immobilization was realized by Simone M. Kaniber [102].

Tour wires

Another species of molecules used in this work are so called Tour wires [154]. Tour invented the building block concept for the synthesis of rigid-rod conjugated oligomers, forming self-assembled mono and multilayers with different thiol-groups on gold [154]. Figure 2.9 depicts the molecule prepared for the experimental study here. The molecule [9,10-Bis(2'-para-mercaptophenyl)-ethinyl-anthracene] is also belonging to the group of Tour wires. At

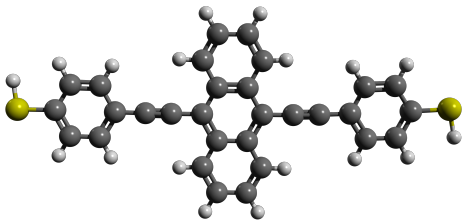

Figure 2.9: Sketch of the spatially symmetric molecule [9,10-Bis(2'-para-mercaptophenyl)-ethinyl-anthracene] without the acetyl-protection groups.

first a droplet of about 0.5 ml of a 1 mmol tetrahydrofurane (THF) molecule solution is put carefully with a Pasteur pipette on a gold-coated glass substrate (see section 2.2.2). The substrate is fixed on a kimwipe/kerchief to absorb overflowing molecule solution [50]. The rod-shaped molecules used in these experiments were terminated with acetyl-protected thiol groups. During the exposure time of 10-20 minutes acetyl protection groups split off, when the molecules in solution touch the gold surface. This way, the sulfur of the thiol-group is bound covalently to the gold of the substrate. A monolayer of molecules on the gold surface is formed with this technique, whereby the molecules are bound covalently to the gold on one side. On the far side of the gold surface the upstanding molecules remain acetyl-protected. When the solvent has dried, the substrate gets rinsed several times with pure THF to ensure that all molecules that did not bind covalently to the gold are removed. The exact density of molecules on the surface is not known. Due to the exposure time of 10-20 minutes, it is assumed that the molecule density is close to a monolayer [155, 156].

2.2.3 The experimental configuration

Figure 2.10 shows the set-up for single molecule experiments with the aforementioned SNOM-tip acting as a counter electrode and local light source at the same time. A gold-substrate with immobilized molecules is fixed on a high precision piezo crystal and a sample holder with the SNOM-tip placed above the substrate. Both components are situated inside a UHV chamber. A sourcemeter serves as DC voltage source and measures the current. Two different light sources are employed during the experiments - a Xe arc white light source and a He-Ne-laser. Thereby the light is guided through several objectives and filters and

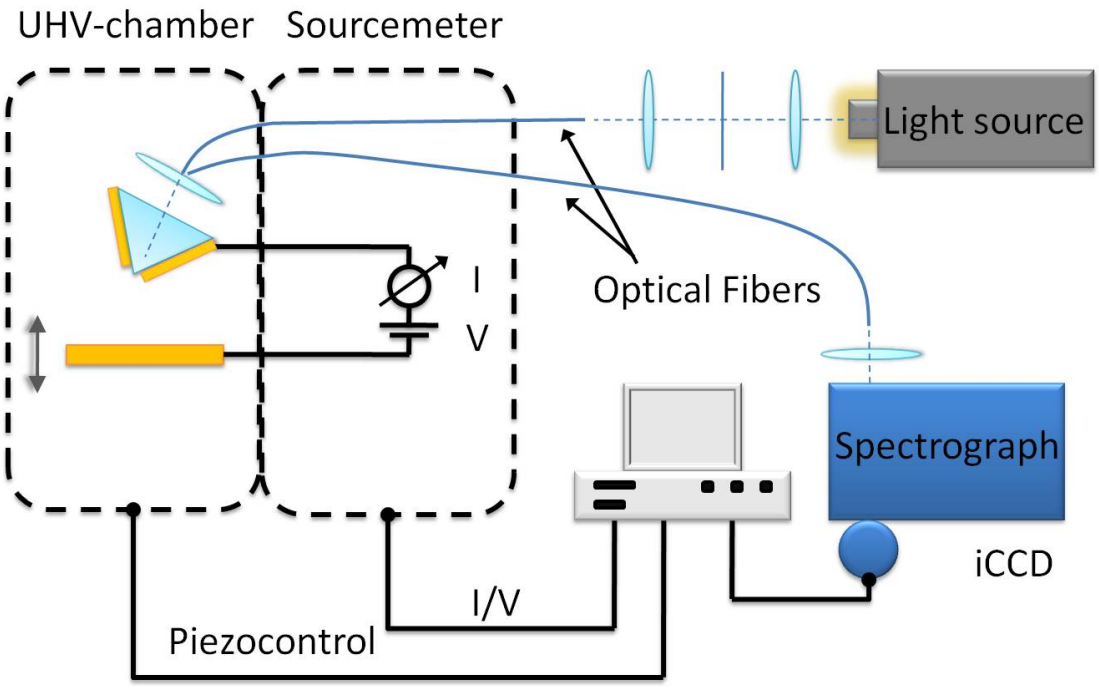

Figure 2.10: Set-up for single molecule transport measurements with a tetrahedral SNOM-tip. The SNOM-tip acts as a counter electrode and a light source at the same time. Light is coupled into the T-tip by an optical multimode fiber. The backscattered light is collected by a second optical fiber which is guided to the spectrograph, where the light is spectrally analyzed. The metal substrate is fixed on top of a low temperature high precision piezo actuator. To accurately control the distance between tip and substrate, the piezo is feed-backed on a given tunneling current. Inside a UHV chamber current-voltage characteristics are recorded by a sourcemeter. Vacuum conditions are established, to avoid adsorbent layers and oxygenation of molecules in high optical fields.

subsequently focused into a multimode glass fiber. Finally the fiber is fed through into the UHV chamber. There, a grated index (GRIN) lens at the end of the fiber focuses the light from the backside through the glass of the SNOM-tip into the apex. A second multimode fiber collects the backscattered light from the apex area of the SNOM-tip and transfers it through a suitable notch or Raman edge filter to a spectrograph. The whole set-up is computer controlled. In the following the single components of the set-up are explicated.

Cryostat/UHV-chamber

The experiments are performed under vacuum conditions at room temperature in a UHV chamber to avoid any adsorbent layers on the substrate or oxygenation of molecules in the high optical fields. Thus, a turbo molecular pump system (*TPU 060 from Balzers/Pfeiffer*) and a vane rotary pump (*Edwards*) are attached to the chamber, generating a base pressure below 10^{-7} mbar. In order to contact single molecules and to drive current through these molecules, mechanical stability is essential. Therefore the whole set-up (figure 2.10) is mounted on vibration absorbers. With a commercially available ^{4}He flow cryostat (Cryovac), low temperature measurements down to 30 K are realizable. The sample holder is mounted on top of the cryostat inside the UHV chamber as depicted in figure 2.11. Two fed-throughs, one for optical fibers a second for electrical connections are fixed at the outer face.

Piezo control

A low temperature high precision piezo crystal (*Physik Instrumente(PI)*) is used to position the sample with respect to the tip. The substrate is fixed on an electrically isolating layer. Since the SNOM-tip and the substrate are metal-coated the distance can be controlled by a STM feedback technique which is based on the tunneling effect. The tunneling current I_{tunnel} through a rectangular barrier for voltages lower than the work function of the gold electrodes is described in a good approximation as [157]:

$$I_{tunnel} = C \cdot V e^{-2x\sqrt{\frac{2m\varphi}{\hbar^2}}}. \tag{2.1}$$

Here, C is a constant depending the tunneling area and the electron density of states, while V corresponds to the applied voltage. m is the electron mass, x the barrier width and φ describes the barrier height, while $\hbar$ is the Planck's constant. The difference to a common STM set-up is the lack of piezos for the lateral control along the surface (x- and y-axis). Only a piezo for the distance control in the vertical direction is provided (detailed description in chapter 3.1). The reason for this realization is to minimize drift effects which would make it impossible to have molecules covalently bound between two electrodes. In

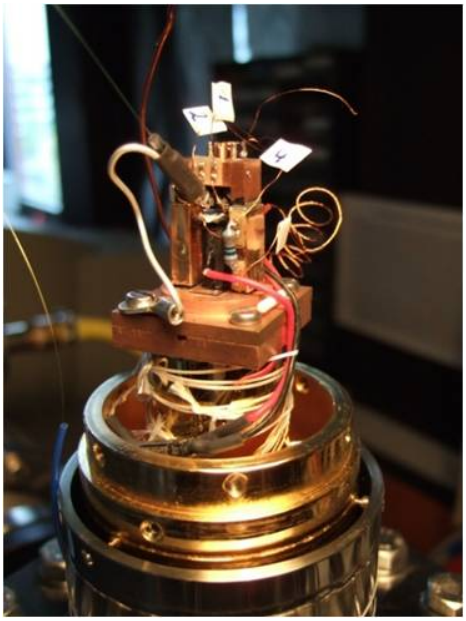

Figure 2.11: Image of the home-made set-up mounted on top of the flow cryostat. The sample holder is positioned on top. The red cable connects the piezo with the high-voltage output. At the end of the fiber a GRINS-lens is fixed, focusing into the back of the SNOM-tip.

common scanning probe techniques as STM, SNOM and AFM, it is difficult to keep a tip over a molecule at a fixed position above the surface in the time window of tens of seconds, due to thermal drifts even with compensation techniques. With a single piezo crystal one looses the ability to scan over the surface, but one gains the mechanical stability that enables single molecule transport measurements in the time range of several tens of seconds. The operating voltage of the piezo ranges from 0 to -1000 V, realized with a home built high voltage amplifier with a voltage resolution of 3 mV that corresponds to a step size of about 0.18 Å.

Sample holder

The sample holder (visualized in figure 2.12) is made of copper on which the SNOM-tip is glued with a colloidal silver liquid (Pelco®). It consists of two side plates, a central plate in the middle that connects the main holder with a fine thread and two rods. The fine thread is composed of two ends with different screw threads, thus the difference between the threading defines the height change. The fine thread is required to approach the SNOM-tip to a substrate distance smaller than 10 μm, the working range of the piezo crystal. The pitch of the thread is 150 μm for one rotation of 360°, that corresponds to a height difference of 2.1 μm, when the fine thread is turned 5° by a screwdriver. The side plates

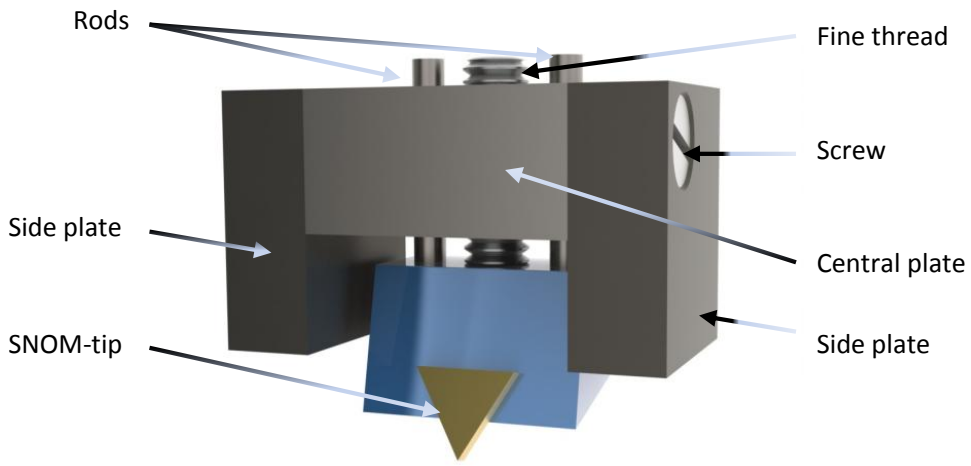

Figure 2.12: Sketch of the sample holder. In the center a gold coated SNOM-tip is fixed on an insulator. On top a fine thread that enables a smooth approach into the working distance of the piezo is situated.

and the central plate are interconnected with a screw enabling an independent adjustment of the components with respect to each other. As depicted in figure 2.12 the surface where the SNOM-tip is positioned is tilted, to ensure that only the apex of the SNOM-tip gets in touch with molecules and not the whole cleaved edge. This surface is covered with an insulating glass plate which is glued onto the metal with a particular UHV suitable gluten. The SNOM-tip is glued onto the glass plate in a way, that the apex sticks out about 1 mm. For the connection to macroscopic leads a cooper wire is fixed with silver collodial liquid to the SNOM-tip, that finally ends in the sourcemeter. In combination with a current control feedback loop a smooth and controlled approach into the working distance of the piezo is enabled.

Sourcemeter

A sourcemeter from *Agilent Technologies* (model E5263A) with a high speed medium power source measuring unit (MPSMU) acts as a DC high precision voltage source. The resolution of the voltage output up to ± 2 V is ± 0.1 mV. This sourcemeter is accessed via GPIB with a computer and has a current measuring accuracy of 5 pA up to a limit of 100 nA. The current detection limit for the given set-up is <1 pA. By applying a voltage between SNOM-tip and substrate current-voltage characteristics are measured and time-averaged in units of power line cycles (PLC). During a PLC 128 samples are measured and averaged for each voltage step. The minimum integration time is 100 μs and the maximum number of steps is 1001 per voltage sweep measurement. The typical acquisition time for current-voltage

characteristics is 10-30 s.

Light sources

Two different light sources are employed in the experiments. The first is the Xe-light source LAX 1530 (*Müller Elektronik-Optik*) with a switchable output power between 150 and 300 W, providing a broadband light spectrum from the ultraviolet (UV) at 250 nm up to the near infrared (1250 nm). The second light source is a stabilized He-Ne-laser HRP120 (*Thorlabs*) with a wavelength of 633 nm and an output power of 12 mW.

Spectrograph

The spectrograph from the company *Princeton Instruments* is composed of a spectrometer (ACTON SP2300i) and a detector system (SPEC-10). The spectrometer has two different gratings, a focal length of 0.300 m and an aperture ratio of f/3.9. The detector attached to the spectrometer is a liquid nitrogen cooled ($-120°$ C) imaging charge coupled device (CCD) camera with a maximum CCD resolution of 0.14 nm and a peak quantum efficiency >90 %.

Optical multimode fiber

One way to couple light into the back of a SNOM-tip that is fixed inside a UHV chamber is the application of an optical fiber. In our set-up two optical multimode fibers are employed. Light coupling into the SNOM-tip is accomplished with the first fiber. The second optical fiber collects light from the SNOM-tip and guides into the above mentioned spectrograph, where the light is spectroscopically analyzed. For either efficient light coupling or trapping a GRIN lens with a high NA of 0.46, an effective focal length of 1.94 mm and a transmittance of >89 % from 380 - 2000 nm wavelength, is glued at the end of one fiber into a ferrule sleeve. The fiber, fixed in a pigtailed ferrule, is plugged and adjusted into the working distance of the GRIN lens. An eight degree angled facet minimizes back reflection and compensates for the beam deviation resulting from the angled pigtail ferrule. The fiber end for the light coupling is fixed on an translation stage (*Thorlabs*), to adjust the light coupling. To decouple the collected light from the second fiber into the spectrograph this fiber end is positioned on a fiber stage (*Newport*) in front of the spectrograph.

Optical components

Along the light path different optical components are built in. In case of the Xe-light source, a pinhole and up to three neutral density (ND) filters with different attenuation factors and an objective with a numerical aperture of 0.1 are positioned in front of the above mentioned

multimode glassfiber. The reflected light that is expanded with the second fiber is collected with a second objective before it is focused into the spectrograph with a third objective. When the He-Ne-laser acts as light source, a laser line filter is positioned in front of the laser, and a Raman edge-filter (*LOT-Oriel*) that acts as a high pass filter, transmitting light with energies below the laser wavelength or a suitable notch filter (*LOT-Oriel*) that absorbs the wavelength 633 ± 8 nm are placed in front of the spectrograph.

Computer control

To control the piezo and the sourcemeter three programs are realized with *AgilentVEE* for the experiments. The first routine is a simple feedback loop program, which controls a target current at a specified voltage. The second procedure is utilized to study the "lock-in" behavior of single molecules, where the substrate is approached with a given step size up to a target tunneling current and subsequently retracted with the same stepsize. Depending on the type of bond between molecule and tip specific hysteresis during the retraction can be monitored (see figure 3.11). The third program is most often employed during the experiments. The main part of this program is the measurement of current-voltage-characteristics, while the piezo is manually controlled. The tunneling current is monitored on a software oszillograph in between the measurements of the IV-characteristics. For the spectrograph the program *WinSpec32* is employed. This program enables to record, to compare and to subtract spectra from the UV to the near infrared.

Light coupling into the apex of the SNOM-tip

The light coupling, with one optical fiber focusing into the apex (F1) and a second one for the collection of backscattered light from the apex of the tip (C2), was manually adjusted with the help of a microscope. The experimental approach to optimize the light coupling started with the fiber C2. At the far end of this fiber, inside the UHV-chamber, a GRIN lens was attached (see section 2.2.3). This end was mounted on a bendable wire. It was brought into the distance of the focal length of approx. 2 mm with respect to the apex of the SNOM-tip. The goal of this procedure was to couple the focused GRIN-lens laser spot, with a typical focal diameter of 50-150 μm, into the apex from the backside of the tip and excite surface-plasmon-polaritons (see sections 1.5 and 2.1). The angle of the incident laser beam with respect to the tip edge S23 (see figure 2.1) can be varied between 30-60°. The most critical step during this procedure was to ensure that the light spot seen through the microscope is effectively originating from the apex itself and not from reflections of the substrate, the sample holder, a side surface or an edge of the SNOM-tip. Only if the light spot was hitting the apex area from the backside an optical signal could be observed afterwards in the experiments. Figure 2.13 shows a sketch of the light coupling into the

SNOM-tip by means of the GRIN-lens. After finishing this procedure, this fiber C2 with

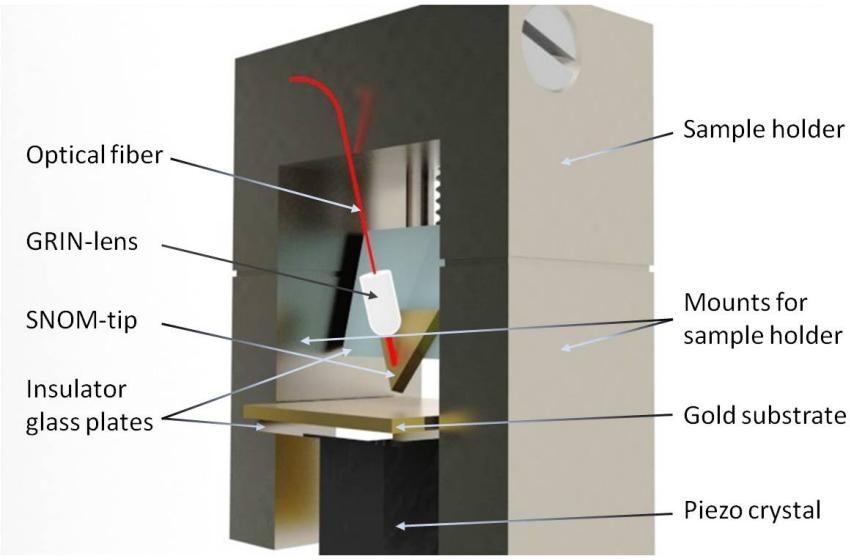

Figure 2.13: Sketch of efficient light coupling into the apex of the SNOM by means of a GRIN-lens.

the GRIN lens at the far end was unmounted from the translation stage and fixed onto a fiber stage. As the fiber C2 accomplishes the light collection from the apex of the tip it was fixed on the fiber stage to decouple the light from the fiber into the spectrograph. Subsequently the procedure described above was repeated with the fiber F1, used for light coupling into the SNOM-tip inside the UHV chamber.

2.3 Experimental set-up for solid state lightwave electronics

Figure 2.14 depicts the principles of the experimental configuration to study the mechanisms of charge carrier excitation and motion inside a metal-dielectric-metal nanojunction induced and steered by ultrashort laser pulses as a function of the carrier envelope phase. As a nanojunction the tetrahedral SNOM-tip with a gap-size of 20-200 nm over the entire edge K1 is employed (properties introduced in section 2.1). The gap region is thereby filled with amorphous or mono-crystalline SiO_2 sandwiched between the gold covered planes which act as electrodes. Additionally the whole tip is capped with a SiO_2 coating of 200-400 nm thickness with an e-beam evaporation technique. The SiO_2 coating ensures that the gap region is sensitive to optically excited electrons in the gold and the SiO_2 and not to the metal-air interface. The straightforward fabrication procedure is the reason for the usage of SNOM-tips as nanojunctions compared to the numerous processing steps in lithographic manufacturing of nanostructures. Steering of electrons by optical pulses in the condensed

carrier wavelength λ_L	720-750 nm
pulse duration τ_p	< 4 fs
power density I_0	$10^{13} - 10^{15}$ $\frac{\mathrm{W}}{\mathrm{cm}^2}$
max. electric field amplitude E_0	$10^9 - 10^{11}$ $\frac{\mathrm{V}}{\mathrm{m}}$
energy per pulse E_p	300-500 μJ
repetition rate of stabilized pulses f_{rep}	3 kHz
lock-in modulation frequency $f_{lock-in}$	1.5 kHz

Table 2.1: Basic properties of sub-5 femtosecond laser pulses employed in the experiments. The energy of one near-single cycle pulse is in the order of 400 μJ.

matter is interesting in fundamental research to understand the mechanisms of charge carrier excitation and control inside a dielectric. Figure 2.14 also sketches the experimental procedure. Near-single cycle sub-4 fs laser pulses are polarized either perpendicular (p-polarized) or parallel (s-polarized) with respect to the gap at the edge K1. The pulses are CE-phase stabilized (see section 2.3.2), while the absolute CE-phase and pulse length is adjustable by the insertion of two fused silica wedges (see section 2.3.3) into the beam path. The laser beam has a diameter of about 70 μm (for an intensity down to $1/e^2$) and is focused into the center of the gap region. The electric current is amplified by a variable high gain IV-converter (*Femto DLPCA 200*) and the CEP-dependent component is extracted with a lock-in amplifier at the CEP modulation frequency $f_{lock-in}$, which corresponds to half of the laser pulse repetition frequency $f_{rep} = 3$ kHz. These experiments were performed at the Max-Planck-Institute for Quantum Optics where a set-up for the generation of such sub 5-fs few-cycle CEP-stable near infrared (NIR) pulses is located [118,158]. The pulses are named NIR pulses, as the carrier wavelength λ_L is in the range of 720-750 nm. In table 2.1 the basic properties of the femtosecond laser pulses are displayed. The laser system as well as the CE-phase stabilization (see section 2.3.2) are described in the next subsections. Finally in section 2.3.4 the interferometric set-up is introduced, where the nanojunction is exposed to two laser pulses that are polarized perpendicular to each other. This set-up enables performing pump-probe experiments, with optical pulses that can be temporally delayed.

2.3.1 The femtosecond laser system

In figure 2.15 the set-up of the laser system for the generation of near single cycle VIS/NIR femtosecond pulses is visualized. In order to analyze phenomena arising from strong optical

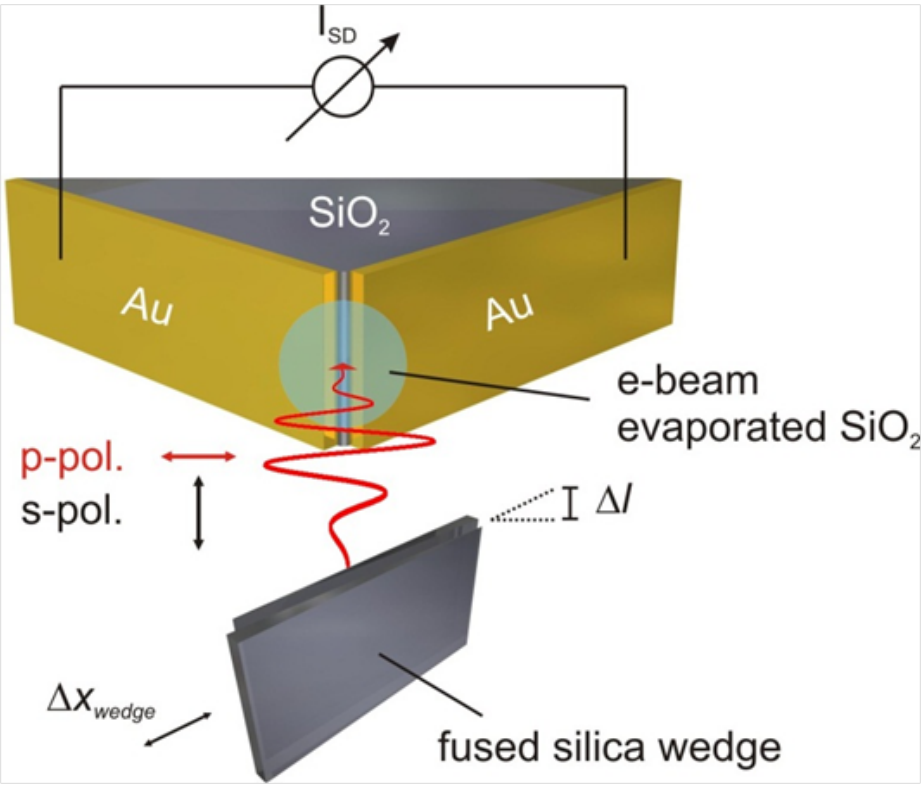

Figure 2.14: Sketch of the principal configuration for the study of charge carrier excitation and motion inside a metal-dielectric-nanojunction with CE-phase stabilized near-single cycle sub-4 fs laser pulses as a function of the CE-phase. The tetrahedral SNOM-tip acts as a nanojunction, while a pair of fused silica wedges enables to tune the CE-phase. The macroscopically detectable current is pre-amplified and recorded with a lock-in amplifier.

fields, oscillating fields due to their large bandwidth and hence their ultrashort time scale are required. Furthermore, it is possible to apply strong optical fields for a very short time and therefore avoid breakdown of the system. The Ti:Sapphire oscillator generates pulses with a pulse duration of 6-7 fs and a pulse energy of 5 nJ. This pulse energy is too weak for experimental usage and thus the seed pulses have to traverse a chirped-pulse amplification (CPA) process [159]. This pulse amplification process is limited by the damage threshold of the amplifying crystal and therefore the intensity of the pulse has to be reduced. This is achieved by stretching the pulse temporally down to a pulse duration of 15 picoseconds. Subsequently the pulses are amplified in the multipass amplifier. In the prism/chirped mirror compressor the pulses are recompressed to approx. 20 fs pulse duration and a bandwidth of 70 nm. A spectral broadening of the pulses is accomplished hereafter in the hollow core fused silica fiber, which is filled with Neon gas. The spectral broadening is necessary to enable a further pulse compression. In an additional chirped mirror compressor, the pulses are compressed to a near single cycle of approx. 4 fs and a pulse energy of 0.4 mJ at a carrier wavelength of 720-750 nm. In the following sections the different components of the laser will be described. A detailed description of all components can be found in the books of Chang [122], Diels [123] and the PhD-thesis of Rauschenberger [159].

Ti:Sapphire oscillator

The Ti:Sapphire oscillator (figure 2.15) is Kerr lens mode-locked and optically pumped by a frequency doubled continuous wave Nd:YVO_4 laser at 532 nm. The Kerr lens mode locking mediates the generation of 6-7 fs pulses with an energy of approx. 4 nJ at a frequency of 71 MHz due to self phase modulation (SPM) and self focusing (SF). At the output of the oscillator the pulses are focused into a periodically poled MgO-doped lithium niobate crystal (PPLN). Here, SPM and second harmonic generation (SHG) or alternatively difference frequency generation (DFG) is induced. As SHG or DFG are required for the phase stabilization (see section 2.3.2) the SHG, or respectively the DFG spectrum has to be separated from the fundamental spectrum. This is achieved by a dichroic mirror (DM) acting as a beam splitter. The reflected components are guided to a photodiode, where the signal is detected. The phase-locking electronics is feedbacked on the minimization of the f_{CEO} to stabilize the CE-phase. This CE-phase control technique is based upon a f-to-0 interferometer, also known as “fast loop” feedback (described in section 2.3.2). The fundamental spectrum is transmitted by the DM and directed to the stretcher.

Stretcher

Before entering the stretcher, the pulses are dispersed by a Faraday isolator (FI) to prevent any back reflections. The function of the successive third order dispersion chirped mirrors

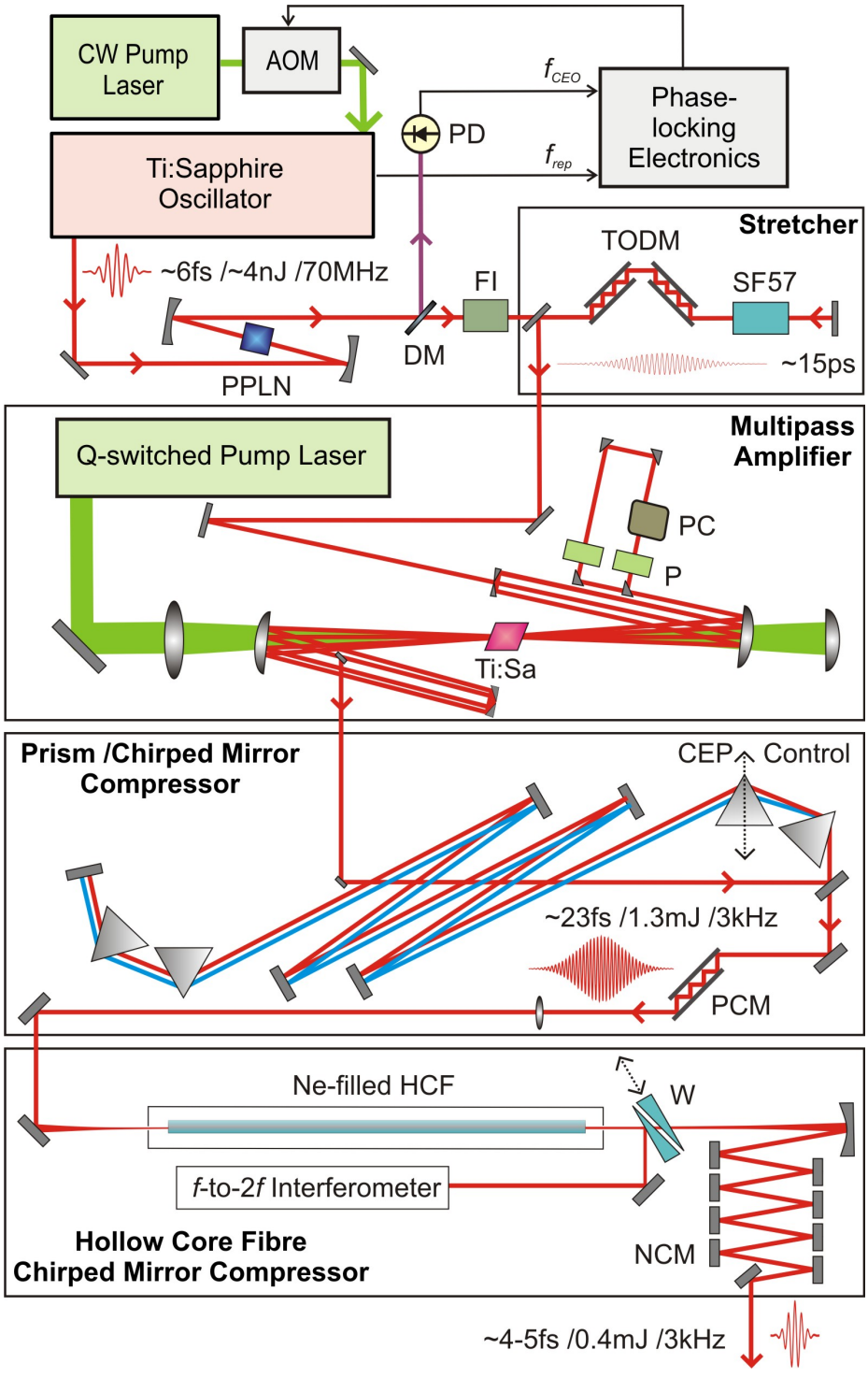

Figure 2.15: The femtosecond laser system: A continuous wave (CW) laser pumps the Ti: Sapphire oscillator, controlled with an acousto-optical modulator (AOM). Periodically poled MgO-doped lithium niobate crystal (PPLN); Faraday isolator (FI); dichroic mirror (DM); photodiode (PD); heavy flint glass (SF57); third order dispersion chirped mirrors (TODM); Pockels cell (PC); polarizer (P); positive chirped mirrors (PCM) hollow-core fiber (HCF); negative chirped mirrors (NCM); silica wedges (W); f_{CEO}: carrier envelope offset frequency.

(TODM) is the precompensation for higher-order dispersion which the pulses accumulate during their amplification. In a next step the signal is propagating in 5 cm of heavy flint glass (SF57), in which the pulses are temporally broadened up to 15 ps. Subsequently the oscillator pulses enter the multi-pass amplifier.

Multi-pass amplifier

Nine times the pulse is passing the amplifying crystal and every fourth pass single pulses are selected at a frequency of 3 kHz by a Pockels Cell (PC), acting as a pulse picker [160]. The main part of the amplifier stage is the highly doped Ti:Sapphire crystal, that is fed with a diode pumped Q-switched frequency doubled Nd:YLF laser with a power of 20 W at a repetition rate of 3 kHz. The Ti:Sapphire crystal is set to Brewster's angle configuration to minimize reflection loss [122]. Due to heating by the pump laser the crystal is cooled down to -70 $^{\circ}C$, thus minimizing thermal lensing effects. After passing the amplifier the pulse energy is increased up to approx. 1 mJ. Temporal compression of the pulse is explained in the next step.

Hybrid prism/chirped mirror compressor

The first stage of pulse compression is realized with a swift combination of 4 prisms and positive chirped mirrors (PCM). When entering the compressor the pulses remain slightly negatively chirped to avoid any SPM effects inside the prisms, which would lead to a spectral narrowing [158]. At the end of this hybrid compressor the pulse duration is compressed down to 23 fs with an energy of 1.3 mJ at a 3 kHz repetition rate, corresponding to a spectral bandwidth on the order of 70 nm [158].

Hollow-core fiber/chirped mirror compressor system

To obtain an additional pulse compression the pulses are spectrally broadened inside a hollow core fiber (HCF). The fiber with a inner diameter of 250 microns has a length of 1 m and is filled with Neon gas at a pressure between 1.8 and 2 bar. SPM is induced inside the fiber, resulting in a spectral broadening. The efficiency is on the order of 50 %. During the pulse propagation through the fiber the spectral bandwidth is extended to more than 500 nm reaching from 400 nm up to 1000 nm. The heavily positive chirped pulses are subsequently dispersion compensated by a set of negatively chirped mirrors (NCM). At this stage the pulses are compressed to a near single cycle with a pulse duration of 4-5 fs and a pulse energy of approximately 0.4 mJ. A small fraction of the laser is sidelined after the output of the HCF into a f-to-2f interferometer. This interferometer represents the "slow loop" feedback loop, where a pair of fused silica wedges steers the fine tuning of the CE-phase (description in section 2.3.2).

Sample holder

The SNOM-tip is glued onto a sample holder and connected to macroscopic contacts with silver liquid. The surrounding material is macor, a technical ceramic, highly insulating. At both ends the gold planes of the tip are macroscopically plugged to a pre-amplifier connected to a "lock-in" amplifier. The sample holder is fixed on a rotational plate to change the polarization of the incoming pulse with respect to the gap at the apex of the tip. This rotational plate with the tip on is set on a xyz-nano positioner to enable a precise positioning of the gap with respect to the incident laser pulses.

Lock-in amplifier

Before the electric signal from the nanojunction is transferred to the lock-in amplifier (*Stanford Research, SR830*) the current is converted into a voltage signal by the pre-amplifier from *Femto Messtechnik*, with the typical gain setting of $10^8 \frac{V}{A}$. The signal is transferred to the lock-in amplifier, which is locked to a frequency of 1.5 kHz (or integer multiples of this frequency). This corresponds to half of the repetition frequency f_{rep} of the CEP stabilized laser and gives access to electric signals originating from the CE-phase of the optical pulse. The time constants, which defines the time period for a signal averaging during experiments, is varied between 0.1-1 s. Data acquisition is performed with a *LabView* program.

2.3.2 Stabilization of carrier-envelope phase

In section 1.8 the CE-phase was introduced as a parameter in few-cycle laser pulses. It can be described as

$$E(t) = A(t) \cdot cos(\omega_L t + \varphi_{CE}), \tag{2.2}$$

A(t) is the electric field amplitude; ω_L the carrier frequency and φ_{CE} corresponds to the CE-phase. In general, a change of the CE-phase φ_{CE} inside an optical medium with a dispersive index of refraction is given by:

$$\Delta\varphi_{CE} = \left(\frac{1}{v_g(\omega_L)} - \frac{1}{v_p(\omega_L)} \right) L\omega_0. \tag{2.3}$$

A pulse propagating in a cavity of length L has the phase-velocity v_p and the group-velocity v_g that differ from each other, which results in a phase slippage. When considering the laser cavity of the Ti:Sapphire oscillator the φ_{CE} changes after each round trip. The pulses in the time domain are separated by $T = \frac{1}{f_{rep}}$, where f_{rep} is the laser repetition rate and T is the pulse period or cavity round-trip time [161]. In the frequency domain (see figure 2.16) the pulses are represented as comb lines within the laser spectrum, separated by f_{rep} [161].

The modes of the laser cavity are defined as:

$$f_a = f_{CEO} + a f_{rep}, \qquad a \in \mathbb{N} \tag{2.4}$$

where f_{CEO} is the carrier envelope offset (CEO) frequency and a represents the laser modes a. For the ideal case the phase-velocity v_p and group-velocity v_g are equal inside the cavity, thus f_{CEO} becomes zero. f_{CEO} results from the dispersion in the cavity for each round trip and is correlated with the CE-phase φ_{CEP} [161]:

$$\Delta\varphi_{CEP} = \frac{2\pi f_{CEO}}{f_{rep}}. \tag{2.5}$$

The CE-phase shift (eq. 2.5) is independent of the laser modes a, meaning all modes get the same phase shift (see eq. 2.5) [161]. Precise control and adjustment of the CEP is of highest relevance in our experiments, since we are interested in studying strong field effects in a solid and the time-structure of the electric field carried by a few-cycle optical pulse depends strongly on the CEP. The stabilization of the CEP in our set-up is split into two decoupled components. The first component is the "fast-loop" technique, where the CE-phase of the generated laser pulses from the oscillator is stabilized. This feedback loop works on a timescale of nanoseconds to compensate changes of the CE-phase caused by mechanical vibrations, air flow or other noise sources [162]. The second stabilization loop is termed as "slow loop", running at a frequency of 3 kHz. Slow CE-phase drifts are induced, when the pulses are guided through the multipass amplifier and the HCF [162]. These drifts mainly originate from thermal effects and are compensated with the "slow loop "technique [162]. Both stabilization feedback loops are described in the following two subsections.

f-to-zero interferometer

In 2005 Fuji et al. [163] introduced a new CE-phase "fast loop" stabilization that is implemented in the laser set-up (see figure 2.15). Figure 2.16 shows the basic principle of the f_{CEO} detection. As mentioned in section 2.3.1 either a DF or a SH comb in the nonlinear PPLN crystal are generated. In our set-up the DFG is employed. This difference frequency signal results from the mixing of the high frequency components ($mf_{rep} + f_{CEO}$) of the fundamental spectrum with its low frequency components ($nf_{rep} + f_{CEO}$) (see arrows in the fundamental spectrum in figure 2.16. The resulting DF comb is expressed as:

$$f_{DFG} = (m - n) f_{rep}, \qquad m > n \tag{2.6}$$

Thus the f_{DFG} frequency is independent of the f_{CEO}. At the same time SPM leads to a spectral broadening of the fundamental frequency comb f_a over an octave spanning region,

important for a spectral overlap of both (DFG and fundamental) components. The beat frequency results from the interference of the two frequency combs

$$f_{beat} = f_a - f_{DFG} = (a - m - n) f_{rep} \pm f_{CEO}, \qquad a > m, n. \tag{2.7}$$

The beat signal is bandpass filtered and detected by a photodiode. The beat signal is modulated by the f_{CEO}, thus it is obtained by frequency analysis. Due to eq. (2.5) the phaseshift is specified and can therefore be stabilized. The measured f_{CEO} frequency is compared with a fixed reference frequency $f_{ref} = \frac{f_{rep}}{4}$. The deviation signal is send to a proportional-integral (PI) controller, which feedbacks on an acousto-optical modulator (AOM). Inside the Ti:Sapphire oscillator the modulated power of the CW pump laser causes a phase shift caused by the Kerr effect. This fast loop method ensures that every fourth pulse leaving the oscillator has the same phase. The amplifying laser works at a frequency of 3 kHz, thus the frequency has to be down-converted. Therefore the Pockels cell acts as a pulse picker at 3 khz, the base for the second phase stabilization technique in the following subsection.

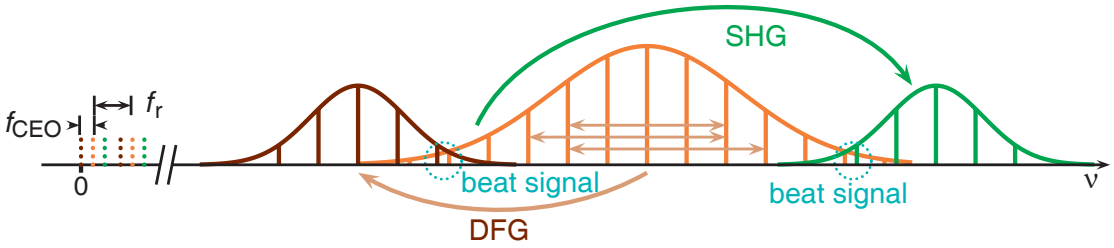

Figure 2.16: Visualization of frequency combs in the frequency domain for the detection of the carrier envelope offset frequency f_{CEO}. Adopted from [163].

f-to-2f interferometer

As already mentioned in section 2.3.2 a second phase stabilization loop (slow loop) is implemented to compensate slow phase drifting induced by the amplifier and the HCF. The f-to-2f method is based on the frequency doubling of the spectrum after the HCF. Therefore a wedge W (see figure 2.15 the HCF compressor components) at the end of the HCF reflects a small fraction of light into a beta-bariumborate (BBO) crystal, where the second harmonics of the fundamental frequency comb are generated. By overlapping the red part of the fundamental spectrum with the blue part of the second harmonic interference occurs. The resulting fringes are detected with a spectrometer in contrast to the f-to-zero technique, where a photodiode is applied. Due to the interference a frequency modulation Δf

is detected. This feedback loop acts on the piezo on which one of the prisms is positioned. By slightly changing the prism position, the propagation length and therefore the CEP is varied. The precise locking of the CE-phase provides control of the CE-phase by tuning the propagation length in a thin dispersive material, fused silica wedges in this case.

2.3.3 Tuning the carrier-envelope phase after stabilization

So far the CE-phase stabilization was examined. For the experimental approach a technique is required to tune the CE-phase in a controlled and reproducible manner as the optical excitation process is investigated as a function of the CEP. To realize this, the CE-stabilized laser beam is guided through a pair of fused silica wedges. In section 2.3.2 the equation (2.3) for the CE-phase change $\Delta\varphi_{CE}$ of a laser pulse propagating over a distance z inside a media with dispersive index of refraction was introduced. This equation can also be expressed in the following way [122]:

$$\Delta\varphi_{CE} = -2\pi \frac{dn}{d\lambda}|_{\lambda_L} z, \tag{2.8}$$

where $\frac{dn}{d\lambda}$ can be derived from the *Sellmaier equation* [122], a model for the description of $n(\lambda)$ for a given material and carrier wavelength λ_L. For fused silica at a carrier wavelength $\lambda_L = 700$ nm the derivative is $\frac{dn}{d\lambda}$, which corresponds to a distance z = 41.5 μm for a CE-phase shift of 2π. In the experimental set-up a pair of fused silica wedges is positioned on a stepper motor, where the wedges can be moved against each other by a distance Δx (see figure 2.14), thus changing the propagation length of the beam by the factor $\Delta z = \tan(2°48') \cdot \Delta x$ per wedge.

2.3.4 The interferometric delay stage

Figure 2.17 shows the experimental configuration for pump-probe measurements performed with the aforementioned laser system. This way the excitation of charge carriers and the motion control can be temporally decoupled as described in section 1.8.4 and spatially by polarization gating. The interferometric delay stage is positioned in front of the sample holder. It mainly consists of a broadband beamsplitter, a mirror, a $\frac{\lambda}{4}$ plate/periscope and a second mirror mounted on a piezo stage, which allows delaying both pulses relative to each other with sub-femtosecond precision. This stage can be moved over several microns with nanometer precision using a piezo control along the beam path. The incoming CEP locked NIR-laser beam is split into a transmitted drive pulse $\vec{E}_{drive}$ and a reflected pump pulse $\vec{E}_{pump}$. The periscope changes the polarization of the pump pulse by 90° with respect to the drive pulse. After the mirror reflection of both pulses they are brought together after the beamsplitter. The set-up is similar to a Michelson interferometer. The polarizations of both pulses are chosen in a way that the pump pulse is polarized parallel with respect to the gap

of the tip, whereas the drive pulse is polarized perpendicular to the gap. The delay stage enables the temporal decoupling of the charge carrier excitation pulse from the optical driving force. The time ($t_0 = 0$) is defined, when both pulses are spatially overlapped. This time corresponds to a delay stage position, where both pulses are identical in time, space and phase but different in their polarization and amplitude. This temporal overlap can be found by interference pattern of both pulses. Therefore a broadband polarizer is positioned right after the CEP-locking set-up. The function of the polarizer is to generate from both pulses a fraction having the same polarization which is essential for the temporal interference pattern. A CCD camera fixed in the laser beam path in front of the sample holder visualizes the focus of both beams. The delay stage is moved until fringes start to appear along the focused beam. These fringes correspond to constructive (bright colored fringes) or destructive (dark fringes) interference and therefore enabling access to time zero t_0.

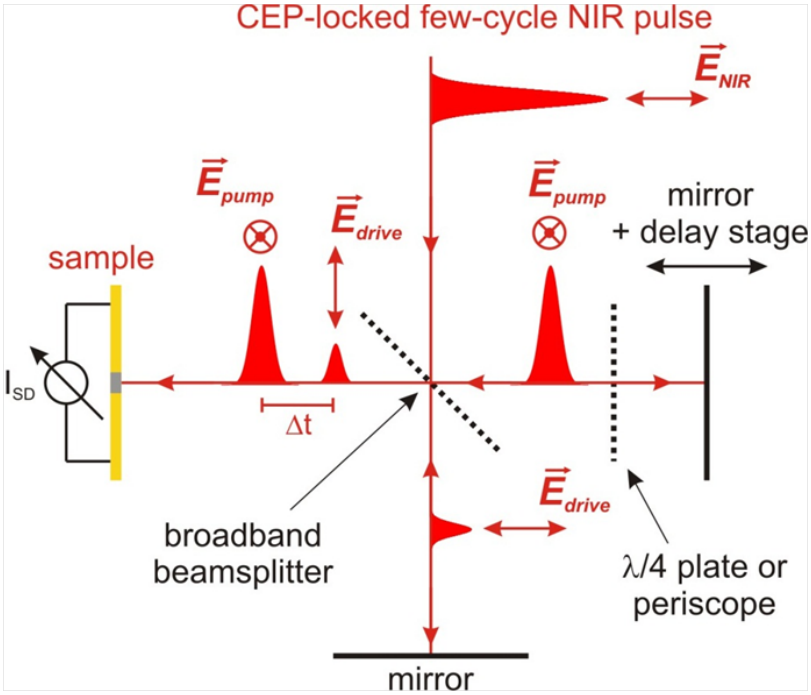

Figure 2.17: Interferometric delay stage based on a Michelson interferometer. With this configuration near single-cycle and CEP-locked NIR-NIR pumpe probe experiments are realizable. The optically-induced charge excitation in the dielectric is decoupled via polarization gating of the injection and control pulse. Temporally the pulses are synchronized and can be delayed with respect to each other.

3 Results and Discussion

In the first part of this chapter results of test experiments performed with the home-made single-molecule transport set-up described in section 2.2 are discussed. Subsequently light induced electron transport measurements of two different mutations of single cyanobacterial photosynthetic protein complexes are presented. The electron transport is described in the picture of hopping transport which was introduced in section 1.2.3. In the second part of this chapter we present the collective electron motion inside metal-dielectric-metal-nanojunctions optically exposed to ultrashort laser pulses, whereby the direction is steered with the CE-phase of the pulses. To decouple the electron excitation process inside the dielectric from the steering of the excited electrons towards the electrodes, two-pulse experiments have been performed. The experimental results are discussed with possible theoretical models in the picture of ballistic electron transport (see section 1.3).

3.1 Test experiments

As the experimental set-up is home-made it is of great importance to perform preliminary measurements to test whether required properties are fulfilled and to optimize the experimental procedure. In the following section the prearrangement and experimental results are presented.

3.1.1 Optical properties of multimode fibers

First experimental data, where only one optical fiber for both light coupling and collection was utilized, revealed a huge background signal arising from the fiber itself. This high optical background originates from Raman background and fluorescence that is present in quartz glass fibers, when getting excited with high laser intensity [164–166]. To minimize the background signal, multimode fibers from different manufacturers were studied. The set-up for this experiment is quite simple. Light from the He-Ne laser is focused onto a beam-splitter and subsequently into the one end of an optical fiber fixed on a stage. The total length of the optical fiber is 50 cm. With the beam-splitter the backscattered light is transferred through a Raman-edge filter into the spectrograph. Fluorescence in optical fibers mainly originates from the coating material, when the light is not precisely coupled into the fiber core [164–166]. In figure 3.1 the investigated fibers, with their specific

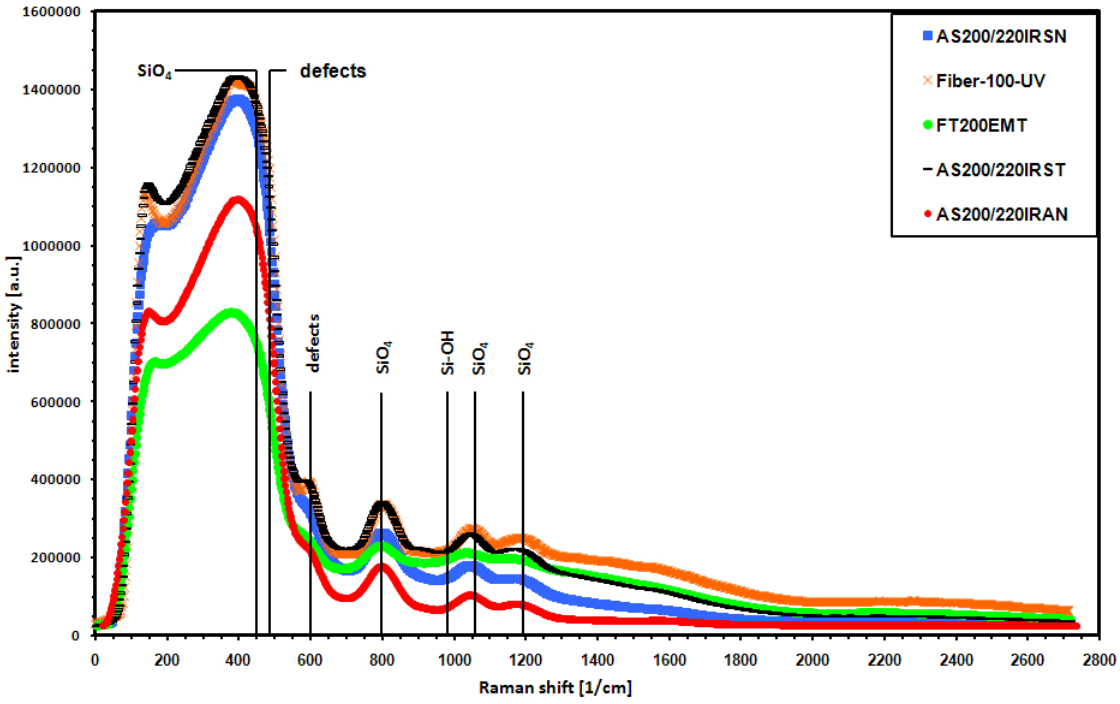

Figure 3.1: Raman background of the investigated optical multimode fibers: The broadened Raman modes at 450, 800, 1055 and 1195 $\frac{1}{\text{cm}}$ originate from SiO_4 vibrations, while the vibrations at 970 $\frac{1}{\text{cm}}$ can be referred to SiOH. Defects are responsible for modes at 491 and 604 $\frac{1}{\text{cm}}$ [164]. In the experiments the fiber AS200/220IRAN revealed the lowest Raman background signal.

Raman modes are shown. These Raman modes originate from SiO_4, SiOH and defects. The experiments revealed that the lowest background signal is measured with the multimode fiber AS200/220IRAN (*Fibertech*). This results are consistent with experimental data from Santos et al. [166] and therefore this fiber was chosen for further experiments. The AS200/220IRAN fiber is composed of a 200 μm fused silica core with a NA of 0.2, surrounded by a silica-silica cladding, followed by a acrylate coating and a nylon jacket around. It is optimized for the visible and near infrared wavelength regime. At both ends the coating and the jacket are removed. The ends are cleaved to obtain a straight surface to maximize the light coupling into the fiber.

3.1.2 Tip-substrate distance control

After fixing a SNOM-tip on the sample holder with silver colloidal liquid (see section 2.2.3), the sample holder is put onto its designated mount. After gluing, the apex of the SNOM-tip is typically located several tens of microns above the gold substrate. Subsequently the SNOM-tip, gold substrate and piezo are interconnected to a home made feedback loop system. To approach the tip into the working distance of the piezo, the differential thread is screwed slowly until a given target tunneling current is obtained and the feedback loop is retracting the sample. Subsequently the set-up is connected to the sourcemeter. Thereafter the UHV-chamber is closed, pumped to a pressure below 10^{-7} mbar and a computer controlled feedback loop program is started, feedbacking with a given voltage on a target current (typically 0.1-0.8 nA at 0.25 V).

With the measured time trace of the piezo creep and the measured current, one can identify whether the apex of the SNOM-tip is in good shape after installation and manual approach. In figure 3.2 typical time traces of a new SNOM-tip and an unstable tip are shown.

Figure 3.3 shows a first control measurement. A DC-voltage of 10 mV is applied between a bare gold substrate and the SNOM-tip, while the substrate on top of the piezo is slowly approached and the current is measured. In this measurement no light is coupled into the apex of the SNOM-tip. At a certain distance a tunneling current can be measured, exponentially increasing until a metallic contact has formed. When subsequently retracting the gold substrate, quantized conductance (see section 1.3) in multiple integers of $G_0 = 2 \cdot e^2/h$ is observed [59, 60]. This step-like conductance has been similarly studied with mechanically controlled break junctions (MCBJ) performed by Scheer et al. with various metals [61,62]. These measurements show that the required precision and stability for single molecule transport measurements is given and indicate that an atomically sharp contact has formed.

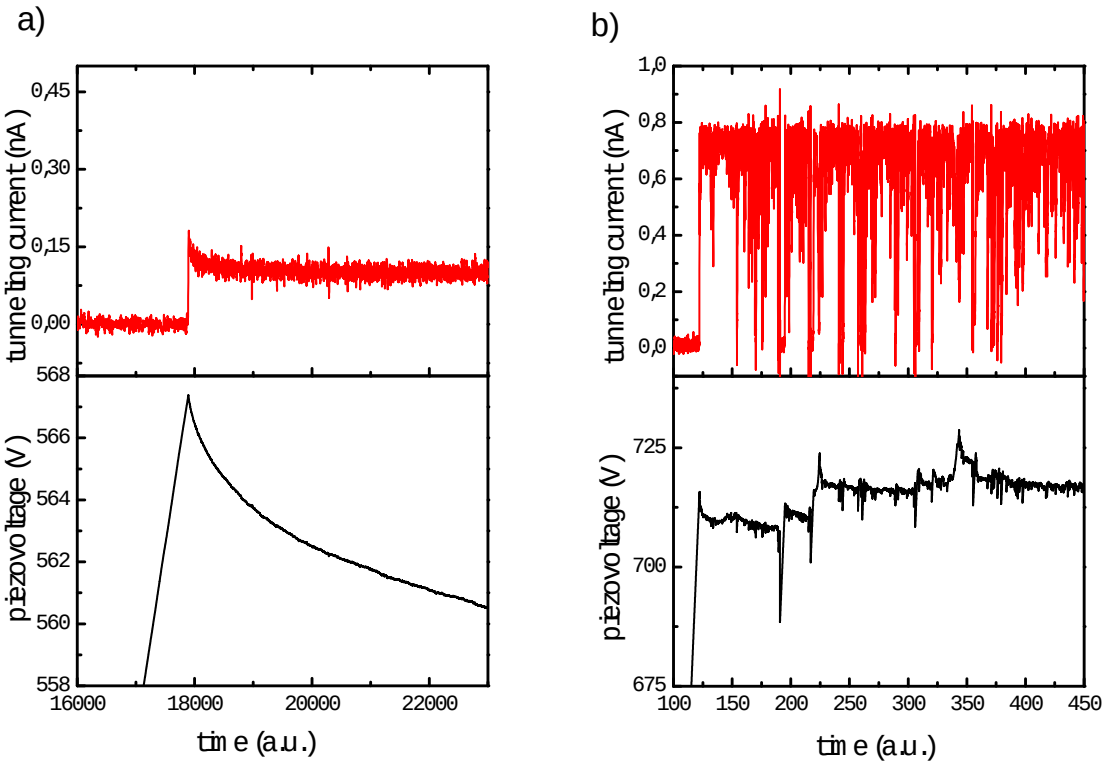

Figure 3.2: Time trace of measured tunneling current (top) feedbacked on a given target current and the applied piezovoltage (bottom). a) The target tunneling current is 0.1 nA at a bias voltage of 0.25 V. The stable time trace of the tunneling current reveals that the apex of the SNOM-tip is sharp and in good order. The piezovoltage time trace shows a piezo creep, which is characteristic for piezo actuators. b) The time trace (tunneling current is set to 0.8 nA at 0.25 V) of the tunneling current respectively the piezovoltage is unstable over time, indicating an unstable tip.

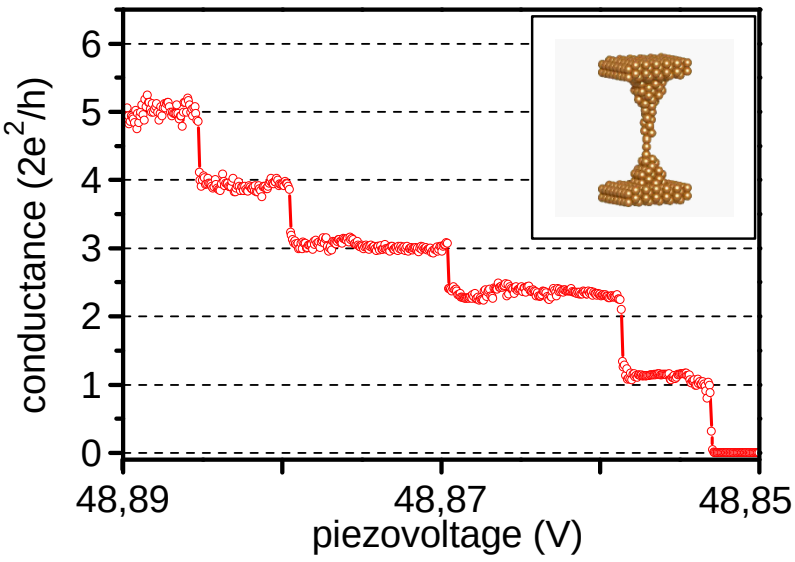

Figure 3.3: Conductance quantization can be observed when a metallic (Au) interelectrode contact is established and subsequently broken indicating that an atomically sharp junction has formed. The piezo can be controlled with a sub-Ångstrom precision in a range of up to 10 μm. The conductance is stated in units of $G_0 = 2 \cdot e^2/h$.

3.1.3 Efficiency of light coupling into the SNOM-tip

A first preliminary experiment to estimate the efficiency of the light coupling was done with a white light source (see section 2.2.3). Beginning with the illuminated SNOM-tip in tunneling contact the reflected light was recorded with the GRIN lens fiber over a wavelength regime from 600 to 740 nm. The gap between substrate and tip was increased in steps of 40 nm up to 2 μm, measuring the spectrum at each step. Figure 3.4 shows an absorption spectrum (left) and a simulation (right). Each measured spectrum is normalized to its averaged intensity. Readily identifiable on the left in figure 3.4 is an optical standing wave pattern that can be attributed to specific distances between tip and substrate where the distance fits with multiples of the excitation wavelengths. In case of a minimum in the absorption, the wavelength or its multiples do not fit to the given distance in contrast to a maximum absorption, where a standing wave between tip and substrate is formed. For increasing wavelength the maxima/minima are shifted to larger distances. This case can be easily simulated by the summation of two spheric waves propagating in reverse directions (see figure 3.4 on the right hand side) forming a standing wave pattern between tip and substrate. A measurement with a different SNOM-tip is shown in figure 3.5 and revealed an interference of two standing waves. For this simulation, we assumed an object on the sample with an offset of about 500 nm with respect to the first standing wave, backscattering light

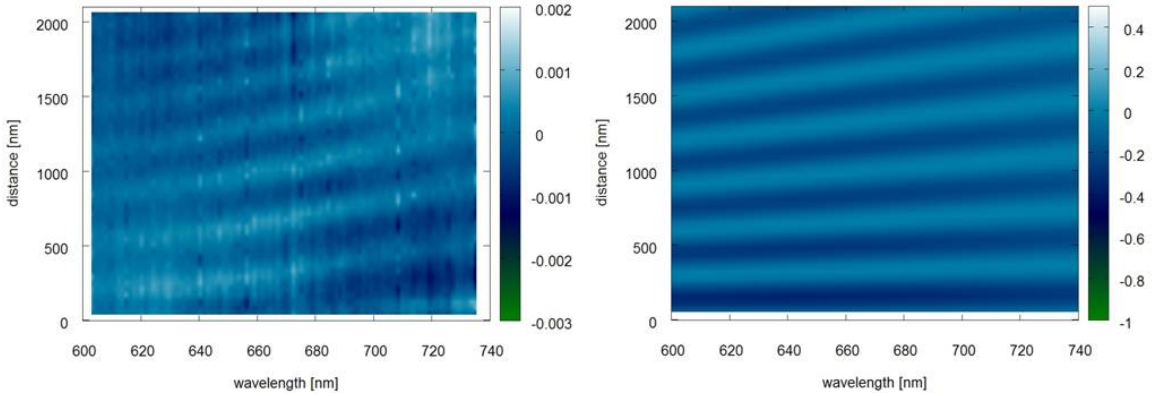

Figure 3.4: Beginning with the tip in contact with the substrate, the gap between substrate and illuminated tip is increased in 40 nm steps up to 2 microns. At each step a spectrum is recorded. Left: Spectra of the reflected light from the SNOM-tip for increasing distance shows an optical standing wave pattern between the tip and the substrate. Right: Simulation of a single standing wave pattern.

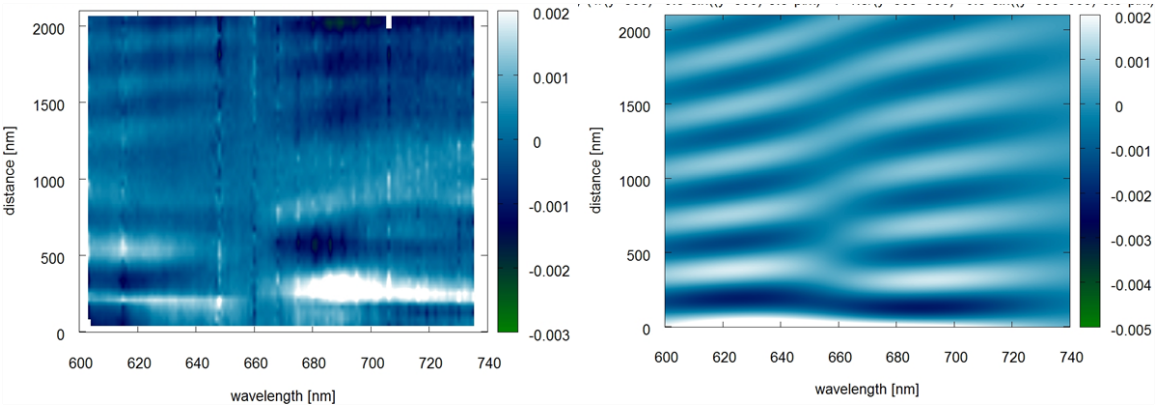

Figure 3.5: Absorption spectra for a different tip-sample system with the same parameters. Left: Spectra for increasing distance show interference of two standing waves between tip and substrate. Right: Simulation of a superposition of two standing waves where the second wave originates from a local light scatterer with an offset of about 500 nm with respect to the first standing wave.

and thus modifying the inference pattern. The simulation is depicted in figure 3.5 on the right hand side, giving an explanation that two standing waves interfere. To conclude, the measurements reveal that light is coupled into the apex and the resulting interference tip and sample. Furthermore the data indicate that the set-up is spectroscopically sensitive to the region of the SNOM-tip at the length scale up to microns.

3.1.4 Sensing the optical near-field

Additionally the near field of the gap region was studied. Therefore spectra in the short range from tunneling contact to 100 nm gap distance were recorded. In figure 3.6 a data set for a near-field measurement with a white light source is depicted. For some measurements strong intensity changes on the length scale of 30 nm are observed, as visualized in figure 3.6, indicating a near field at the apex of the SNOM-tip.

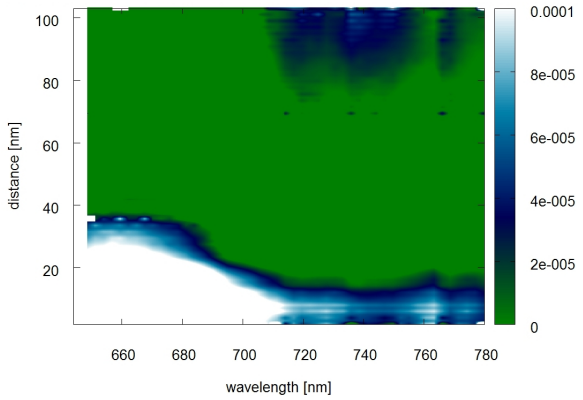

Figure 3.6: Significant signal changes on a length scale of 20 nanometers indicate a strongly localized near field at the apex of the tip.

3.1.5 Influence of laser light on the tip sample elongation

Before performing transport measurements on single molecules the behavior of the SNOM-tip in tunneling contact under laser illumination has to be studied. Therefore the feedback controlled tunneling current of 1 nA was maintained constant at a bias voltage of 2 V. Subsequently the readjustment of the piezo when switching the laser on and off is monitored. Figure 3.7 shows the time trace of a typical data set of the repeated piezo response when the laser beam couples into the tip for 10 s. Thereupon the laser is blocked for 2 minutes. Clearly visible is the retraction of the substrate, when the laser beam is focused into the apex of the tip. The readjustment of the piezo can be explained by heating of the SNOM-tip due to laser radiation. This results in a thermal expansion, which is compensated by retracting the substrate. There are different parameters influencing the piezo response.

Main parameters include the quality of light focusing into the apex of the tip, the geometry of the tip and the laser power. This piezo response is a hint for the quality of the laser coupling, as a big thermal expansion suggests a good coupling. In the following experiments the laser illuminated "hot" tips are approached to the tunneling regime to ensure that the tip stability is maximized.

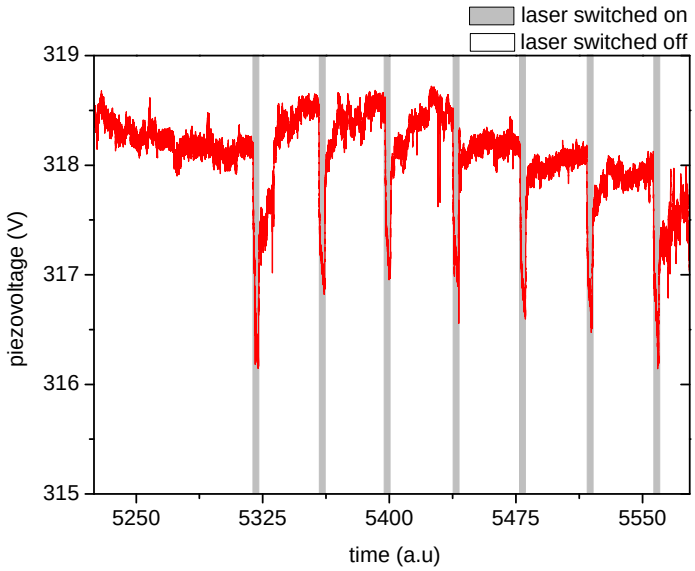

Figure 3.7: Time trace of the response of the feedback loop maintained at a constant current of 1 nA/2 V when the laser beam couples into the tip for 10 s (gray-shaded) and thereafter is switched off 2 minutes to regain thermal equilibrium. The change of the piezo height gives access to the tip elongation due to thermal expansion. Also the quality of light coupling into the apex is monitored by the response of the feedback loop.

Conductance measurements on single molecules

After testing the efficiency and stability of the set-up, first measurements with single molecules at room temperature have been conducted. Thereby the pure gold substrate was replaced by a gold substrate covered with a monolayer of the spatially small and symmetric molecules 9,10-bis(2'-para-mercaptophenyl)-ethinyl-anthracene (see section 2.2.2). In a first step the substrate was manually approached with a bias voltage of about 250 mV to the SNOM-tip and stopped below it. After waiting for 2 hours to minimize piezo drifts, the approach with a step size between 0.3 and 1 Å was sustained. The manual approach was continued until the exponential tunneling regime was reached. At this point the approach is slowed down and stopped as soon as a sudden step like increase of the current in the 10-40 nA range was recorded. The value of the current jump strongly depends on

the molecule but also the atomic configuration of the gold at the apex of the SNOM-tip and the substrate [50]. This current jump is named "lock-in behavior" and indicates that a molecule has closed the contact between the substrate and the SNOM-tip [50]. When a stable metal-molecule-metal contact configuration has formed, IV-curves are recorded. This procedure was started by gradually decreasing the applied voltage down to zero, thereafter several current-voltage-characteristics in the range of $\pm$ 1.5 V were recorded until the metal-molecule-metal configuration gets unstable or is broken. The average acquisition time for one IV-curve is 15-25 seconds. After the contact was broken, a new approach was started. This procedure can be repeated any number of times, as the molecule is not considered to be destroyed when the contact is lost. In figure 3.8 two subsequently measured current-voltage-characteristics (red curves) and the resulting differential conductance (blue curves) are depicted. The results are analogous to the electron transport measurements through the same molecules (see section 1.2.1) performed with the MCBJs technique by Reichert et al. [16, 50]. The results prove that single molecule transport measurements are realizable with this home-made set-up. Although the high mechanical stability of a MCBJ is not achieved, the stability is sufficient to perform these experiments.

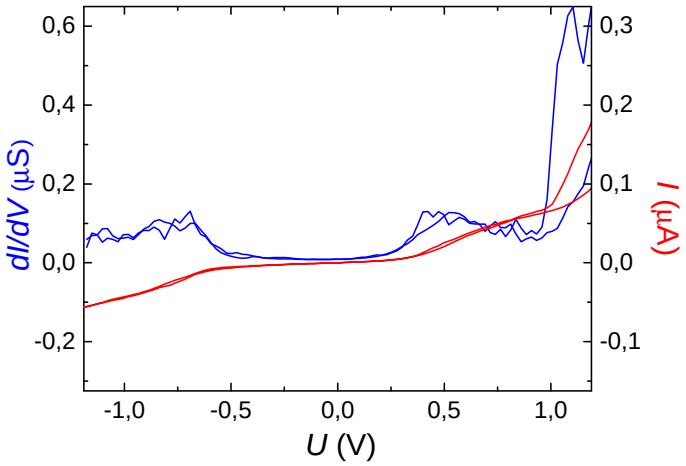

Figure 3.8: Typical current-voltage characteristics (red: current, blue: differential conductance) of a stable single molecule contact configuration are shown. Inset: Visualization of the spatially symmetric molecule [9,10-Bis(2'-para-mercaptophenyl)-ethinyl-anthracene] with which the transport measurements are performed.

3.2 Photocurrent of a single photosynthetic protein

As introduced in section 1.7.5, site-directed mutagenesis was the starting point for the specific modification of peptide-groups in bacteria. In 2005 Frolov et. al [92] succeeded to genetically mutate PS I from the robust cyanobacteria species *Synechocystis sp.* PCC6803

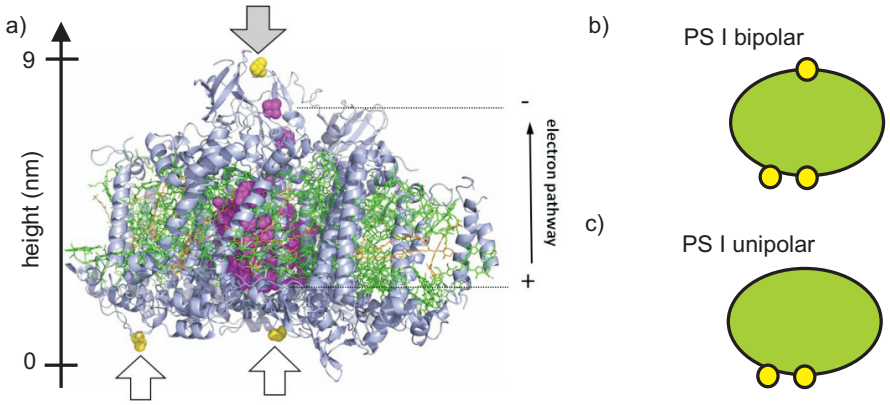

Figure 3.9: Structure of genetically mutated Photosystem I from cyanobacteria: a) Three cysteine mutations - two at the oxidizing (white arrows) and one at the reducing side of PS I are selected to be in close proximity to the electron transport chain. b) PS I with three cysteine mutations is named as *bipolar PS I*. c)*unipolar PS I* species has no mutation at the reducing side of PS I. Figure 3.9a) adopted from [27].

via site-directed mutagenesis. Thereby amino groups of the PS I are modified to cysteine groups, which are well known to form covalent bonds to a variety of metals including gold [92]. In these experiments only amino groups without steric hindrance when bound to a gold or functionalized semiconductor surface as well as to carbon nanotubes are genetically changed to cysteines [27, 92, 111, 167]. Two cysteine mutations D235C/Y634C close to the reaction center core *P700* are selected, at the oxidizing side of the PS I, as depicted in figure 3.9 a) and marked with white arrows [27]. At the reducing side of PS I at minimal distance to the ETC a third cysteine mutation is situated, marked with a grey arrow in figure 3.9 a) [27]. In figure 3.9 b) and c) pictograms of the two different PS I mutation species to be studied in the subsequent experiments are visualized. The PS I species with two mutation at the oxidizing and one on the reducing side is named *bipolar PS I*, whereas in *unipolar PS I* the mutation at the reducing side is missing. Carmeli et al. [27] confirmed that cysteine mutated PS I form covalent bonds to gold but not to SiO_2. The optical properties of mutated PS I carbon nanotube hybrid systems were studied by Kaniber et al. [28, 102, 113], as described in section 1.7.6.

3.2.1 Lock-in behavior of the Photosystem I

The procedure to explore the “lock-in behavior”of unipolar and bipolar PS I complexes was performed without laser illumination at room temperature in the following way: Up to a given target tunneling current of 0.5-100 nA at 0.25 V bias voltage the tip was approached and subsequently retracted. Our current-distance curves revealed that three different con-

ductance regimes are distinguishable, visualized in figure 3.10. Above 9 nm, the junctions behave roughly like a tunneling barrier with decreasing barrier width. Between 9 and 3 nm, a finite current of about 300 pA with fluctuations of 200 pA is observed for the bipolar PS I. Below 3 nm, the current increases rapidly in a non-systematic manner for both PS I species. The current fluctuations always occur, after the first touch of the tip with the molecule. At closer distance the apex of the tip is pushed into the soft protein. In figure 3.10 a) a typical current-distance profile of the bipolar PSI is visualized. At the point where the bipolar PS I touches the SNOM-tip the current-distance profile gets irreversible. It is assumed that the protein is covalently linked to the tip. When retracting the tip after touching it a strongly fluctuating electric current is measurable over distances of more than 25 nm until it drops to zero. After the contact is broken, the situation at the apex of the tip is undefined at SNOM-

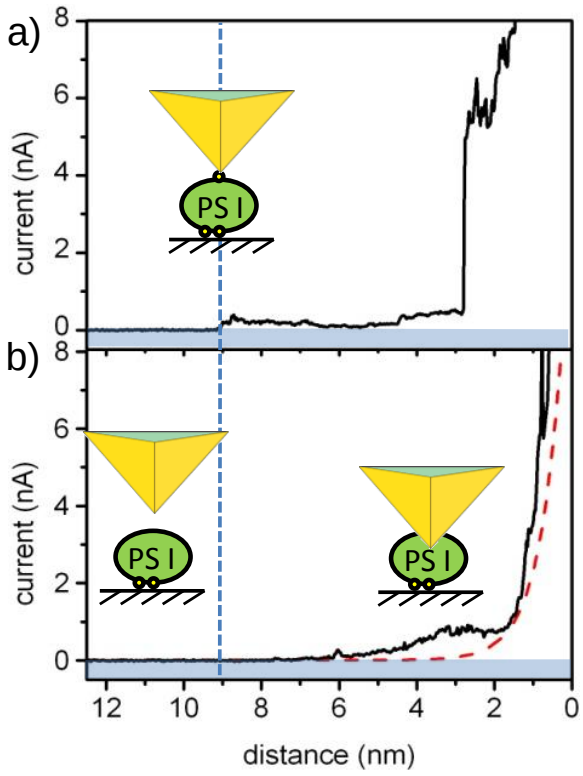

Figure 3.10: a) Dark current vs. gap distance for sub-monolayer of a bipolar PS I measured under vacuum conditions at V_{bias} = 0.25 V. (b) Identical curve for a sub-monolayer of unipolar PS I. The red curve displays the measured vacuum tunneling without photosystem proteins on the substrate.

tip as the PSI is broken. For this reason the SNOM-tip is replaced every time it came in contact with a protein. As a consequence the ultra high vacuum has to be broken and the aforementioned procedure has to be repeated. In the control experiment current-distance profiles without light of the unipolar PSI are measured and diagrammed in figure 3.10 (b).

Clearly visible is the missing step-like increasing current at a distance of 9 nm compared to the bipolar PSI, indicating that no covalent linkage has formed, since the cysteine mutation at the reducing side of the PSI is missing. From 6 to 2 nm, a distance where the apex is already deforming the protein, a shoulder-like increase of the current is measured. Below 2 nm the current through the bipolar PSI increases in an non-systematic manner. In figure 3.11 the entire tip-approach profile up to the given target tunneling current of 20 nA at 0.25 V as well as the subsequent retraction is depicted for the bipolar PS I until the current has dropped down to zero. At a distance of approx. 9 nm first current fluctuations start to appear, indicating that a covalent bond between the PS I and the SNOM-tip has formed. In the retraction curve of figure 3.11 one can identify current fluctuations up to 55 nA, an indication that the PS I is lengthened and unfolded until the protein complex breaks apart and the current decreases to zero. This sort of "hysteresis" was also observed for the unipolar PS I, also the distance from the first contact to the current drop was on the same order of approx. 25-30 nm. Thus for both cases, when the tip is quenching the molecules a chemisorbed bond is built up as the strong hysteresis indicates. The additional cysteine group at the reducing site of the bipolar PS I seems to act as a distance marker, which is missing for the unipolar species.

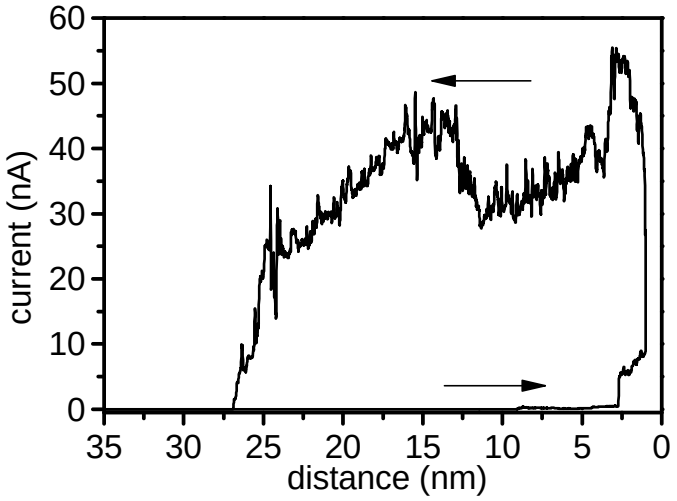

Figure 3.11: A typical current-distance profile of a bipolar PS I with the approach curve (blue) and the subsequent retraction curve (red) after a target tunneling current is achieved. Clearly visible is the long range hysteresis when retracting the tip. At a distance of 9 nm the first current fluctuations occur during the approach. When the tip is retracted current fluctuations up to 55 nA are measured, suggesting that the protein complex is lengthened and unfolded until the bond is broken.

3.2.2 Photocurrent of a single Photosystem I

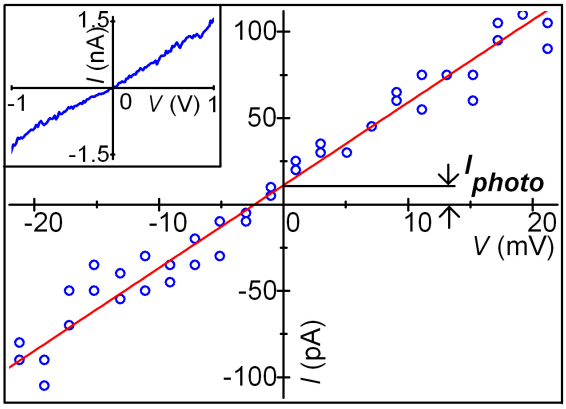

Figure 3.12: Typical current-voltage dependence of a bipolar PS I under laser excitation close to zero bias. Y-interception of linear fit defines residual current I_{photo} at zero bias (i.e. 11 ± 13 pA). Inset: The dependence up to $|V_{bias}| = 1$ V.

For both bipolar and unipolar PS I, the current-voltage characteristics were recorded under laser excitation after first fluctuations appeared in the current-distance curve. For a low bias voltage $V_{bias} < 50$ mV, the molecular junctions show a linear current-voltage dependence (inset of figure 3.12). For $|V_{bias}| \geq 0.5$ V, the characteristics become more and more non-linear. Non-linear characteristics have been reported both for transport across single reaction centers without laser excitation [108, 168, 169] and for corresponding photoconductance-voltage characteristics [25, 26]. In order to determine a value for the photocurrent, the current-voltage characteristics under light excitation are fitted linearly for $|V_{bias}| \leq 20$ mV. These fits are analyzed for their residual current at zero bias (short circuit current, see also in section 1.4) which we define as I_{photo}. The histograms of I_{photo} in figure 3.13 show the accumulated photocurrent measurements for samples exhibiting a positive offset (red) and negative (blue) offset. The different signs of I_{photo} are attributed to the two possible orientations of the bipolar PS I with respect to the applied bias direction. $I_{photo} > 0$ is expected for PS I molecules which are anchored with the twofold sulfur-terminated oxidizing side on the substrate (see figure 3.9). The results demonstrate that the photocurrent direction is determined by the orientation of the PS I with respect to the surface. The average absolute value of the photocurrent of 6 junctions in 77 measurements is 9.8 ± 5.1 pA irrespective of the direction. The photocurrent fluctuations are at the same order of magnitude for subsequent measurements. These strong fluctuations, which do not exist in the absence of the PS I layer (green histogram) are an inherent feature of the PS I protein complexes and agree with the above conclusion that the tip is in contact with the PS I. This kind of single molecule fluctuations have been previously recorded in similar

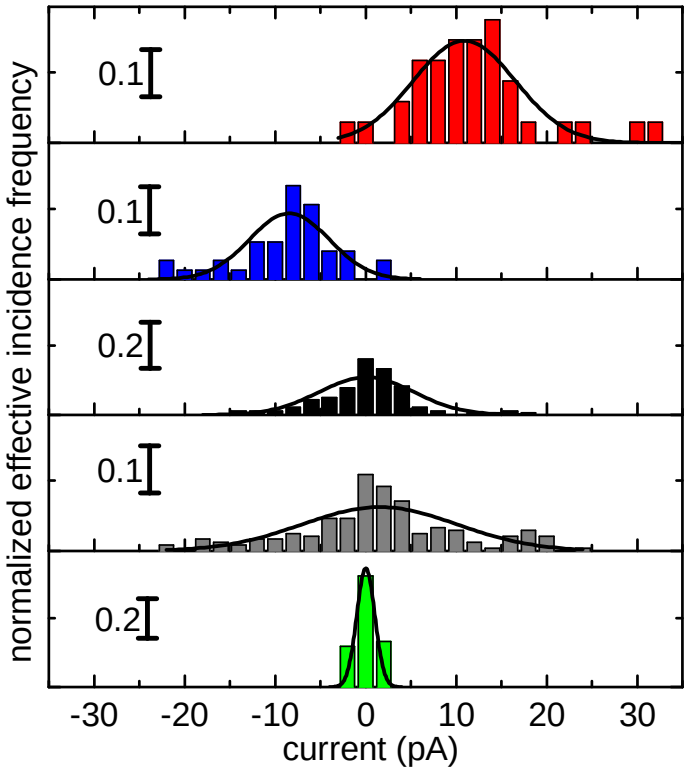

Figure 3.13: Red: histogram of I_{photo} for different illuminated single bipolar PS I junctions showing a positive offset when contacted. Average photocurrent: 11 ± 5.6 pA. Blue: Photocurrent histogram of different illuminated single bipolar PS I junctions showing a negative offset. Average photocurrent: -8.4 ± 4.4 pA. Black: corresponding histogram for different bipolar PS I junctions (red and blue) without illumination. Average residual current: $+0.09 \pm 5.3$ pA. Gray: Photocurrent histogram taken from different unipolar PS I molecules under illumination. Average residual current: 1.5 ± 8.6 pA. Green: Residual histogram for several measurements without photosystem taken at a comparable tunneling conductance and illumination of the tip (average: 0.021 ± 1.0 pA). The histogram heights are normalized according to the probability of their occurrence.

experiments exploiting break junctions [16, 170]. The fluctuations are also present when the tip is in contact with a bipolar PS I without illumination (black histogram). For the unipolar PS I, we do not observe any significant short circuit current (gray histogram). This demonstrates that in order to obtain an efficient electron transfer the PS I should be covalently bound to both top and bottom electrodes and in agreement with recent studies on single molecules [17] and reaction centers [171]. One of the most significant results in our experiment is the intriguingly large value for I_{photo} of 10 pA. It translates into a turnover time of $16 \cdot 10^{-9}$ s, i.e., every 16 ns an electron transverses the PS I covalently bound between the two electrodes. As suggested in figure 1.12, a photoexcited electron reaches F_x in 15 ns at the earliest. This is very close to the rate we deduce from our photocurrent measurements. The expected limiting step of the electron transfer is the electron transfer from the F_x to $F_{A/B}$, which seems to be overcome by a direct transfer process to the covalently bound tip. This interpretation is consistent with the rather high dark currents of 1.5 nA at $V_{bias} = 1$ V (inset in figure 3.12) that suggest that the electron transfer to the top electrode is not limited by the second slower stage. In particular, our dark current values are consistent with results measured for a reaction center coated Au tip [169]. The measured photocurrent, however, is higher than simple expectations based on the electron transfer rates of PS I in solution [57]. Recent studies demonstrate that the electron transfer in proteins in the dry state can be several orders of magnitude higher than in solution [54]. Dry proteins pass orders of magnitude higher currents than saturated molecules, and the current values are nearly comparable with the ones across conjugated molecules. Generally, the largest photocurrent achieved to date is from a multilayer photovoltaic cell, in the order of tens of $\frac{\mathrm{mA}}{\mathrm{cm}^2}$ for 0.1 $\frac{\mathrm{W}}{\mathrm{cm}^2}$ illumination [172]. Assuming an internal quantum efficiency close to 1 [95,99] and an absorption of a PSI monolayer of 0.003 at 633 nm, the electron transfer time of 16 ns suggests a photon flux of at least $2 \cdot 10^{10}$ $\frac{1}{\mathrm{s}}$. This value translates to a near-field intensity of 3.5 $\frac{\mathrm{kW}}{\mathrm{cm}^2}$ in our set-up. Along with the incident laser beam power that we measured to 4 mW it is possible to estimate the field enhancement factor g, introduced in equation 1.7 of section 1.5.2. For a beam spot-size of 100 μm, we obtain an incident laser intensity of 50 $\frac{\mathrm{W}}{\mathrm{cm}^2}$. The enhancement factor is determined to $g = \sqrt{\frac{I_{near-field}}{I_{incident}}} = \frac{E_{near-field}}{E_{incident}} \approx 8$. Most importantly, the photocurrent density generated by a single PS I gives a value of 0.15 $\frac{\mathrm{mA}}{\mathrm{cm}^2}$ for 0.1 $\frac{\mathrm{W}}{\mathrm{cm}^2}$ illumination, which is comparable to values of multilayered molecular photovoltaic cells [172].

3.2.3 Photocurrent at first contact

Our experimental data clearly identified a significant photocurrent for the bipolar PS I. The tunneling current with the PS I in contact does not allow direct access to the distance, as the molecular fluctuations induce permanent conductance changes. Thus the distance

is not known during the measurements, except that we are in contact. For an estimation of the distance, one would have to establish a metallic contact, destroying the junction as described in section 3.2.1. During the experiments the distance may change due to rearrangements of the electrode atoms in the strong electric fields and due to drifts. For this reason the distance was varied during the experiment to keep the conductance in the same regime and to explore the highest I_{photo} measureable. As a control experiment we performed a series of experiments when we detected the photocurrent exclusively at the first contact to the molecule. The experiments revealed a very low, probably insignificant photocurrent, that is much smaller than the current fluctuations. The IV-curves were performed with bipolar PS I in contact. Figure 3.14 shows the histogram as a summation of measurements revealing a mean photocurrent of 1.75 ± 2.3 pA. From 45 tip approaches 21 did not hit a molecules, whereas 24 approaches showed the typical fluctuating behavior as already described in section 3.2.1. 6 of the 24 tip-approaches exhibited a photocurrent between 0.5-2 pA. Translating this photocurrent into a electron transfer time results in 92 ns, which is sill above the expected time of 200 ns for the transfer from F_x to $F_{A/B}$ (see figure 1.11) [99]. A further possible interpretation could be the mixing of the 200 ns and 15 ns events, which then would sum up to a mean transfer time of ≈ 100 ns.

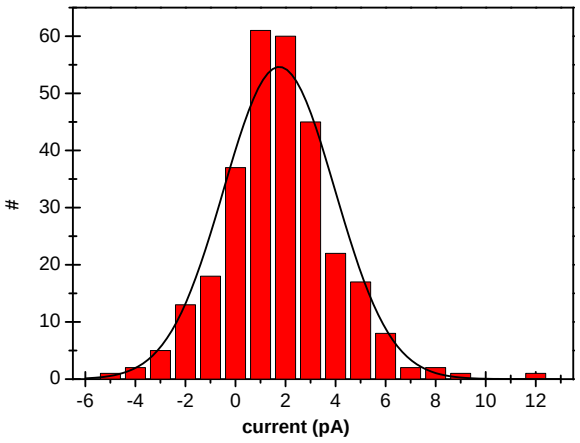

Figure 3.14: Histogram of the current at zero bias voltage accumulated for 6 different tip approaches (from 45 approaches in sum) where a photocurrent emerged. The mean photocurrent is 1.75 ± 2.3 pA.

3.3 Lightwave electron motion control in a metal-dielectric-metal nanojunction

In this section the results measured with the femtosecond laser system introduced in section 2.3 are presented. The section is divided into five main parts. First, simulations of the electric field distribution at the nanojunction are presented. The second and third subsections deal with the optical injection of charge carriers with sub-4 fs near-single cycle pulses as a function of the CEP and the laser power. In the fourth part the results from experiments obtained by the interferometric set-up (see section 2.3.4), with the goal to decouple the injection from the driving process are explained. This chapter ends with a qualitative discussion of possible charge carrier injection mechanisms inside the dielectric SiO_2. All experimental data shown in this section were performed in ambient atmosphere at room temperature.

3.3.1 The SNOM-tip as a probe in ultrashort laser spectroscopy

Since the optically-generated electric current is given by the temporal structure of the optical electric field at the junction, it is necessary to evaluate such a field right at the junction. This is achieved via FDTD simulations. We consider a Gaussian 4 fs VIS/NIR pulse with 750 nm carrier wavelength impinging on a 50 nm metal-dielectric-metal nanogap [145,173]. The goal of this simulation is to gain insight into the electric field distribution and light confinement at the apex of the tip. All simulations are performed for laser pulses polarized perpendicular with respect to the gap of the tip. The data set shown in figure 3.15 was simulated by Sascha Mühlbrandt for this diploma thesis [173].

The image represents a snapshot of the propagating electric field at the illuminated gap region at the time, when the electric field of the pulse is highest close to the electrodes. Clearly identifiable in this illustration is the confinement and enhancement of the electric field across the gap. An estimation of the enhancement can be obtained by calculating the ratio of the incident laser pulse E_0 and the local electric field E along the gap of the tip. Along the gap the simulation shows an enhancement on the order of 2 (see green curve on top of figure 3.15). The enhancement can be explained by excitation of localized plasmon resonances at the apex area of the tip (see section 1.5). The highest enhancement is achieved close to the electrodes with a field enhancement factor $g = 3$. Figure 3.16 depicts the electric field strength of a 4 fs laser pulse propagating towards the gap of the SNOM-tip (blue) and the field in the gap at the position of maximum field enhancement (red) over time. A strong asymmetric tail is observed, which temporally broadens the pulse to more than 5 fs. The calculated significant field enhancement makes the nanojunction a promising candidate as a solid-state phasemeter. However, a direct mapping of the laser pulse is not

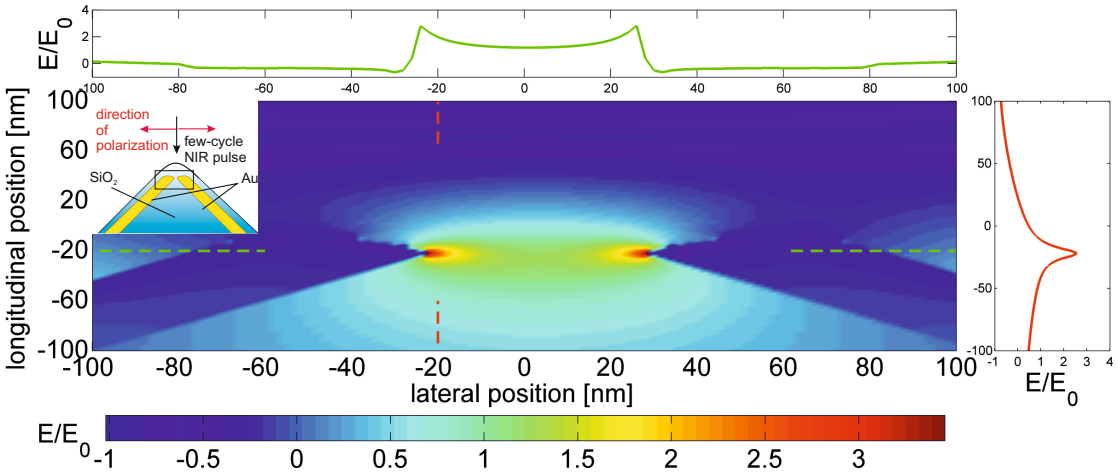

Figure 3.15: FDTD-simulation of the spatial electric field distribution at the nanogap of the SNOM-tip covered with a SiO_2 capping irradiated with 4 fs/750 nm laser pulses polarized perpendicular to the gap (see inset on the left), with a gap size of 50 nm. This illustration depicts the instant of time where the maximum of the Gaussian shaped laser pulse peak hits the gap of the tip. Close to the gold electrodes the electric field enhancement is on the order of 3 as visualized by the curves on the right (red) and on the order of 2 (green) across the gap. Figure adopted from [173].

possible due to dispersion effects at the tip.

3.3.2 Optically-induced charge carrier injection in a dielectric as a function of the carrier-envelope phase (CEP)

Our first experiments were aimed to generate currents at the unbiased hybrid junction with intense few-cycle optical fields, gain insight in the nature of the current and evaluate the optically-induced current as a function of the CEP and the peak magnitude of the field. To do so, we first irradiate the junction with one pulse, for both perpendicular and parallel polarizations. The relative CE-phase was controlled by a pair of fused silica wedges as described in section 2.3.3. As mentioned in section 1.8.2 the charge carrier excitation mechanisms are expected to be sensitive to the electric field of the pulse as the processes are highly nonlinear. To extract a net charge per pulse Q_p in the lock-in amplifier originating from the CEP of the pulse, the lock-in amplifier is locked to the modulation frequency of the CEP (see section 2.3). Figure 3.17 illustrates experimental data for the integrated net current Q_p per pulse as a function of the propagation length in fused silica. The electrodes are unbiased as in all experiments. The maximum value of Q_p in the experiments is on the order of 1000 electrons per pulse. The plotted data reveal a modulation of Q_p. The period of modulation in this measurement corresponds to a propagation length inside the fused

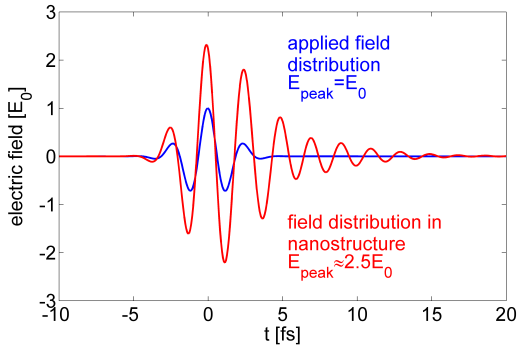

Figure 3.16: This plot depicts the electric field strength of an initial 4 fs laser pulse propagating towards the gap of the SNOM-tip (blue) and the field enhancement in the nanostructure at the position of maximum field enhancement (red) over time. The FDTD simulation reveals an enhancement on the order of 3 with respect to the incoming pulse. Furthermore a strong asymmetric tail is observed, temporally broadening the pulse by more than 5 fs. Figure adopted from [173].

silica wedge of 41 μm. In section 2.3.3 the 2π shift of the CEP was determined to a 41.5 μm for a carrier wavelength of 700 nm. We can conclude that the modulation of Q_p stems from the CEP, a first proof that it is possible to steer a net current of generated charge carriers by the CEP. Simulations performed for the Zener-like tunneling charge injection mechanism are depicted in figure 3.17 (right). The displaced charge per pulse Q_p is plotted as a function of the CEP which confirms the experimental data and reveals a 2π periodicity of the CEP. These results prove that the nanojunction can act as a solid-state absolute phasemeter, where the net charge per pulse Q_p displays the CEP. Additionally, measurements of the net charge as a function of the laser beam position along the electrodes were performed. When the beam does not irradiate the junction (i.e. when the beam is fully positioned on one of the metal electrodes) the CEP-dependent signal vanishes.

Pulse polarization dependence of CEP-controlled current

For a basic understanding of the excitation process in the metal-dielectric-metal nanojunction and the influence of the laser electric field therein, the polarization of the laser pulses was changed from perpendicular to parallel with respect to the gap. In figure 3.18 the data-sets for both laser polarizations for the same tip are depicted. For the polarization parallel to the gap (black), a CEP-dependent current is detected. However, it is one order of magnitude smaller than for the perpendicular case (red) for the same incoming laser intensity. We define the ratio between the maximum net currents of both polarizations as the polarization contrast. In figure 3.18 the polarization contrast is on the order of 20. This

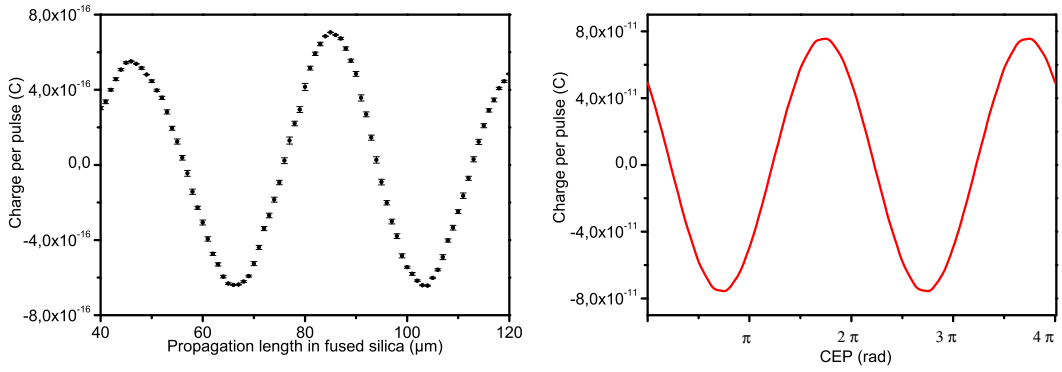

Figure 3.17: Left: Data-set of the measured electric current plotted against the CEP. The suggested net current is detected with a lock-in amplifier and reveals that it is possible to control the directionality of the charge motion in an metal-dielectric-metal nanojunction. Right: Calculation of the expected CEP-dependency normalized in units of charge per pulse, for the Zener-like tunneling model introduced in section 1.8.2.

contrast indicates that an electric field component perpendicular to the gap is required in order to drive excited charge carriers in the direction to the metal electrodes. The residual net current contribution of the parallel polarized pulse in figure 3.18 can be explained by an imperfect alignment of the polarization in respect to the gap. Another possibility for the residual current is the non perfectly straight gap, as the SEM-image in figure 2.8 b) indicates.

3.3.3 Dispersion of the pulse in the nanostructure

As aforementioned, the CEP of the laser pulse is controlled by tuning its propagation length in a dispersive fused silica wedge (see section 1.8). Due to the difference between group and phase velocity in this medium, this propagation adds higher order dispersion, inducing temporal broadening of the pulse. Figure 3.19 shows the optically-generated current in dependence of the propagation length in fused silica for a long range scan. The current modulation is maximum, when the pulse is shortest. The signal decays when the spectral components of the pulse are dispersed by changing the propagation length and its duration consequently increases. This signal decay is a strong indication that the detected current originates from an ultrashort optical field effect, where the detected charge is maximum for the shortest pulse duration.

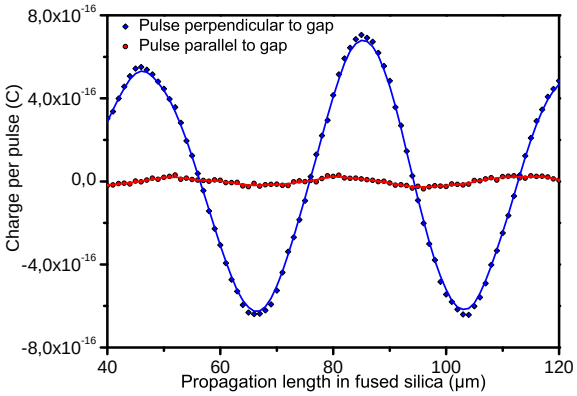

Figure 3.18: CEP-dependent current in a metal-dielectric-metal nanojunction in two configurations: The blue curve was recorded with an incoming laser field of $E_0 \approx 1.5 \cdot 10^{10} \frac{V}{m}$, polarized perpendicular with respect to the gap. In contrast to the red curve, where the laser pulses were oriented parallel to the gap with the same incoming laser field. The ratio of the maximum net currents of both polarizations is defined as the polarization contrast. Here the polarization contrast is on the order of 20.

3.3.4 CEP controlled current as a function of the laser power

As introduced in section 1.8.2, the possible charge carrier excitation mechanisms are strongly nonlinear with respect to the strength of the incident optical field. In order to verify this, subsequent measurements with increasing pulse energy were performed. A plot of the CEP-dependent maximum net charge per pulse Q_p as a function of the electric field strength for pulses polarized perpendicular to the gap is depicted in figure 3.20. Since the intensity of the pulse was adjusted with an iris diaphragm the net current was normalized to the beam waist. The strong nonlinear behavior is a feature of multiphoton excitation, Nordheim-Fowler tunneling and the Zener interband-tunneling. The fitting of the different mechanisms revealed the best agreement for the exponential fit of the Zener interband tunneling, as shown by the dataset in figure 3.20 assuming an energy gap of $E_g = 10$ eV (see dashed red lines).

3.3.5 Decoupling of charge carrier injection and motion control

To get further insight into the origin and dynamics of the charge creating mechanism, the processes of excitation and drive were decoupled. The decoupling is only possible if the charge carriers are generated in the SiO_2. In these injection-drive experiments (the set-up was introduced in section 2.3.4) an injection-pulse which is polarized parallel with respect to the gap was used to excite charge carriers, whereas the drive-pulse, polarized perpendicular to the gap was used to imprint a net momentum to the charge carriers towards the electrodes.

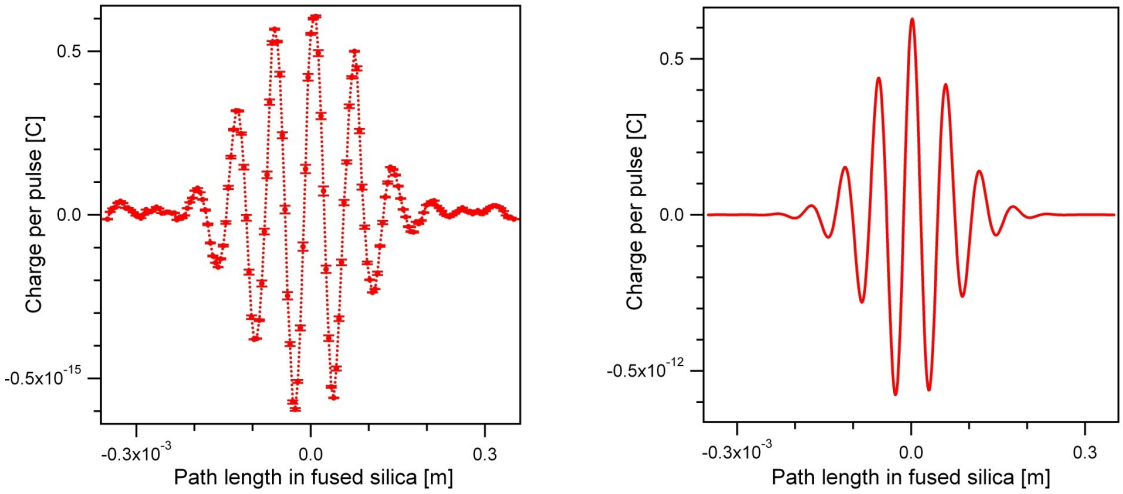

Figure 3.19: Long-range scan of the propagation length of the pulse in the fused silica wedge. The signal is maximum for the shortest pulse duration. Due to a temporal broadening the CEP dependent current decays. Left: Experimental data for long range CEP-dependent measurement, where the maximum net charge corresponds to the shortest pulse duration. The incoming laser field was $E_0 \approx 1.4 \cdot 10^{10}$ V/m. Right: Modeled CEP-dependent net current as a function of the CEP, including temporal broadening due to the chirp of the pulse propagating in the fused silica wedges. For this model the Zener tunneling injection mechanism with $E_0 = 1.4 \cdot 10^{10}$ V/m was assumed.

The laser power of the drive-pulse ($E_0^{drive} \approx 10^9$ V/m) was one order of magnitude lower than the injection-pulse $E_0^{injection} \approx 10^{10}$ V/m, as the drive-pulses was not intended to excite charge carriers but to steer the excited charge carriers to the electrodes. This set-up enabled to measure the integrated net current per pulse Q_p as a function of the delay time $\Delta\tau_{delay}$ between the injection and drive pulse. Additionally, the CEP of the injection pulse $\varphi_{CEP}^{injection}$ and the drive pulse $\varphi_{CEP}^{control}$ were adjustable independently by two pairs of fused silica wedges. Polarization contrast measurements as they are depicted in figure 3.18 are the starting point for this time delay experiments. The results from the contrast measurements are essential as they supply the fused silica wedge positions to adjust the net current of both the pump and drive pulse. In the delay scans presented in the following $\varphi_{CEP}^{injection}$ was kept constant at the fused silica wedge position of maximum net current as shown in figure 3.22 (right), whereas $\varphi_{CEP}^{control}$ was shifted by π between maximum and minimum current.

Figure 3.21 shows a time delay scan, with the $\varphi_{CEP}^{control}$ (polarized perpendicular to the gap) at wedge position of maximum current. The detected net charge Q_p oscillates with the time delay. Additionally, a sub-cycle structure is identifiable, indicating that the current signal originates from an optical field effect. In figure 3.21 the laser power of the injection pulse

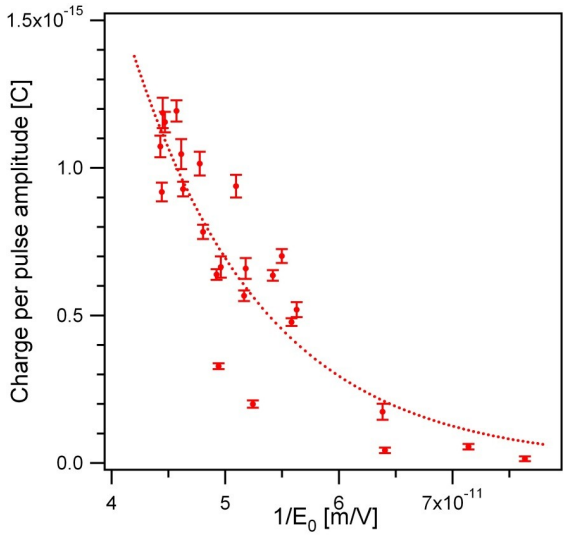

Figure 3.20: CEP-dependent maximum net charge per pulse Q_p as a function of the electric field strength for a variety of pulses polarized perpendicular to the gap. For the exponential fit of the dataset an energy gap of $E_g = 10$ eV was assumed (see red dashed lines).

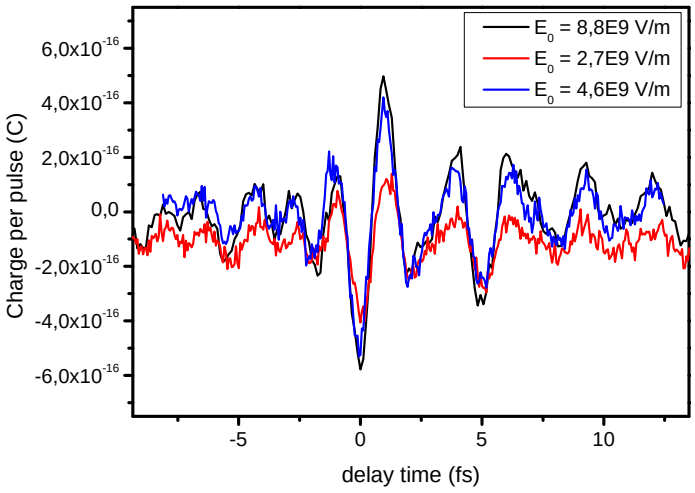

Figure 3.21: Displaced charge per pulse Q_p as a function of time delay visualized for three different control pulse intensities. Here, $\varphi_{CEP}^{injection}$ as well as $\varphi_{CEP}^{control}$ were set to the maximum net current wedge position. The electric field of the injection pulse is $3.6 \cdot 10^{10}$ V/m. The power of the control pulse was varied between $8.8 \cdot 10^9$ V/m (black),$4.6 \cdot 10^9$ V/m (blue) and $2.7 \cdot 10^9$ V/m (red).

was set to a fixed value of 100 mW, which corresponds to an incident electric field strength of $E_0^{injection} = 3.6 \cdot 10^{10}$ V/m, whereas the electric field of the drive pulse was varied was varied between $8.8 \cdot 10^9$ V/m (black),$4.6 \cdot 10^9$ V/m (blue) and $2.7 \cdot 10^9$ V/m (red). The delay scans show, that with decreasing intensity of the control pulse, the detected net current Q_p in the delay scan is reduced, whereas the periodicity of the current oscillation around delay time zero ($\tau_{delay} \approx$ 2.3 fs) is constant for all three curves. These data suggest, that even for low intensities of the control pulse charge carriers are injected by this pulse.

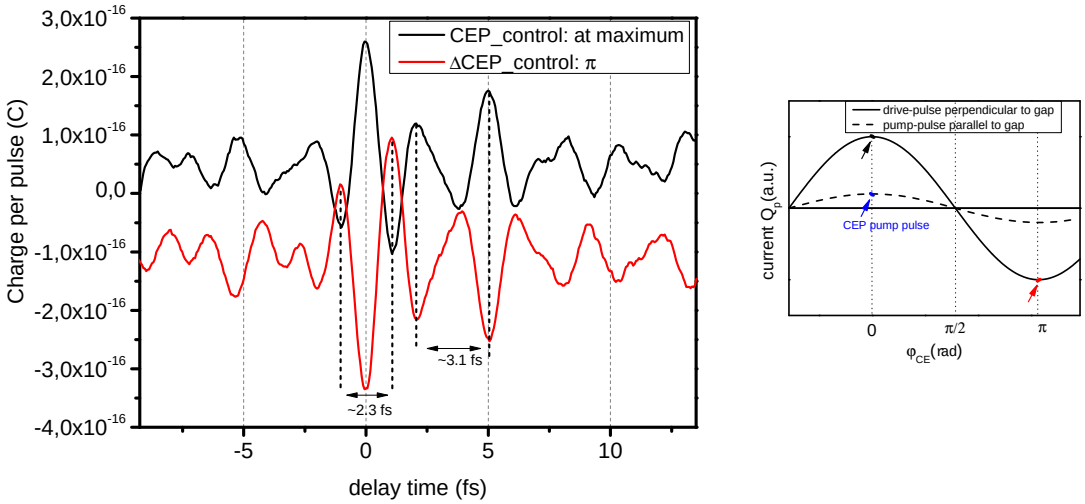

Figure 3.22: Left: Delay scans with the $\varphi_{CEP}^{injection}$ at maximum net charge position while $\varphi_{CEP}^{control}$ was recorded for 2 CEP-values shifted by π ($E_0^{injection} = 3.6 \cdot 10^{10}$ V/m, $E_0^{control} = 0.3 \cdot 10^{10}$ V/m). The smoothed data reveal that the net current switches its polarity around $\Delta\tau_{delay} = 0$. Furthermore a the sub-cycle current oscillation is identifiable. Right: Sketch visualizes the CEP-dependent net charge of both pulse polarizations for the one pulse experiments. The red and black arrows correspond to the CEP positions of the control pulse for which delay scans were performed.

Figure 3.22 depicts two delay scans, which differ only by a shift of π of $\varphi_{CEP}^{control}$, whereas $\varphi_{CEP}^{injection}$ remains the same in the two scans. For a better visualization both datasets are smoothed. The plots clearly exhibit a current inversion. $\Delta\tau_{delay} = 0$ is set to the maximum net current of both curves. This current inversion for a π-shift of the control pulse demonstrates that the electric field of the control pulse steers the excited charge carriers. When comparing the electric field from the FDTD-simulations (see section 3.3.1 figure 3.16) with the delay scans, we can identify the same temporal asymmetry for longer positive time delays. The net current oscillation period close to time zero is determined to $\approx$ 2.3 fs. This is consistent with the laser pulse oscillation period of $\approx$ 2.5 fs. With the

net current oscillation period we can estimate the upper time-window for the injection of charge carriers. To resolve a current oscillation with a period of ≈ 2.5 fs, a current injection process within the half-cycle of the injection pulse periodicity is required. The upper time window for the injection is then limited to ~ 1.2 fs. This can be seen as an ultrashort current switch in the time scale of 1 fs.

3.3.6 Discussion of the charge carrier injection mechanisms in the dielectric

In section 1.8.2 the possible charge carrier injection mechanisms for the metal-dielectric-metal junction were introduced. Here, the different injection mechanisms are set in relation to the experimental data.

In section 3.3.2 first experimental data revealed a CEP dependence of the measured net current Q_p. To determine whether photoemission from the electrodes is a possible mechanism to trigger a current, the laser beam was scanned from the center of the nanojunction towards one of the electrodes. The detected net current Q_p for the laser pulse focused onto one gold electrode should be higher, as the emitted electrons would create holes that should be compensated by a charge flow through the circuit. When the laser spot is moved from the junction to one of the electrodes the net current vanishes, clearly evidencing that the photoemission can be excluded. Moreover the energy of the NIR-pulses is too small to overcome the work-function of gold $W \approx 5$ eV in a single photon excitation process.

The second mechanism to mention is the multiphoton excitation process. The energy gap in SiO_2 is $E_{gap} \approx 9$ eV, thus for an charge injection from the VB to the CB a superposition of at least 6 photons (for a given photon energy of 1.65 eV) are required. Data fits for the intensity dependent net current revealed n ~ 1.3, which is not consistent with the expected I^6 behavior.

Nordheim-Fowler tunneling can only be caused by electric fields perpendicular to the gap. The time delay scans with the excitation pulse parallel and the drive pulse perpendicular to the gap reveal, that the Nordheim-Fowler tunneling is not sensitive to the injection pulse, since the net current is not depending strongly on the intensity of the drive pulse. In order to determine if a non-perfect alignment of the injection pulse with the electrodes could result in the observation of a delay-dependent Nordheim-Fowler current simulations based on the equation 1.23 were performed and are depicted in figure 3.23. The injection pulse was tilted by an angle of 10° with respect to the nanogap, which effects a laser field component perpendicular to the gap. The oscillating delay net current is obtained in the simulations for two delay scans, with a CEP of the drive pulses shifted by π. When comparing this simulations with the experimental data shown in figure 3.22 we perceive that the simulation

do not show the same qualitative form. The simulated net current is point reflected at the point of origin, for CEP shifts of π for the drive pulse. With these simulations we can exclude this excitation mechanism.

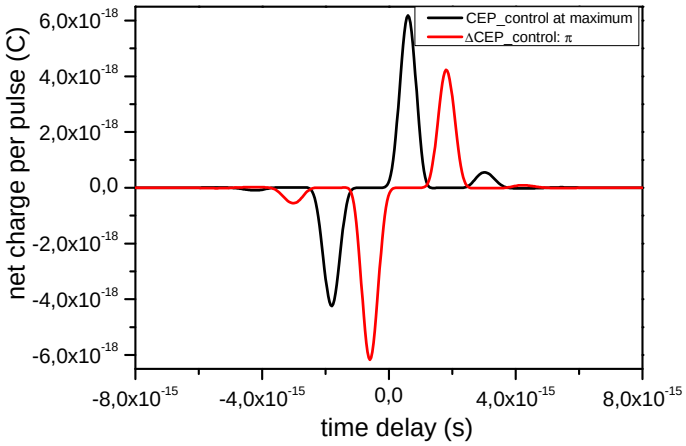

Figure 3.23: Simulations of the net current Q_p of two delay scans where $\Delta\varphi_{CEP}^{control}$ is shifted by π, modeled with the Nordheim-Fowler tunneling. For a better visualization the calculations are offset. The injection pulse is tilted by an angle of 10° with respect to the gap of the junction. The tilt effects a laser field component perpendicular to the gap. At $\Delta\tau_{delay} = 0$ the current is mirrored, which is in contradiction with the measured data, excluding Nordheim-Fowler tunneling as an excitation mechanism in the dielectric.

The semi-classical Zener/Keldysh modeling emerged qualitatively to be the best fitting mechanism. Already the good agreement of data fitting for the power dependence of the one pulse experiments suggested this mechanism. Simulations of the delay scans as a function of the CEP $\varphi_{CEP}^{control}$ and $\varphi_{CEP}^{injection}$ propose exactly the measured periodicity of the displaced net charge Qp modulation. The data simulation of two time delay scans (illustrated in figure 3.24) reveal a qualitatively good agreement of the measured dataset in figure 3.22. A π-shift of $\Delta\varphi_{CEP}^{control}$ shows the same current flip. The simulations are based on ballistic electron transport not including any scattering effects like electron-phonon interactions. To conclude this chapter, the ballistic Zener-tunneling model explains qualitatively the basic features of the experimental data best. We propose from experimental in combination with simulations, that Zener/Keldysh-like interband tunneling is the excitation mechanism of electrons in the dielectric SiO_2.

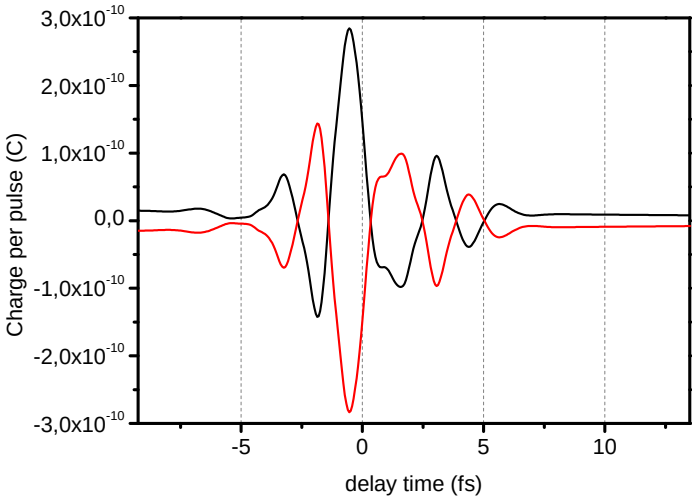

Figure 3.24: Simulation of two delay scan of the net current by the Zener-interband tunneling. The CEP of both calculations is shifted by π. Compared with the experimental data, the simulations of the Zener model are qualitatively in good agreement, explaining the main features of the delay scans measured.

4 Summary and outlook

In conclusion, two basic situations regarding light-induced electron transport in well-defined nanojunctions have been explored. In the first part of this thesis a new experimental set-up combining the exploration of optical and electronic properties of single molecules via electron transport measurements was tested and optimized. The experiments revealed that a tetrahedral SNOM-tip can act as a localized light source and electrode at the same time. Single-photosynthetic proteins, functionalized with cysteine end-groups, were covalently linked between the metalized tip and a metal substrate. Electron-transport measurements under laser illumination reveal a photocurrent of 10 pA [174]. This corresponds to an electron transfer time of 16 ns. It should be noted that this is a first demonstration of a nano-scale optoelectronic circuit on a single biomolecular level. Our observations prove that individual PS I units can act as nanosized current generators in optoelectronic and photovoltaic circuits. Several straightforward technological routes can be chosen to further increase the photovoltaic power output such as utilizing plasmon enhancement effects at optimized wavelength to improve light absorption by individual PS I [30].
The second part of this thesis aimed to explore the optically mechanisms of charge carrier excitation in amorphous silicon dioxide, embedded between two metal electrodes with intense optical fields. It could be shown, that by ultrashort optical NIR-pulses it is possible to hoist charge carriers into the conduction band of the dielectric via highly nonlinear processes. With the same pulse a net momentum is imprinted to the excited electrons, which is manifested in a macroscopically detectable current. The experimental data prove that the electrons can be excited and steered with the electric field of the pulses, depending on the pulse magnitude, polarization, CEP and pulse duration. Experiments with a dual-pulse set-up revealed that a polarization of the pulses perpendicular to the gap is required to imprint a net momentum. Different nonlinear excitation mechanisms were simulated and discussed in the picture of ballistic transport. The semi-classical Zener-interband tunneling explains the characteristics of the time-delay measurements best. The experimental data give strong indications that the electron injection process is limited to a time frame of $\approx$ 1 fs. A quantitative description of the obtained experimental data is under further development in a quantum mechanical picture on the basis of Wannier-Stark states [175]. In summary this metal-dielectric-metal-junction can be viewed as an ultra-fast solid-state optically driven transistor, where the electron motion is steered by optical fields. The results

presented here are the base for the realization of all optically controlled electronic devices, to overcome the speed limitations of silicon-based data processing as well as reduction of heat load.

List of Publications

Publications

- *Ultrafast light field control of electric currents in metal-dielectric interfaces*; T. Paasch-Colberg, A. Schiffrin, **D. Gerster**, S. Mühlbrandt, N. Karpowicz, J. Reichert, J.V. Barth, R. Ernstorfer, R. Kienberger, and F. Krausz, in Nonlinear Optics: Materials, Fundamentals and Applications, OSA Technical Digest (CD) (Optical Society of America, 2011).

- *Light-Field Control of Electric Current in Metal-Dielectric Nano-Circuits*; A. Schiffrin, T. Paasch-Colberg, **D. Gerster**, N. Karpowicz, S. Mühlbrandt, J. Reichert, J. V. Barth, R. Kienberger, R. Ernstorfer, and F. Krausz, in CLEO/Europe and EQEC 2011 Conference Digest, OSA Technical Digest (CD) (Optical Society of America, 2011).

- *Optical-Field-Induced Current in Dielectrics*; A. Schiffrin, T. Paasch-Colberg, N. Karpowicz, V. Apalkov, **D. Gerster**, S. Mühlbrandt, M. Korbman, J. Reichert, Y. Deng, P. Altpeter, J.V. Barth, R. Kienberger, R. Ernstorfer, V. S. Yakovlev, M. I. Stockman, and Ferenc Krausz, submitted.

- *Photocurrent of a single photosynthetic protein*; **D. Gerster**, J. Reichert, H. Bi, J. V. Barth, S. M. Kaniber, Alexander W. Holleitner, I. Visoly-Fisher, S. Sergani, I. Carmeli, submitted.

Conference contributions

- *Optical Spectroscopy on Tuneable Nano Gaps*; **D. Gerster**, J. Reichert , S. Klein, H. Fuchs, J. V. Barth; Deutsche Physikalische Gesellschaft, Frühjahrstagung, Dresden 2009.

- *Single Molecule Transport Junctions Utilizing a SNOM Tip as Counterelectrode*; **D. Gerster**, J. Reichert , S. Klein, H. Fuchs, J. V. Barth; Summerschool on Nanooptics, Aarhus, Denmark 2010.

- *Photocurrent of a single Photosystem I*; **D. Gerster**, S. M. Kaniber, J. V. Barth, A. W. Holleitner, I. Carmeli, Joachim Reichert; Deutsche Physikalische Gesellschaft, Frühjahrstagung, Dresden 2011.
- *Photocurrent of a single photosynthetic protein*; **D. Gerster**, J. Reichert, H. Bi, J. V. Barth, S. M. Kaniber, Alexander W. Holleitner, I. Visoly-Fisher, S. Sergani, I. Carmeli; International Scanning Probe Microscopy Conference, München 2011.

List of Figures

Bibliography

[1] C. Joachim and M.A. Ratner. Molecular electronics: Some views on transport junctions and beyond. *Proc. Natl. Acad. Sci. U. S. A.*, 102(25):8801, 2005.

[2] F. Chen, J. Hihath, Z. Huang, X. Li, and N.J. Tao. Measurement of Single-Molecule Conductance. *Annu. Rev. Phys. Chem.*, 58(1):535–564, 2007.

[3] J. R. Heath. Molecular Electronics. *Annu. Rev. Mater. Res.*, 39(1):1–23, 2009.

[4] J. C. Cuevas and E. Scheer. *Molecular Electronics: An Introduction to Theory and Experiment*, volume 1. World Scientific Pub Co Inc., 2010.

[5] N. J. Tao. Electron transport in molecular junctions. *Nature Nanotech.*, 1(3):173–181, 2006.

[6] W. Lu and C.M. Lieber. Nanoelectronics from the bottom up. *Nat. Mater.*, 6(11):841–850, 2007.

[7] S. J. van der Molen, J. Liao, T. Kudernac, J. S. Agustsson, L. Bernard, M. Calame, B. J. van Wees, B. L. Feringa, and Christian Schönenberger. Light-Controlled Conductance Switching of Ordered Metal-Molecule-Metal Devices. *Nano Lett.*, 9(1):76–80, 2009.

[8] R. M. Metzger. Unimolecular electronics. *J. Mater. Chem.*, 18(37):4364–4396, 2008.

[9] P. F. Barbara, A. J. Gesquiere, S.-J. Park, and Y. J. Lee. Single-Molecule Spectroscopy of Conjugated Polymers. *Acc. Chem. Res.*, 38(7):602–610, 2005.

[10] J. V. Barth, G. Costantini, and K. Kern. Engineering atomic and molecular nanostructures at surfaces. *Nature*, 437(7059):671–679, September 2005.

[11] H. B. Akkerman and B. de Boer. Electrical conduction through single molecules and self-assembled monolayers. *J. Phys.: Condens. Matter*, 20:013001, 2008.

[12] A. Aviram and M. A. Ratner. Molecular rectifiers. *Chem. Phys. Lett.*, 29(2):277 – 283, 1974.

[13] H. Choi and C. C. M. Mody. The Long History of Molecular Electronics. *Social Studies of Science*, 39(1):11–50, 2009.

[14] B. Mann and H. Kuhn. Tunneling through Fatty Acid Salt Monolayers. *J. Appl. Phys.*, 42(11):4398–4405, 1971.

[15] R. M. Metzger, B. Chen, U. Höpfner, MV Lakshmikantham, D. Vuillaume, T. Kawai, X. Wu, H. Tachibana, T.V. Hughes, H. Sakurai, et al. Unimolecular electrical rectification in hexadecylquinolinium tricyanoquinodimethanide. *J. Am. Chem. Soc.*, 119(43):10455–10466, 1997.

[16] J. Reichert, R. Ochs, D. Beckmann, H. B. Weber, M. Mayor, and H. v. Löhneysen. Driving Current through Single Organic Molecules. *Phys. Rev. Lett.*, 88(17):176804, Apr 2002.

[17] A. Salomon, D. Cahen, S. Lindsay, J. Tomfohr, V.B. Engelkes, and C.D. Frisbie. Comparison of Electronic Transport Measurements on Organic Molecules. *Adv. Mater.*, 15(22):1881–1890, 2003.

[18] X. Guo, J. P. Small, J. E. Klare, Y. Wang, M. S. Purewal, I. W. Tam, B. H. Hong, L. Caldwell, R.and Huang, S. O'Brien, J. Yan, R. Breslow, S. J. Wind, J. Hone, P. Kim, and C. Nuckolls. Covalently Bridging Gaps in Single-Walled Carbon Nanotubes with Conducting Molecules. *Science*, 311(5759):356–359, 2006.

[19] D. Dulic, S. J. van der Molen, T. Kudernac, H. T. Jonkman, J. J. D. de Jong, T. N. Bowden, J. van Esch, B. L. Feringa, and B. J. van Wees. One-Way Optoelectronic Switching of Photochromic Molecules on Gold. *Phys. Rev. Lett.*, 91(20):207402, Nov 2003.

[20] S. Yasutomi, T. Morita, Y. Imanishi, and S. Kimura. A Molecular Photodiode System That Can Switch Photocurrent Direction. *Science*, 304(5679):1944–1947, 2004.

[21] S. Battacharyya, A. Kibel, G. Kodis, P. A. Liddell, M. Gervaldo, D. Gust, and S.M. Lindsay. Optical Modulation of Molecular Conductance. *Nano Lett.*, 11(7):2709–2714, 2011.

[22] S. W. Wu, N. Ogawa, and W. Ho. Atomic-Scale Coupling of Photons to Single-Molecule Junctions. *Science*, 312(5778):1362–1365, 2006.

[23] V. Ferri, M. Elbing, G. Pace, M. D. Dickey, M. Zharnikov, P. Samori, M. Mayor, and M. A. Rampi. Light-Powered Electrical Switch Based on Cargo-Lifting Azobenzene Monolayers. *Angew. Chem. Int. Ed.*, 47(18):3407–3409, 2008.

[24] A. Safiei, J. Henzl, and K. Morgenstern. Isomerization of an Azobenzene Derivative on a Thin Insulating Layer by Inelastically Tunneling Electrons. *Phys. Rev. Lett.*, 104(21):216102, May 2010.

[25] P. B. Lukins and T. Oates. Single-molecule high-resolution structure and electron conduction of Photosystem II from scanning tunneling microscopy and spectroscopy. *Biochim. Biophys. Acta, Biophys.*, 1409(1):1 – 11, 1998.

[26] B. D. Reiss, D. K. Hanson, and M. A. Firestone. Evaluation of the Photosynthetic Reaction Center Protein for Potential Use as a Bioelectronic Circuit Element. *Biotechnol. Prog.*, 23(4):985–989, 2007.

[27] I. Carmeli, M. Mangold, L. Frolov, B. Zebli, C. Carmeli, S. Richter, and A. W. Holleitner. A Photosynthetic Reaction Center Covalently Bound to Carbon Nanotubes. *Adv. Mater.*, 19(22):3901–3905, 2007.

[28] S. M. Kaniber, M. Brandstetter, F. C. Simmel, I. Carmeli, and A. W. Holleitner. On-Chip Functionalization of Carbon Nanotubes with Photosystem I. *J. Am. Chem. Soc.*, 132(9):2872–2873, 2010.

[29] S. Mackowski, S. Wormke, A. J. Maier, T. H. P. Brotosudarmo, H. Harutyunyan, A. Hartschuh, A. O. Govorov, H. Scheer, and C. Brauchle. Metal-Enhanced Fluorescence of Chlorophylls in Single Light-Harvesting Complexes. *Nano Lett.*, 8(2):558–564, 2008.

[30] I. Carmeli, I. Lieberman, L. Kraversky, Z. Fan, A. O. Govorov, G. Markovich, and S. Richter. Broad Band Enhancement of Light Absorption in Photosystem I by Metal Nanoparticle Antennas. *Nano Lett.*, 10(6):2069–2074, 2010.

[31] G. Binnig and H. Rohrer. Scanning tunneling microscopy. *Surf. Sci.*, 126(1-3):236–244, 1983.

[32] G. Binnig, C. F. Quate, and Ch. Gerber. Atomic Force Microscope. *Phys. Rev. Lett.*, 56:930–933, Mar 1986.

[33] D.J. Wold and C.D. Frisbie. Formation of metal-molecule-metal tunnel junctions: Microcontacts to alkanethiol monolayers with a conducting AFM tip. *J. Am. Chem. Soc.*, 122(12):2970–2971, 2000.

[34] X.D. Cui, A. Primak, X. Zarate, J. Tomfohr, O.F. Sankey, A.L. Moore, T.A. Moore, D. Gust, G. Harris, and S.M. Lindsay. Reproducible measurement of single-molecule conductivity. *Science*, 294(5542):571, 2001.

[35] J. M. van Ruitenbeek, A. Alvarez, I. Pineyro, C. Grahmann, P. Joyez, M. H. Devoret, D. Esteve, and C. Urbina. Adjustable nanofabricated atomic size contacts. *Rev. Sci. Instrum.*, 67(1):108–111, 1996.

[36] M. A. Reed, C. Zhou, C. J. Muller, T. P. Burgin, and J. M. Tour. Conductance of a Molecular Junction. *Science*, 278(5336):252–254, 1997.

[37] E. Lörtscher, H. B. Weber, and H. Riel. Statistical Approach to Investigating Transport through Single Molecules. *Phys. Rev. Lett.*, 98:176807, Apr 2007.

[38] J. He, F. Chen, P. A. Liddell, J. Andreasson, S.D Straight, D. Gust, T. A Moore, A. L Moore, J. Li, O. F. Sankey, and S. M. Lindsay. Switching of a photochromic molecule on gold electrodes: single-molecule measurements. *Nanotechnology*, 16(6):695, 2005.

[39] X. Li, J. He, J. Hihath, B. Xu, S. M. Lindsay, and N.J. Tao. Conductance of Single Alkanedithiols: Conduction Mechanism and Effect of Molecule-Electrode Contacts. *J. Am. Chem. Soc.*, 128(6):2135–2141, 2006.

[40] H. Park, A.K. L. Lim, A. P. Alivisatos, J. Park, and P. L. McEuen. Fabrication of metallic electrodes with nanometer separation by electromigration. *Appl. Phys. Lett.*, 75(2):301–303, 1999.

[41] A. F. Morpurgo, C. M. Marcus, and D. B. Robinson. Controlled fabrication of metallic electrodes with atomic separation. *Appl. Phys. Lett.*, 74(14):2084–2086, 1999.

[42] Y. V. Kervennic, H. S. J. Van der Zant, A. F. Morpurgo, L. Gurevich, and L. P. Kouwenhoven. Nanometer-spaced electrodes with calibrated separation. *Applied Physics Letters*, 80(2):321–323, 2002.

[43] Z. Li, B. Han, G. Meszaros, I. Pobelov, T. Wandlowski, A. Błaszczyk, and M. Mayor. Two-dimensional assembly and local redox-activity of molecular hybrid structures in an electrochemical environment. *Faraday Discuss.*, 131(0):121–143, 2005.

[44] F. Chen and N. J. Tao. Electron Transport in Single Molecules: From Benzene to Graphene. *Acc. Chem. Res.*, 42(3):429–438, 2009.

[45] S. Strobel, S. Harrer, G. Penso Blanco, G. Scarpa, G. Abstreiter, P. Lugli, and M. Tornow. Planar Nanogap Electrodes by Direct Nanotransfer Printing. *Small*, 5(5):579–582, 2009.

[46] C. Zhou, MR Deshpande, MA Reed, L. Jones Ii, and JM Tour. Nanoscale metal/self-assembled monolayer/metal heterostructures. *Appl. Phys. Lett.*, 71:611, 1997.

[47] J. Liao, L. Bernard, M. Langer, C. Schönenberger, and M. Calame. Reversible Formation of Molecular Junctions in 2D Nanoparticle Arrays. *Adv. Mater.*, 18(18):2444–2447, 2006.

[48] F. Chen, X. Li, J. Hihath, Z. Huang, and N.J. Tao. Effect of Anchoring Groups on Single-Molecule Conductance: Comparative Study of Thiol-, Amine-, and Carboxylic-Acid-Terminated Molecules. *J. Am. Chem. Soc.*, 128(49):15874–15881, 2006.

[49] A. Nitzan and M. A. Ratner. Electron Transport in Molecular Wire Junctions. *Science*, 300(5624):1384–1389, 2003.

[50] Joachim Reichert. *Leitfähigkeitsmessungen an einzelnen organischen Molekülen*. PhD thesis, Universität Karlsruhe, 2003.

[51] Y. Selzer, M. A. Cabassi, T. S. Mayer, and D. L. Allara. Thermally Activated Conduction in Molecular Junctions. *J. Am. Chem. Soc.*, 126(13):4052–4053, 2004.

[52] A. Nitzan. *Chemical dynamics in condensed phases: relaxation, transfer and reactions in condensed molecular systems*. Oxford University Press, USA, 2006.

[53] J. R. Heath and M. A. Ratner. Molecular Electronics. *Phys. Today*, 56(5):43–49, 2003.

[54] I. Ron, I. Pecht, M. Sheves, and D. Cahen. Proteins as Solid-State Electronic Conductors. *Acc. Chem. Res.*, 43(7):945–953, 2010.

[55] A. Nitzan. Electron Transmission Through Molecules and Molecular Interfaces. *Annu. Rev. Phys. Chem.*, 52(1):681–750, 2001.

[56] R.A. Marcus and N. Sutin. Electron transfers in chemistry and biology. *Biochim. Biophys. Acta*, 811(3):265–322, 1985.

[57] T. Mikayama, K. Iida, Y. Suemori, T. Dewa, T. Miyashita, M. Nango, A.T. Gardiner, and R.J. Cogdell. The Electronic Behavior of a Photosynthetic Reaction Center Monitored by Conductive Atomic Force Microscopy. *J. Nanosci. Nanotechnol.*, 9(1):97–107, 2009.

[58] N. Agraït, A. L. Yeyati, and J. M. van Ruitenbeek. Quantum properties of atomic-sized conductors. *Phys. Rep.*, 377(2-3):81 – 279, 2003.

[59] R. Landauer. Spatial variation of currents and fields due to localized scatterers in metallic conduction. *IBM J. Res. Dev.*, 44:251–259, January 1957.

[60] R. Landauer. Electrical resistance of disordered one-dimensional lattices. *Philos. Mag.*, 21(172):863–867, 1970.

[61] E. Scheer, P. Joyez, D. Esteve, C. Urbina, and M. H. Devoret. Conduction Channel Transmissions of Atomic-Size Aluminum Contacts. *Phys. Rev. Lett.*, 78:3535–3538, May 1997.

[62] E. Scheer, N. Agraït, J.C. Cuevas, A.L. Yeyati, B. Ludoph, A. Martín-Rodero, G.R. Bollinger, J.M. van Ruitenbeek, and C. Urbina. The signature of chemical valence in the electrical conduction through a single-atom contact. *Nature*, 394(6689):154–157, 1998.

[63] Bernd Zebli. *Optoelektronische Sensibilisierung von Kohlenstoffnanoröhren durch CdTe-Nanokristalle*. PhD thesis, Universität München, 2009.

[64] E. Ozbay. Plasmonics: Merging Photonics and Electronics at Nanoscale Dimensions. *Science*, 311(5758):189–193, 2006.

[65] W.L. Barnes, A. Dereux, and T.W. Ebbesen. Surface plasmon subwavelength optics. *Nature*, 424(6950):824–830, 2003.

[66] A. V. Zayats, I. I. Smolyaninov, and A. A. Maradudin. Nano-optics of surface plasmon polaritons. *Phys. Rep.*, 408(3-4):131 – 314, 2005.

[67] S. Lal, S. Link, and N.J. Halas. Nano-optics from sensing to waveguiding. *Nat. Photonics*, 1(11):641–648, 2007.

[68] J.A. Schuller, E.S. Barnard, W. Cai, Y.C. Jun, J.S. White, and M.L. Brongersma. Plasmonics for extreme light concentration and manipulation. *Nat. Mater.*, 9(3):193–204, 2010.

[69] H.A. Atwater and A. Polman. Plasmonics for improved photovoltaic devices. *Nat. Mater.*, 9(3):205–213, 2010.

[70] D. W. Pohl, W. Denk, and M. Lanz. Optical stethoscopy: Image recording with resolution $\lambda/20$. *Appl. Phys. Lett.*, 44(7):651–653, 1984.

[71] A. Otto. Excitation of nonradiative surface plasma waves in silver by the method of frustrated total reflection. *Zeitschrift für Physik A Hadrons and Nuclei*, 216:398–410, 1968.

[72] E. Kretschmann and H. Raether. Radiative decay of non radiative surface plasmons excited by light(Surface plasma waves excitation by light and decay into photons applied to nonradiative modes). *Z. Naturforsch., A: Phys. Sci.*, 23:2135, 1968.

[73] E. Kretschmann. Die Bestimmung optischer Konstanten von Metallen durch Anregung von Oberflächenplasmaschwingungen. *Zeitschrift für Physik A*, 241:313–324, 1971.

[74] K. A. Willets and R. P. Van Duyne. Localized Surface Plasmon Resonance Spectroscopy and Sensing. *Annu. Rev. Phys. Chem.*, 58(1):267–297, 2007.

[75] A.V. Zayats and D. Richards. *Nano-Optics and Near-Field Optical Microscopy.* Artech House, 2009.

[76] M. Fleischmann, P.J. Hendra, and A.J. McQuillan. Raman spectra of pyridine adsorbed at a silver electrode. *Chem. Phys. Lett.*, 26(2):163 – 166, 1974.

[77] K. Kneipp, M. Moskovits, and H. Kneipp. *Surface-enhanced Raman Scattering: Physics and Applications*, volume 103. Springer Verlag, 2006.

[78] C.V. Raman and K.S. Krishnan. A new type of secondary radiation. *Nature*, 121(3048):501–502, 1928.

[79] M. Moskovits. Surface roughness and the enhanced intensity of Raman scattering by molecules adsorbed on metals. *J. Chem. Phys.*, 69(9):4159–4161, 1978.

[80] S. Nie and S. R. Emory. Probing Single Molecules and Single Nanoparticles by Surface-Enhanced Raman Scattering. *Science*, 275(5303):1102–1106, 1997.

[81] Katrin Kneipp, Yang Wang, Harald Kneipp, Lev T. Perelman, Irving Itzkan, Ramachandra R. Dasari, and Michael S. Feld. Single Molecule Detection Using Surface-Enhanced Raman Scattering (SERS). *Phys. Rev. Lett.*, 78:1667–1670, Mar 1997.

[82] L. Novotny and B. Hecht. *Principles of Nano-Optics.* Cambridge Univ. Press, 2006.

[83] A. Hartschuh, E. J. Sánchez, X. S. Xie, and L. Novotny. High-Resolution Near-Field Raman Microscopy of Single-Walled Carbon Nanotubes. *Phys. Rev. Lett.*, 90:095503, Mar 2003.

[84] B. Pettinger, B. Ren, G. Picardi, R. Schuster, and G. Ertl. Tip-enhanced Raman spectroscopy (TERS) of malachite green isothiocyanate at Au(111): bleaching behavior under the influence of high electromagnetic fields. *J. Raman Spectrosc.*, 36(6-7):541–550, 2005.

[85] L. Novotny and S.J. Stranick. Near-field optical microscopy and spectroscopy with pointed probes. *Annu. Rev. Phys. Chem.*, 57:303–331, 2006.

[86] A. Lewis, M. Isaacson, A. Harootunian, and A. Muray. Development of a 500 Å spatial resolution light microscope: I. light is efficiently transmitted through $\lambda/16$ diameter apertures. *Ultramicroscopy*, 13(3):227 – 231, 1984.

[87] W. Kühlbrandt. Chlorophylls galore. *Nature*, 411(6840):896–899, 2001.

[88] R.E. Blankenship. Origin and early evolution of photosynthesis. *Photosynth. Res.*, 33(2):91–111, 1992.

[89] J. Xiong and C. E. Bauer. Complex evolution of photosynthesis. *Annu. Rev. Plant Biol.*, 53(1):503–521, 2002.

[90] J. M. Berg, J. L. Tymoczko, and L. Stryer. *Biochemistry.* W.H. Freeman and Company: New York, 2007.

[91] A.N. Melkozernov, J. Barber, and R.E. Blankenship. Light harvesting in photosystem I supercomplexes. *Biochemistry*, 45(2):331–345, 2006.

[92] L. Frolov, Y. Rosenwaks, C. Carmeli, and I. Carmeli. Fabrication of a Photoelectronic Device by Direct Chemical Binding of the Photosynthetic Reaction Center Protein to Metal Surfaces. *Adv. Mater.*, 17:2434–2437, 2005.

[93] I. Carmeli, L. Frolov, C. Carmeli, and S. Richter. Photovoltaic Activity of Photosystem I-Based Self-Assembled Monolayer. *J. Am. Chem. Soc.*, 129(41):12352–12353, 2007.

[94] P. Jordan, P. Fromme, H.T. Witt, O. Klukas, W. Saenger, and N. Krauß. Three-dimensional structure of cyanobacterial photosystem I at 2.5 Å resolution. *Nature*, 411(6840):909–917, 2001.

[95] M. K. Sener, C. Jolley, A. Ben-Shem, P. Fromme, N. Nelson, R. Croce, and K. Schulten. Comparison of the Light-Harvesting Networks of Plant and Cyanobacterial Photosystem I. *Biophys. J.*, 89(3):1630 – 1642, 2005.

[96] A. Amunts, O. Drory, and N. Nelson. The structure of a plant photosystem I supercomplex at 3.4 Å resolution. *Nature*, 447(7140):58–63, 2007.

[97] J.H. Golbeck. *Photosystem I: the light-driven plastocyanin: ferredoxin oxidoreductase.* Springer Verlag, 2006.

[98] J.H. Golbeck. Structure and function of photosystem I. *Annual Review of Plant Physiology and Plant Molecular Biology*, 43(1):293–324, 1992.

[99] K. Brettel. Electron transfer and arrangement of the redox cofactors in photosystem I. *Biochim. Biophys. Acta, Biophys.*, 1318(3):322 – 373, 1997.

[100] Th. Foerster. Zwischenmolekulare Energiewanderung und Fluoreszenz. *Ann. Phys.*, 437(1-2):55–75, 1948.

[101] M. Gouterman. Spectra of porphyrins. *J. Mol. Spectrosc.*, 6:138 – 163, 1961.

[102] Simone Maria Kaniber. *Optoelektronische Phänomene in hybriden Schaltkreisen aus Kohlenstoffnanoröhren und dem Photosystem I.* PhD thesis, Technische Universität München, 2010.

[103] K. Brettel and W. Leibl. Electron transfer in photosystem I. *Biochim. Biophys. Acta, Biophys.*, 1507(1-3):100 – 114, 2001.

[104] C.A. Hutchison, S. Phillips, MH Edgell, S. Gillam, P. Jahnke, and M. Smith. Mutagenesis at a specific position in a DNA sequence. *J. Biol. Chem.*, 253(18):6551, 1978.

[105] M. T. Giardi and E. Pace. Photosynthetic proteins for technological applications. *Trends Biotechnol.*, 23(5):257 – 263, 2005.

[106] B. Esper, A. Badura, and M. Rögner. Photosynthesis as a power supply for (bio-)hydrogen production. *Trends Plant Sci.*, 11(11):543 – 549, 2006.

[107] J. W. Lee, I. Lee, and E. Greenbaum. Platinization: a novel technique to anchor photosystem I reaction centres onto a metal surface at biological temperature and pH. *Biosens. Bioelectron.*, 11(4):375 – 387, 1996.

[108] I. Lee, J. W. Lee, and E. Greenbaum. Biomolecular Electronics: Vectorial Arrays of Photosynthetic Reaction Centers. *Phys. Rev. Lett.*, 79(17):3294–3297, Oct 1997.

[109] P. N. Ciesielski, A. M. Scott, C. J. Faulkner, B. J. Berron, D. E. Cliffel, and G. K. Jennings. Functionalized Nanoporous Gold Leaf Electrode Films for the Immobilization of Photosystem I. *ACS Nano*, 2(12):2465–2472, 2008.

[110] R. Das, P. J. Kiley, M. Segal, J. Norville, A. A. Yu, L. Wang, S. A. Trammell, L. E. Reddick, R. Kumar, F. Stellacci, N. Lebedev, J.l Schnur, B. D. Bruce, S. Zhang, and M. Baldo. Integration of Photosynthetic Protein Molecular Complexes in Solid-State Electronic Devices. *Nano Lett.*, 4(6):1079–1083, 2004.

[111] L. Frolov, Y. Rosenwaks, S. Richter, C. Carmeli, and I. Carmeli. Photoelectric Junctions Between GaAs and Photosynthetic Reaction Center Protein. *J. Phys. Chem. C*, 112(35):13426–13430, 2008.

[112] N. Terasaki, N. Yamamoto, M. Hattori, N. Tanigaki, T. Hiraga, K. Ito, M. Konno, M. Iwai, Y. Inoue, S. Uno, and K. Nakazato. Photosensor Based on an FET Utilizing a Biocomponent of Photosystem I for Use in Imaging Devices. *Langmuir*, 25(19):11969–11974, 2009.

[113] S. M. Kaniber, F. C. Simmel, A. W. Holleitner, and I. Carmeli. The optoelectronic properties of a photosystem I carbon nanotube hybrid system. *Nanotechnology*, 20(34):345701, 2009.

[114] E. Goulielmakis, V. S. Yakovlev, A. L. Cavalieri, M. Uiberacker, V. Pervak, A. Apolonski, R. Kienberger, U. Kleineberg, and F. Krausz. Attosecond Control and Measurement: Lightwave Electronics. *Science*, 317(5839):769–775, 2007.

[115] F. Krausz and M. Ivanov. Attosecond physics. *Reviews of Modern Physics*, 81(1):163–234, 2009.

[116] R. Kienberger, M. Hentschel, M. Uiberacker, C. Spielmann, M. Kitzler, A. Scrinzi, M. Wieland, T. Westerwalbesloh, U. Kleineberg, U. Heinzmann, et al. Steering attosecond electron wave packets with light. *Science*, 297(5584):1144, 2002.

[117] R. Kienberger, E. Goulielmakis, M. Uiberacker, A. Baltuska, V. Yakovlev, F. Bammer, A. Scrinzi, T. Westerwalbesloh, U. Kleineberg, U. Heinzmann, et al. Atomic transient recorder. *Nature*, 427(6977):817–821, 2004.

[118] A. Baltuska, Th. Udem, M. Uiberacker, M. Hentschel, E. Goulielmakis, Ch. Gohle, R. Holzwarth, V. S. Yakovlev, A. Scrinzi, T. W. Hansch, and F. Krausz. Attosecond control of electronic processes by intense light fields. *Nature*, 421(6923):611–615, February 2003.

[119] A.L. Cavalieri, N. Müller, T. Uphues, V.S. Yakovlev, A. Baltuška, B. Horvath, B. Schmidt, L. Blümel, R. Holzwarth, S. Hendel, et al. Attosecond spectroscopy in condensed matter. *Nature*, 449(7165):1029–1032, 2007.

[120] E. Goulielmakis, Z.H. Loh, A. Wirth, R. Santra, N. Rohringer, V.S. Yakovlev, S. Zherebtsov, T. Pfeifer, A.M. Azzeer, M.F. Kling, et al. Real-time observation of valence electron motion. *Nature*, 466(7307):739–743, 2010.

[121] A. Scrinzi, M.Y. Ivanov, R. Kienberger, and D.M. Villeneuve. Attosecond physics. *J. Phys. B: At., Mol. Opt. Phys.*, 39:R1, 2006.

[122] Z. Chang. *Fundamentals of Attosecond Optics*. Taylor and Francis, 2010.

[123] J.C. Diels and W. Rudolph. *Ultrashort laser pulse phenomena*. Elsevier London, 2006.

[124] W. Bragg and R.E. Gibbs. The Structure of α and β Quartz. *Proc. R. Soc. London, Ser. A*, 109(751):405, 1925.

[125] R. P. Gupta. Electronic structure of crystalline and amorphous silicon dioxide. *Phys. Rev. B*, 32:8278–8292, Dec 1985.

[126] J. R. Chelikowsky and M. Schlüter. Electron states in α-quartz: A self-consistent pseudopotential calculation. *Phys. Rev. B*, 15:4020–4029, Apr 1977.

[127] M.V. Fischetti and D.J. DiMaria. Hot electrons in SiO_2: ballistic to steady-state transport. *Solid-State Electron.*, 31(3-4):629–636, 1988.

[128] T. Otobe, K. Yabana, and J.-I. Iwata. First-principles calculation of the electron dynamics in crystalline SiO_2. *J. Phys.: Condens. Matter*, 21(6):064224, 2009.

[129] B. Rethfeld, H. Krutsch, and D.H.H. Hoffmann. Tracing Laser-Induced Dielectric Breakdown in Solids. *Contrib. Plasma Phys.*, 50(1):16–20, 2010.

[130] D. Du, X. Liu, G. Korn, J. Squier, and G. Mourou. Laser-induced breakdown by impact ionization in SiO_2 with pulse widths from 7 ns to 150 fs. *Appl. Phys. Lett.*, 64(23):3071–3073, 1994.

[131] L. N. Gaier, M. Lein, M. I. Stockman, P. L. Knight, P. B. Corkum, M. Yu. Ivanov, and G. L. Yudin. Ultrafast multiphoton forest fires and fractals in clusters and dielectrics. *J. Phys. B: At., Mol. Opt. Phys.*, 37(3):L57, 2004.

[132] M. Lenzner, J. Krüger, S. Sartania, Z. Cheng, Ch. Spielmann, G. Mourou, W. Kautek, and F. Krausz. Femtosecond Optical Breakdown in Dielectrics. *Phys. Rev. Lett.*, 80:4076–4079, May 1998.

[133] H. Friedrich. *Theoretical atomic physics.* Birkhäuser, 2006.

[134] C. Zener. A theory of the electrical breakdown of solid dielectrics. *Proc. R. Soc. London, Ser. A*, 145(855):523–529, 1934.

[135] L. V. Keldysh. Ionization in the field of a strong electromagnetic wave. *Soviet Physics JETP*, 20(5):1307–1314, 1965.

[136] R. H. Fowler and L. Nordheim. Electron Emission in Intense Electric Fields. *Proc. R. Soc. London, Ser. A*, 119(781):pp. 173–181, 1928.

[137] M. Lenzlinger and E. H. Snow. Fowler-Nordheim Tunneling into Thermally Grown SiO_2. *J. Appl. Phys.*, 40(1):278–283, 1969.

[138] J. Ferber, U.C. Fischer, N. Hagedorn, and H. Fuchs. Internal reflection mode scanning near-field optical microscopy with the tetrahedral tip on metallic samples. *Appl. Phys. A*, 69:581–589, 1999. 10.1007/s003390051036.

[139] U.C. Fischer. The tetrahedral tip as a probe for scanning near-field optical microscopy. *NATO ASI Series E Applied Sciences*, 242:255–255, 1993.

[140] E.G. Bortchagovsky, S. Klein, and U. C. Fischer. Surface plasmon mediated tip enhanced Raman scattering. *Appl. Phys. Lett.*, 94(6):063118, 2009.

[141] E. G. Bortchagovsky and U. C. Fischer. A tetrahedral tip as a probe for tip-enhanced Raman scattering and as a near-field Raman probe. *J. Raman Spectrosc.*, 40(10):1386–1391, 2009.

[142] J. Koglin, U. C. Fischer, and H. Fuchs. Material contrast in scanning near-field optical microscopy at 1–10 nm resolution. *Phys. Rev. B*, 55:7977–7984, Mar 1997.

[143] U. C. Fischer, A. Dereux, and J.C. Weeber. Controlling light confinement by excitation of localized surface plasmons. *Near-Field Optics and Surface Plasmon Polaritons*, pages 49–69, 2001.

[144] K. Tanaka, G. Burr, T. Grosjean, T. Maletzky, and U. Fischer. Superfocussing in a metal-coated tetrahedral tip by dimensional reduction of surface-to edge-plasmon modes. *Appl. Phys. B: Lasers Opt.*, 93:257–266, 2008.

[145] A. Taflove and S.C. Hagness. *Computational electrodynamics: The Finite-Difference Time-Domain Method*. Artech House Boston, 1995.

[146] P.l. Geshev, U. C. Fischer, and H.Fuchs. Light scattering by a nanoparticle and a dipole placed near a dielectric surface covered by a thin metallic film. *Opt. Express*, 15(21):13796–13804, Oct 2007.

[147] E. Goormaghtigh, V. Raussens, and J. M. Ruysschaert. Attenuated total reflection infrared spectroscopy of proteins and lipids in biological membranes. *Biochim. Biophys. Acta*, 1422(2):105 – 185, 1999.

[148] L. Layden and D. Wadlow. High velocity carbon dioxide snow for cleaning vacuum system surfaces. *J. Vac. Sci. Technol., A*, 8(5):3881–3883, 1990.

[149] R.Sherman and W. Whitlock. The removal of hydrocarbons and silicone grease stains from silicon wafers. *J. Vac. Sci. Technol., B*, 8(3):563–567, 1990.

[150] R. Sherman, J. Grob, and W. Whitlock. Dry surface cleaning using CO_2 snow. *J. Vac. Sci. Technol., B*, 9(4):1970–1977, 1991.

[151] R. Sherman, D. Hirt, and R. Vane. Surface cleaning with the carbon dioxide snow jet. volume 12, pages 1876–1881. AVS, 1994.

[152] T. R. Matzelle, N. Kruse, and R. Reichelt. Characterization of the cutting edge of glass knives for ultramicrotomy by scanning force microscopy using cantilevers with a defined tip geometry. *J. Microsc.*, 199(3):239–243, 2000.

[153] T. R. Matzelle, H. Gnaegi, A. Ricker, and R. Reichelt. Characterization of the cutting edge of glass and diamond knives for ultramicrotomy by scanning force microscopy using cantilevers with a defined tip geometry. Part II. *J. Microsc.*, 209(2):113–117, 2003.

[154] J. M. Tour, L.R. Jones, D. L. Pearson, J. J. S. Lamba, T. P. Burgin, G. M. Whitesides, D. L. Allara, A. N. Parikh, and S. Atre. Self-Assembled Monolayers and Multilayers of Conjugated Thiols, α, ω.-Dithiols, and Thioacetyl-Containing Adsorbates. Understanding Attachments between Potential Molecular Wires and Gold Surfaces. *J. Am. Chem. Soc.*, 117(37):9529–9534, 1995.

[155] F. Schreiber. Structure and growth of self-assembling monolayers. *Prog. Surf. Sci.*, 65(5-8):151 – 257, 2000.

[156] J. C. Love, L. A. Estroff, J. K. Kriebel, R. G. Nuzzo, and G. M. Whitesides. Self-Assembled Monolayers of Thiolates on Metals as a Form of Nanotechnology. *Chem. Rev.*, 105(4):1103–1170, 2005.

[157] J.G. Simmons. Generalized Formula for the Electric Tunnel Effect between Similar Electrodes Separated by a Thin Insulating Film. *J. Appl. Phys.*, 34(6):1793–1803, 1963.

[158] A. L. Cavalieri, E. Goulielmakis, B. Horvath, W. Helml, M. Schultze, M. Fiess, V. Pervak, L. Veisz, V. S. Yakovlev, M. Uiberacker, A. Apolonski, F. Krausz, and R. Kienberger. Intense 1.5-cycle near infrared laser waveforms and their use for the generation of ultra-broadband soft-x-ray harmonic continua. *New J. Phys.*, 9(7):242, 2007.

[159] Jens Rauschenberger. *Phase-stabilized Ultrashort Laser Systems for Spectroscopy.* PhD thesis, Ludwig Maximilians Universität München, 2007.

[160] Bálint Horváth. *Generation, characterization and sub-cycle shaping of intense, few-cycle light waveforms for attosecond spectroscopy.* PhD thesis, Ludwig Maximilians Universität München, 2009.

[161] E. Moon, H. Wang, S. Gilbertson, H. Mashiko, M. Chini, and Z. Chang. Advances in carrier-envelope phase stabilization of grating-based chirped-pulse amplifiers. *Laser & Photon. Rev.*, 4(1):160–177, 2010.

[162] Markus Fiess. *Advancing attosecond metrology.* PhD thesis, Ludwig Maximilians Universität München, 2010.

[163] T. Fuji, J. Rauschenberger, C. Gohle, A. Apolonski, T. Udem, V. S. Yakovlev, G. Tempea, T. W. Hänsch, and F. Krausz. Attosecond control of optical waveforms. *New J. Phys.*, 7(1):116, 2005.

[164] D. P. Tsai, A. Othonos, M. Moskovits, and D. Uttamchandani. Raman spectroscopy using a fiber optic probe with subwavelength aperture. *Appl. Phys. Lett.*, 64(14):1768–1770, 1994.

[165] J. Ma and Y.-S. Li. Fiber Raman background study and its application in setting up optical fiber Raman probes. *Appl. Opt.*, 35(15):2527–2533, May 1996.

[166] L. F. Santos, R. Wolthuis, S. Koljenović, R. M. Almeida, and G. J. Puppels. Fiber-Optic Probes for in Vivo Raman Spectroscopy in the High-Wavenumber Region. *Anal. Chem.*, 77(20):6747–6752, 2005.

[167] L. Sepunaru, I. Tsimberov, L. Forolov, C. Carmeli, I. Carmeli, and Y. Rosenwaks. Picosecond Electron Transfer from Photosynthetic Reaction Center Protein to GaAs. *Nano Lett.*, 9(7):2751–2755, 2009.

[168] A. Stamouli, J. W. M. Frenken, T. H. Oosterkamp, R. J. Cogdell, and T. J. Aartsma. The electron conduction of photosynthetic protein complexes embedded in a membrane. *FEBS Lett.*, 560(1-3):109 – 114, 2004.

[169] J. Zhao, J. J. Davis, M. S. P. Sansom, and A. Hung. Exploring the Electronic and Mechanical Properties of Protein Using Conducting Atomic Force Microscopy. *J. Am. Chem. Soc.*, 126(17):5601–5609, 2004.

[170] M. Tsutsui, M. Taniguchi, and T. Kawai. Single-molecule identification via electric current noise. *Nat. Commun.*, 1(9):138, 2010.

[171] I. Ron, N. Friedman, M. Sheves, and D. Cahen. Enhanced Electronic Conductance across Bacteriorhodopsin, Induced by Coupling to Pt Nanoparticles. *J. Phys. Chem. Lett.*, 1(20):3072–3077, 2010.

[172] M. D. Perez, C. Borek, S. R. Forrest, and M. E. Thompson. Molecular and Morphological Influences on the Open Circuit Voltages of Organic Photovoltaic Devices. *J. Am. Chem. Soc.*, 131(26):9281–9286, 2009.

[173] Sascha Mühlbrandt. Ultrafast Light-Field Control of Electric Current at Metal-Dielectric Nanojunctions. Master's thesis, Technische Universtität München, November 2011.

[174] D. Gerster, J. Reichert, H. Bi, J. V. Barth, S. M. Kaniber, Alexander W. Holleitner, I. Visoly-Fisher, S. Sergani, and I. Carmeli. Photocurrent of a single photosynthetic protein. *submitted*, 2011.

[175] A. Schiffrin, T. Paasch-Colberg, N. Karpowicz, V. Apalkov, D. Gerster, S. Mühlbrandt, M. Korbman, J. Reichert, Y. Deng, P. Altpeter, J.V. Barth, R. Kienberger, R. Ernstorfer, V. S. Yakovlevand M. I. Stockman, and Ferenc Krausz. Optical-Field-Induced Current in Dielectrics. *submitted to Nature*, 2011.

Acknowledgement

Without the support of a many people this thesis would not have been possible:

First of all I would like to thank Prof. Dr. Johannes V. Barth, giving me the possibility to work for and in your group. It was great pleasure!!!

Dr. Joachim Reichert, i am very grateful for your excellent expertise,your patience, your support at any time!!!!

Dr. Agustin Schiffrin, it was a great pleasure to work with you. Thanks, for introducing me to the world of ultrashort physics.

Thanks to Prof. Dr. Aleaxander W. Holleitner for being part of this interesting project and for agreeing to act as second examiner.

Prof. Dr. Ferenc Krausz and Prof. Dr. Reinhard Kienberger at the Max Planck Insitute for Quantum optics for giving me the possibility to work on this project.

Miss Frischke at LMU who did a lot of gold coating on my SNOM-tips as well as Sebastian Schöll at Walter Schottky Institut.

Sascha Mühlbrandt it was always a pleasure to work with you before, during and after beamtimes.

Simone M. Kaniber thank you for the preparation of molecule substrates.

Hai Bi thanks for all your support, it was great to work with you.

Karl Kölbl, Karl Eberle, Reinhold Schneider, Hartmut Schlichting and Peter Feulner for you technical support, without your help the experiments would have never worked.

My colleagues from the legendary office: Dirk, Matze, Wolfgang, Wastl, Knud, Claudia, Richard thank you all for your psychological support, it was a great pleasure sharing my time with you. Not to forget Andreas, Felix and Stefan also supporting me.

Florian Blobner did an extraordinary job, reading and correcting my thesis at least twice. Thanks.

Kamilla and Viktoria as the helping hands besides research.

Maria I specially want to thank you, for everything you did for me during this thesis. You always motivated and believed in me!!!!!

My and Maria's family Gerster and Quast- thanks for all for supporting me!!